AFRL-VS-HA-TR-2005-1207

Investigation of Plasma Phenomena in the Ionosphere Under Natural Conditions and Under Conditions Artificially Perturbed by *HAARP*

James A. Secan
Edward J. Fremouw
Andrew J. Mazzella, Jr.
John Rasmussen
A. Lee Snyder

NorthWest Research Associates, Inc.
14508 NE 20th Street
Bellevue, WA 98007-3713

Scientific Report No. 1

17 August 2005

APPROVED FOR PUBLIC RELEASE; DISTRIBUTION UNLIMITED.



AIR FORCE RESEARCH LABORATORY
Space Vehicles Directorate
29 Randolph Rd.
AIR FORCE MATERIEL COMMAND
Hanscom AFB, MA 01731-3010

This technical report has been reviewed and is approved for publication.

AFRL-VS-HA-TR-2005-1207

/signed/

JAMES BATTIS
Contract Manager

/signed/

JOEL B. MOZER, Chief
Space Weather Center of Excellence

This report has been reviewed by the ESC Public Affairs Office (PA) and is releasable to the National Technical Information Service (NTIS).

Qualified requestors may obtain additional copies from the Defense Technical Information Center (DTIC). All others should apply to the National Technical Information Service.

If your address has changed, if you wish to be removed from the mailing list, or if the addressee is no longer employed by your organization, please notify AFRL/VSIM, 29 Randolph Rd., Hanscom AFB, MA 01731-3010. This will assist us in maintaining a current mailing list.

Do not return copies of this report unless contractual obligations or notices on a specific document require that it be returned.

Using Government drawings, specifications, or other data included in this document for any purpose other than Government procurement does not in any way obligate the U.S Government. The fact that the Government formulated or supplied the drawings, specifications, or other data does not license the holder or any other person or corporation; or convey any rights or permission to manufacture, use, or sell any patented invention that may relate to them.

REPORT DOCUMENTATION PAGE [example]

Form Approved OMB No. 0704-0188

Public reporting burden for this collection of information is estimated to average 1 hour per response, including the time for reviewing instructions, searching existing data sources, gathering and maintaining the data needed, and completing and reviewing this collection of information. Send comments regarding this burden estimate or any other aspect of this collection of information, including suggestions for reducing this burden to Department of Defense, Washington Headquarters Services, Directorate for Information Operations and Reports (0704-0188), 1215 Jefferson Davis Highway, Suite 1204, Arlington, VA 22202-4302. Respondents should be aware that notwithstanding any other provision of law, no person shall be subject to any penalty for failing to comply with a collection of information if it does not display a currently valid OMB control number. PLEASE DO NOT RETURN YOUR FORM TO THE ABOVE ADDRESS.

1. REPORT DATE *(DD-MM-YYYY)*	2. REPORT TYPE	3. DATES COVERED *(From - To)*
17-08-2005	Scientific Report 1	17-02-2004 to 17-08-2005

4. TITLE AND SUBTITLE

Investigation of Plasma Phenomena in the Ionosphere Under Natural Conditions and Under Conditions Artificially Perturbed by *HAARP*

5a. CONTRACT NUMBER
FA8718-04-C-0001

5b. GRANT NUMBER
N/A

5c. PROGRAM ELEMENT NUMBER
N/A

6. AUTHOR(S)

J.A. Secan, E.J. Fremouw, A.J. Mazzella, Jr., J. Rasmussen, A.L. Snyder

5d. PROJECT NUMBER
4827

5e. TASK NUMBER
HA

5f. WORK UNIT NUMBER
R1

7. PERFORMING ORGANIZATION NAME(S) AND ADDRESS(ES)

NorthWest Research Associates, Inc.
14508 NE 20th Street
Bellevue, WA 98007-3713

8. PERFORMING ORGANIZATION REPORT NUMBER
NWRA-BELL-05-R307

9. SPONSORING / MONITORING AGENCY NAME(S) AND ADDRESS(ES)

Air Force Research Laboratory
29 Randolph Rd.
Hanscom AFB, MA 01731-3010

10. SPONSOR/MONITOR'S ACRONYM(S)
AFRL/VSBXI

11. SPONSOR/MONITOR'S REPORT NUMBER(S)
AFRL-VS-HA-TR-2005-1207

12. DISTRIBUTION / AVAILABILITY STATEMENT

Approved for public release; distribution unlimited.

13. SUPPLEMENTARY NOTES

14. ABSTRACT

During the 18-month period covered by this report, NorthWest Research Associates (NWRA) conducted ionospheric measurements at several Air Force research and operational locations and analyzed the data collected thereby. The measurements were performed using a variety of radiowave techniques, most involving transionospheric radio propagation, and included observations of ionospheric perturbations via high-power transmissions under the High frequency Active Auroral Research Program (HAARP). Notable among the instruments employed were the NWRA ITS10S coherent radio receiving system and the NWRA GIOS GPS receiver system. The primary measurements were of ionospheric total electron content (TEC) and radiowave scintillation, for describing the ionosphere and its plasma-density structures in the natural ionosphere and under the perturbing influence of HAARP. Records of TEC were inverted tomographically to produce two-dimensional (altitude versus latitude) images of plasma density. By these and other means, ionospheric features such as the main F-layer trough and polar patches were characterized for application to Air Force environmental models. A model for the confidence level of scintillation estimates provided by the WBMOD ionospheric scintillation model was developed.

15. SUBJECT TERMS

Ionosphere, Ionospheric tomography, Total Electron Content (TEC), Ionospheric scintillation, Incoherent Scatter Radar (ISR), Riometer, Auroral ionosphere

16. SECURITY CLASSIFICATION OF: None			17. LIMITATION OF ABSTRACT	18. NUMBER OF PAGES	19a. NAME OF RESPONSIBLE PERSON
a. REPORT	b. ABSTRACT	c. THIS PAGE			Mr. James Battis
U	U	U	SAR	84	19b. TELEPHONE NUMBER *(include area code)* 781-377-4669

Contents

1. Project Objectives 1

2. HAARP Topics 1
   2.1 Summary of HAARP Data Collection Activities 1
      2.1.1 LEO Satellite and Tomography Data Sets 2
      2.1.2 GPS Data Sets 8
   2.2 Tomographic Image Uncertainty Specification 9
      2.2.1 Background 9
      2.2.2 The Formalism and Its Scaling 9
      2.2.3 Empirical Calibration of the Formal Estimates 10
      2.2.4 Uncertainty in Vertical TEC 19
   2.3 Comparison of Tomography and Digisonde Observations 19
   2.4 Observations of the Artificially-Perturbed Ionosphere 28

3. Non-HAARP Topics 33
   3.1 Ionospheric Scintillation Confidence Model 33

4. Publications and Presentations 44

APPENDICES
   Appendix A. Data Displays from the HAARP Web Site 45
   Appendix B. Consultant Support to HAARP Activities 55
      B.1 Report from Mr. John Rasmussen 55
      B.2 Report from Dr. Arnold Snyder 57
      B.3 Report from Dr. Allan Schell 60
      B.4 Report from Mr. Jens Ostergaard 64
      B.5 Report from Dr. Spencer Kuo 66
      B.6 Report from Dr. William Gordon 66
   Appendix C. Student Intern Activities 67
      C.1 Report for Period June through August 2004 67
      C.2 Report for Period June through August 2005 68

References 69

List of Symbols, Abbreviations, and Acronyms 71

Figures

Figure 1. Location of LEO receiver sites in Alaska. Sites indicated by stars (C: Cordova, G: Gakona, D: Delta, A: Artic Village) have NWRA ITS10S receivers. Sites indicated by circles (Y: Ft. Yukon, K: Kaktovic) have UTA CIDR receivers.....2

Figure 2. Summary flow diagram for the tomography processing system.....4

Figure 3. Flow diagram of the data preprocessing section of the tomographic processing system (the block labeled "Data Preparation" in Figure 2).....5

Figure 4. Flow diagram of the tomographic analysis section of the tomographic processing system (the block labeled "Tomographic Inversion Processor" in Figure 2).....6

Figure 5. Relative slant TEC from the observations that went into the image shown in Figure A2 in Appendix A. The solid box indicates the image range used until recently, and the dashed lines indicate the extended range of images to be used in processing henceforth.....7

Figure 6. Comparison of error and difference profiles for (a) daytime and (b) nighttime cases. Solid curves are vertical profiles of formal errors; dotted curves are RMS difference profiles between the tomographic image and the corresponding Chatanika ISR record; dashed curves are the ratio of these two; and the dot-dash curves are 10 times the formal error for (a) and 3 times for (b).....12

Figure 7. Comparison of f_0F2 values (dark diamonds) obtained from 63 tomographic images and their estimated ±RMS uncertainties (lighter blue symbols) with f_0F2 values (x-axis) obtained from nearly simultaneous ionograms.....15

Figure 8. Comparison of f_0F2 values (solid line) derived from tomographic reconstruction of (a) nighttime and (b) daytime Chatanika ISR records and their estimated ±RMS uncertainties (dashed lines) with f_0F2 values (diamonds) scaled from the ISR record.....16

Figure 9a. Example (Chatanika daytime case) of presentation intended for posting on the HAARP Web site, showing tomographic image on top and f_0F2 with its uncertainty band, along with VTEC on the bottom.....17

Figure 9b. Example (Chatanika daytime case) of alternate presentation intended for posting on the HAARP Web site, showing tomographic image on top and uncertainty field on bottom.....18

Figure 10. Vertical (or equivalent-vertical) TEC for GPS (o) and Digisonde (+) measurements for 12 September 2004, displaying the predominant TEC discrepancy between the GPS and Digisonde values during the daytime periods (0-4 UT and 15-24 UT).....20

Figure 11. Vertical (or equivalent-vertical) TEC for GPS (o) and Digisonde (+) measurements for 11 June 2004 (day 163). Note that the period from 7-11 UT is local night for Gakona, Alaska, for this date. The TEC discrepancy displayed in Figure 10 is essentially absent for this day.....21

Figure 12. Density profile from tomography (o) for 19:19 UT on 11 June 2004 (day 163), with derived Digisonde density profiles (+) at 19:15 UT.....21

Figure 13. Vertical (or equivalent-vertical) TEC for tomography (Δ), GPS (o), and Digisonde (+) measurements for 28 October 2004 (day 302) and 29 October 2004 (day 303). 22

Figure 14. Density profiles for tomography (o) and Digisonde (+) for four time periods (04:43 UT, 16:08 UT, 21:50 UT, 22:45 UT) on 29 October 2004 (day 303) 23

Figure 15. Density profiles for tomography (o) and Digisonde (+) for 22:04 UT and 23:00 UT on 28 January 2005 (day 28), 22:57 UT on 04 February 2005 (day 35), 21:42 UT and 22:16 UT on 13 February 2005 (day 44), and 19:15 UT on 13 March 2005 (day 72), with disparate topside density profiles arising from the extrapolated DISS scale height determination being significantly smaller than the topside scale height for the tomography representation. For the case on day 35, the DISS TEC is 4.1 TEC units, while the tomography TEC is 7.0 TEC units; for day 28 (23:00 UT), day 35, day 44, and day 72, the peak densities are also significantly discrepant 24

Figure 16. Density profile for tomography (o) and Digisonde (+) for 22:22 UT on 04 February 2005 (day 35), which display a closer TEC agreement (better than the typical factor of two discrepancy), even if the topside profiles diverge. The DISS TEC is 6.3 TEC units, while the tomography TEC is 8.0 TEC units, with the topside discrepancy partially compensated by the discrepancy in peak densities. 25

Figure 17. Density profiles for tomography (o) and Digisonde (+) for 20:29 UT and 20:59 UT on 27 February 2005 (day 58), exhibiting discrepancies in the bottomside profile and peak densities, respectively, despite the good TEC agreement between DISS and tomography, which are both different from GPS TEC. 26

Figure 18. Vertical (or equivalent-vertical) TEC for tomography (Δ), GPS (o), and Digisonde (+) measurements for 27 February 2005 (day 58), indicating good TEC agreement between DISS and tomography TEC values at 20:29 UT and 20:59 UT, despite the discrepant density profiles. Note that a TEC discrepancy with GPS TEC remains 27

Figure 19. Density profile for tomography (o) and Digisonde (+) for 19:41 UT on 13 March 2005 (day 72), which displays a closer TEC agreement (better than the typical factor of two discrepancy), even if the topside profiles diverge. The DISS TEC is 10.1 TEC units, while the tomography TEC is 12.0 TEC units. 27

Figure 20. Data from the Kodiak SuperDARN radar (courtesy of R. Bristow of the University of Alaska at Fairbanks). The top panel shows the return power as a function of latitude and longitude at a time near the pass of interest, and the lower panel shows the return power as a function of latitude and Universal Time (UT). The vertical dotted line in the lower panel indicates the time of the pass of interest. 30

Figure 21. Electron density as a function of geomagnetic latitude and altitude derived from TEC data collected from the Oscar 31 pass using the NWRA tomographic processor (upper panel), and vertical TEC and f_0F2 as a function of geomagnetic latitude derived from the image in the upper panel (lower panel) 31

Figure 22. Detrended (30 second period) VHF intensity (upper plot) and differential phase (lower plot) from the Gakona ITS10S station for the 0337UT Oscar 31 pass on 11 February 2005. The horizontal dashed lines indicate the segment that is within 16 of the

heater beam center and the horizontal solid line indicates the segment within 8 of beam-center. Closest approach to beam-center is indicated by the vertical dashed line. 32

Figure 23. Detrended (30 second period) VHF intensity (upper plot) and differential phase (lower plot) from the Delta ITS10S station for the 0337UT Oscar 31 pass on 11 February 2005. The format of this figure is the same as Figure 22. 32

Figure 24. VHF intensity spectra from the ITS10S receivers at Gakona (first and second panels) and at Delta (third panel) from the Oscar 31 pass at 0337UT on 11 February 2005. In each panel, the upper plot is the time-series of detrended (30 second detrend period) VHF intensity and the lower plot is the power-density spectrum of the time series. The dotted line in the spectrum plots indicates the noise floor of the measurements. 33

Figure 25. Example of the height variation of the height confidence-level factor. 38

Figure 26. Example of the seasonal variation at Ancon, Peru. 40

Figure 27. Example of the elevation-angle confidence-level factor. 40

Figure 28. Variation of the confidence level as a function of geographic latitude along the 100° longitude meridian for local noon. 41

Figure 29. Variation of the confidence level as a function of geographic latitude along the 100° longitude meridian for local midnight. 41

Figure 30. Variation of the confidence level as a function of geomagnetic latitude at various geomagnetic latitudes for 1700 GMT. See text for details. 43

Figure A1. Example of LEO satellite data collected from the ITS10S receiver located at the new Arctic Village site. The upper panel shows the relative slant TEC, phase scintillation, and intensity scintillation for the pass, the lower-left panel shows the elevation and azimuth angle geometry of the pass, and the lower-right panel shows the pass geometry on a map of Alaska. 47

Figure A2. Sample image generated from the NWRA tomographic processor. The upper panel is a contour plot of electron density, and the lower plot show vertical TEC (solid curve) and f_oF2 (dashed curve) derived from the image. The locations of receiver locations that contributed data to the image are shown as triangles along the bottom of both plots. 48

Figure A3. Example of GPS satellite data collected from the Ashtech Z-FX receiver located at Gakona. The upper panel shows the absolute slant TEC for the pass, the lower-left panel shows the elevation and azimuth angle geometry of the pass, and the lower-right panel shows the pass geometry on a map of Alaska. 49

Figure A4. Daily individual GPS summary plot as shown on the HAARP Web site. The vertical absolute TEC (red lines) and elevation angle (black lines) are plotted as a function of UT for each GPS satellite as identified by PRN. 50

Figure A5. Summary of GPS-derived VTEC (colored curves) and LEO-derived VTEC (black curves) for a 36-hour period. The upper panel shows the variation of VTEC and the lower panel shows the 350 km IPP for the observation. The dashed curves in the upper panel are VTEC derived from the GPS TEC model (*Klobuchar*, 1987) using the

IONO coefficients in the GPS telemetry stream for that day. The upper curve is for a GPS path looking to the south from Gakona and the lower curve is for a path looking to the north. 51

Figure A6. Same data (GPS only) as shown in Figure A5 but for a seven-day period. 52

Figure A7. Same data (GPS only) as shown in Figure A5 but for a twenty-eight-day period. 53

Figure A8. GPS position-error plot for a 36-hour period. The upper panel shows the altitude provided by the GPS clock for the 36-hour period, and the lower panel shows the GPS horizontal position relative to the true horizontal position. The inset blue ellipse in the lower panel is a least-squares fit to the horizontal error data showing the rms error by the size of the semi-major and semi-minor axes....54

Figure B1. New Dome Shelter for the Narrow-Field-of-View Telescope on Pad 3 (left), and the new shelter layout on Pad 3. 56

Figure B2. HAARP installation of the 16-panel AMISR prototype antenna. 58

Tables

Table 1. Station-availability summary for tomographic images in 2004....7

Table 2. Station-availability summary for tomographic images in 2005 (through August). 8

Table 3. List of satellite passes from which data were collected during the optics campaign. 28

Table 4. Factors to be included in a WBMOD confidence-level model....33

Preface and Acknowledgements

This report summarizes work completed during the period 17 February 2004 through 17 August 2005 on a project to investigate ionospheric plasma phenomenology in both the naturally-occurring and artificially-stimulated ionosphere. Most of the observations were made at, or in conjunction with, the High-frequency Active Auroral Research Program (HAARP) facility located near Gakona, AK. This work was completed by employees and consultants of NorthWest Research Associates, Inc. (NWRA).

In addition to the authors listed on this report, other contributors of material for this report and contributors to the activities described in this report include NWRA employees John Begenisich, Eric Collins, Susan Rao, and student intern Troy Lawlor, as well as NWRA consultants Spencer Kuo, William Gordon, Allan Schell, Jens Ostergaard, and J. Francis Smith.

1. Project Objectives

Under this contract, Northwest Research Associates (NWRA) is performing measurements of the ionosphere in order to investigate plasma phenomena in both the natural ionosphere and in the ionosphere perturbed by the High-frequency Active Auroral Research Program (HAARP) high-frequency heater. The research being conducted falls within Hanscom Technical Areas 3(a), "Ionospheric Effects Research and Department of Defense Systems," and 3(b), "Ionospheric Research Technology," of the Broad Agency Announcement VS-03-01 released by the Air Force Research Laboratory (AFRL).

As a contribution to Technical Area 3(b), we are collaborating with scientists and engineers from AFRL, the Naval Research Laboratory (NRL), and other research organizations in the application of diagnostic instrumentation to HAARP. Among the HAARP instruments that we are applying to ionospheric research are three NWRA ITS10S coherent radio receiving systems for measuring relative Total Electron Content (TEC) and recording scintillation, and an Ashtech Model Z-FX GPS receiver for measuring absolute TEC. We are posting TEC from these instruments, and phase-scintillation records from the ITS10S receivers, on the HAARP Web site (www.haarp.alaska.edu) for telescience applications and for decision-making during active experiments, and we are also focusing on inverting the TEC data tomographically to produce images of the F layer over Alaska. Research topics under the foregoing objectives are reported in Section 2.

In Technical Area 3(a), NWRA is (1) developing techniques for partitioning ionospheric Total Electron Content (TEC) into ionospheric and plasmaspheric content and employing them to study the behavior of the plasmapause and plasmaspheric TEC using GPS measurements of TEC, (2) developing a next-generation GPS ionospheric measuring system, (3) investigating methods for estimating phase scintillation spectra produced by Ashtech Z-12 receivers, and (4) analyzing long-term scintillation databases to determine climatological behavior of ionospheric scintillation. Research topics under the foregoing objectives are reported in Section 3.

2. HAARP Topics

Under this contract, NWRA coordinated installation of enhanced diagnostic instrumentation and participated in research employing some of them. Our activities aimed at enhancing HAARP diagnostics were carried out primarily by NWRA consultants John Rasmussen, A. Lee Snyder, Jens Ostergaard, and Spencer Kuo. Their efforts are detailed in Appendix B. NWRA also employed a summer student intern, Mr. Troy Lawlor, who worked with AFRL personnel at Hanscom AFB and at the HAARP site. A summary of Mr. Wellman's activities is presented in Appendix C.

2.1 Summary of HAARP Data Collection Activities

NWRA's HAARP research activities centered on collection and analysis of transionospheric radiowave data. Transmission of two or more phase-coherent radio signals from satellites above the ionosphere to receivers on the ground permits measurement of the path integral of plasma density (so-called total electron content, or TEC) through the ionosphere. TEC is proportional to the dispersive (differential) phase between the two signals (and, with less precision but greater certainty, to differential group delay). Recording of rapid fluctuations in dispersive phase and in received signal strength yields measurement of trans-ionosphere radiowave scintillation.

Under this contract, NWRA measured TEC on slowly moving paths penetrating the entire ionosphere by recording dispersive phase and differential group delay registered on signals transmitted from satellites of the Global Positioning System (GPS) to Gakona, AK. We also measured both TEC and scintillation on paths between satellites moving rapidly over Alaska in high-inclination, low-earth orbits (LEO) just above the main ionospheric (F) layer and several ground stations. Collection and analysis of the LEO data sets is presented in Section 2.1.1, and collection and analysis of the GPS data sets is presented in Section 2.1.2. All of the data and displays described in these two sections are archived on either the HAARP computer network at the HAARP facility near Gakona, AK, or on servers at NWRA's Bellevue office.

2.1.1 LEO Satellite and Tomography Data Sets

NWRA operates NWRA ITS10S receiver systems at four sites in Alaska in support of HAARP operations: Cordova, Gakona (at the HAARP facility), Delta Junction, and Arctic Village. In addition, we obtain data from two University of Texas at Austin (UTA) CIDR receivers operated by the University of Alaska Geophysical Institute (UAF GI) at two sites in Alaska: Ft. Yukon and Kaktovik. Figure 1 shows the locations of these sites on a map of Alaska. The site at Arctic Village was established during the current contract, and is an important additional site in the tomography chain. An example of data from this new site can be seen in Appendix A (Figure A1). Data from LEO satellite passes collected at NWRA's four sites are all displayed in this format on the HAARP Web site (www.haarp.alaska.edu), accessible through that site's Data Index page.

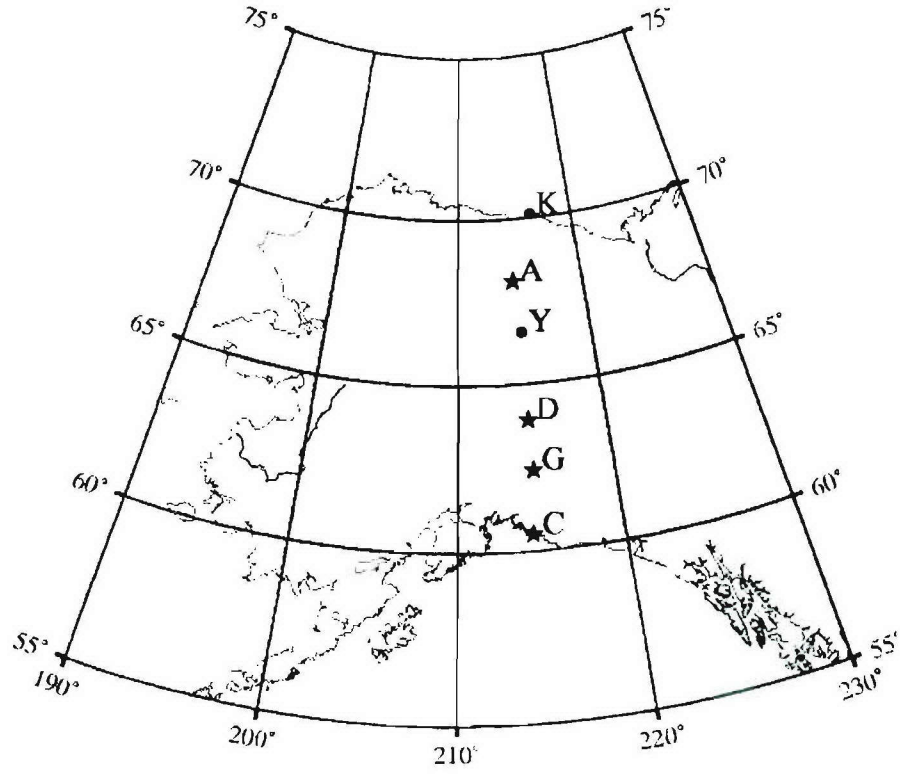


Figure 1. Location of LEO receiver sites in Alaska. Sites indicated by stars (C: Cordova, G: Gakona, D: Delta, A: Artic Village) have NWRA ITS10S receivers. Sites indicated by circles (Y: Ft. Yukon, K: Kaktovic) have UTA CIDR receivers.

Data from these sites are transferred to both HAARP facility computers and to NWRA's Bellevue office for generation of displays, as shown in Figure A1, and tomographic analyses. Descriptions of the tomographic processor used to generate images and the criteria used to select passes for tomographic analysis can be found in *Andreasen et al.* (2004) and *Fremouw et al.* (1992, 1994). The implementation of the processing algorithms and the associated data preprocessing is show in Figures 2 (overall processing flow), 3 (data preprocessing), and 4 (tomographic analysis). The names shown in parenthesis in the boxes (for example, g_mtrx) are the names of programs in which the particular function is implemented.

Images for selected passes are generated in near real-time and posted on the HAARP Web site and stored in NWRA's tomography image database in Bellevue. Figure A2 in Appendix A shows an example of a tomographic image generated using data collected from an Oscar 32 pass over the tomography chain from 0926 to 0944 UT on 09 February 2005. The upper panel shows the electron density as a function of geomagnetic latitude and altitude derived from the analysis, and the lower panel shows vertical TEC and f_0F2 estimates calculated from the image shown in the upper panel.

A few changes have been made to the tomographic processor during the period covered by this report, most of them transparent to the user of these analyses. One change, however, is clear in the image shown in Figure A2: the latitude range of the images produced has been increased from 60° to 72° geomagnetic (see for example Figure 19 in *Andreasen et al.* [2004]) to 56° to 77° geomagnetic. Figure 5 is a plot of relative TEC as a function of the 350 km Ionospheric Penetration Point (IPP) geomagnetic latitude from the data used to generate the image in Figure 5. Shown in this figure is the original (solid box) image coverage and the coverage afforded in the new processing (extensions shown by dashed lines). Note that there are many data paths in the extended region. After an analysis of our processing procedures, we determined that our initial selection of image span was overly conservative and that the data available supported the extension shown. We will be reprocessing all data in our database to regenerate images on this extended range once we have concluded the TEC uncertainty analyses discussed in a later section.

Under the present contract, we have produced 2,970 images from LEO passes over the HAARP tomography chain covering the interval 15 February 2004 through 31 August 2005, all of which were posted on the HAARP Web site. Tables 1 and 2 provide a summary of images generated from the Alaskan tomography network during 2004 and 2005 through the end of August, respectively, as a function of month. The upper panel separates the images by the set of stations used to generate each image. The entries in the columns under "Stations" indicate which stations contributed to the image; for example, the top row lists images generated from the station-set Kaktovik, Fort Yukon, and Delta Junction. The bottom panel shows the percentage of images in each month that included data from the station listed in the left-most column.

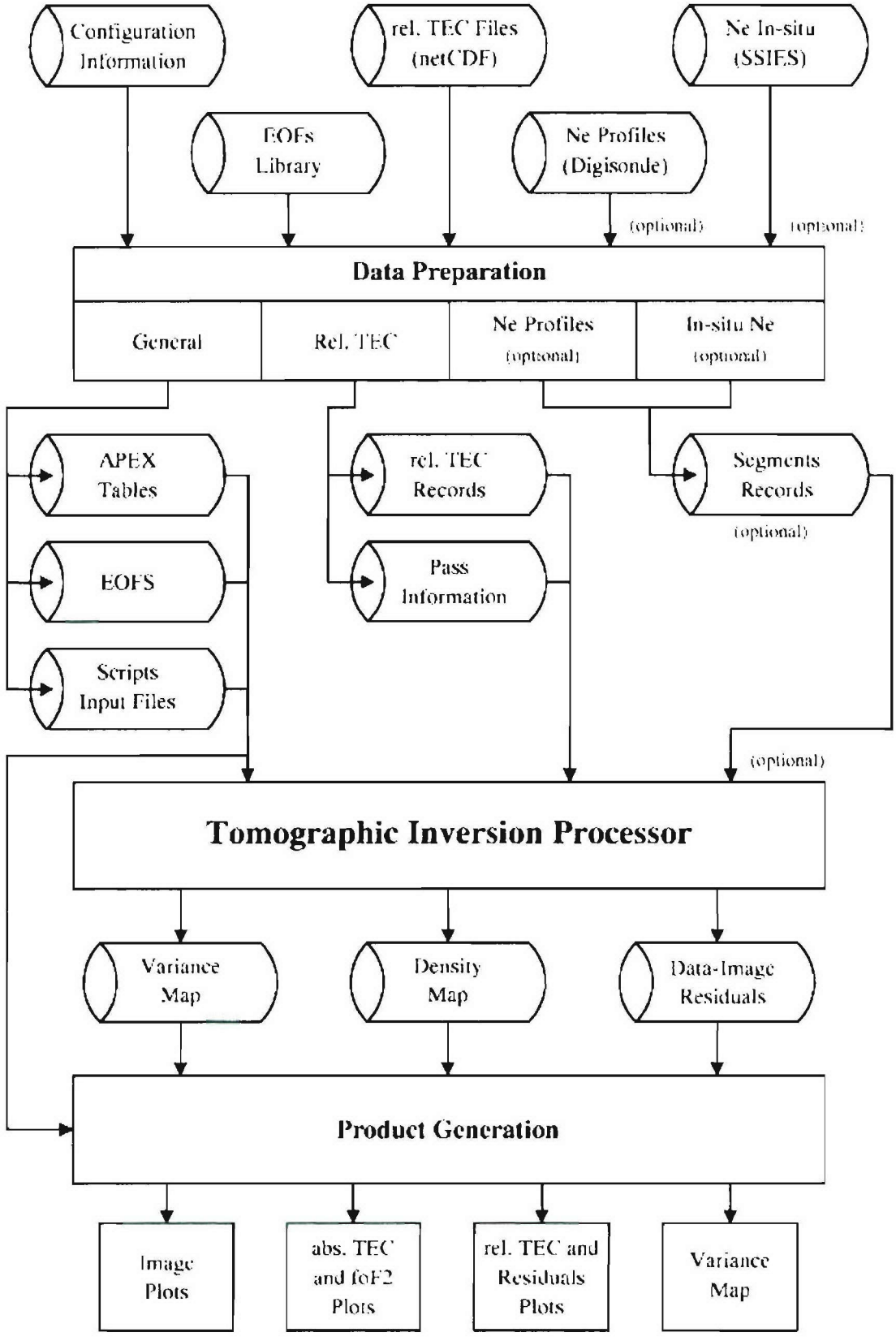


Figure 2. Summary flow diagram for the tomography processing system.

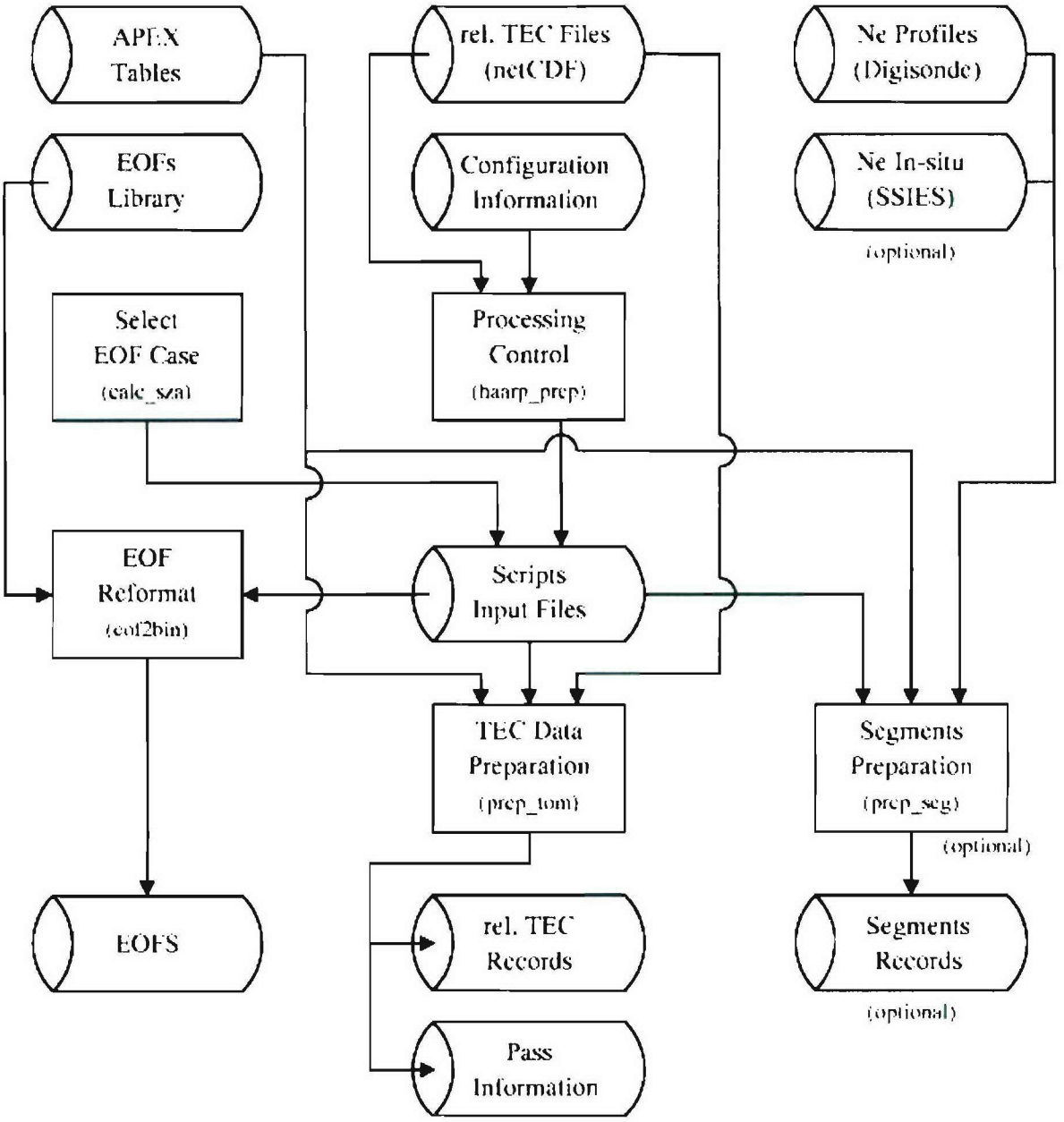


Figure 3. Flow diagram of the data preprocessing section of the tomographic processing system (the block labeled "Data Preparation" in Figure 2).

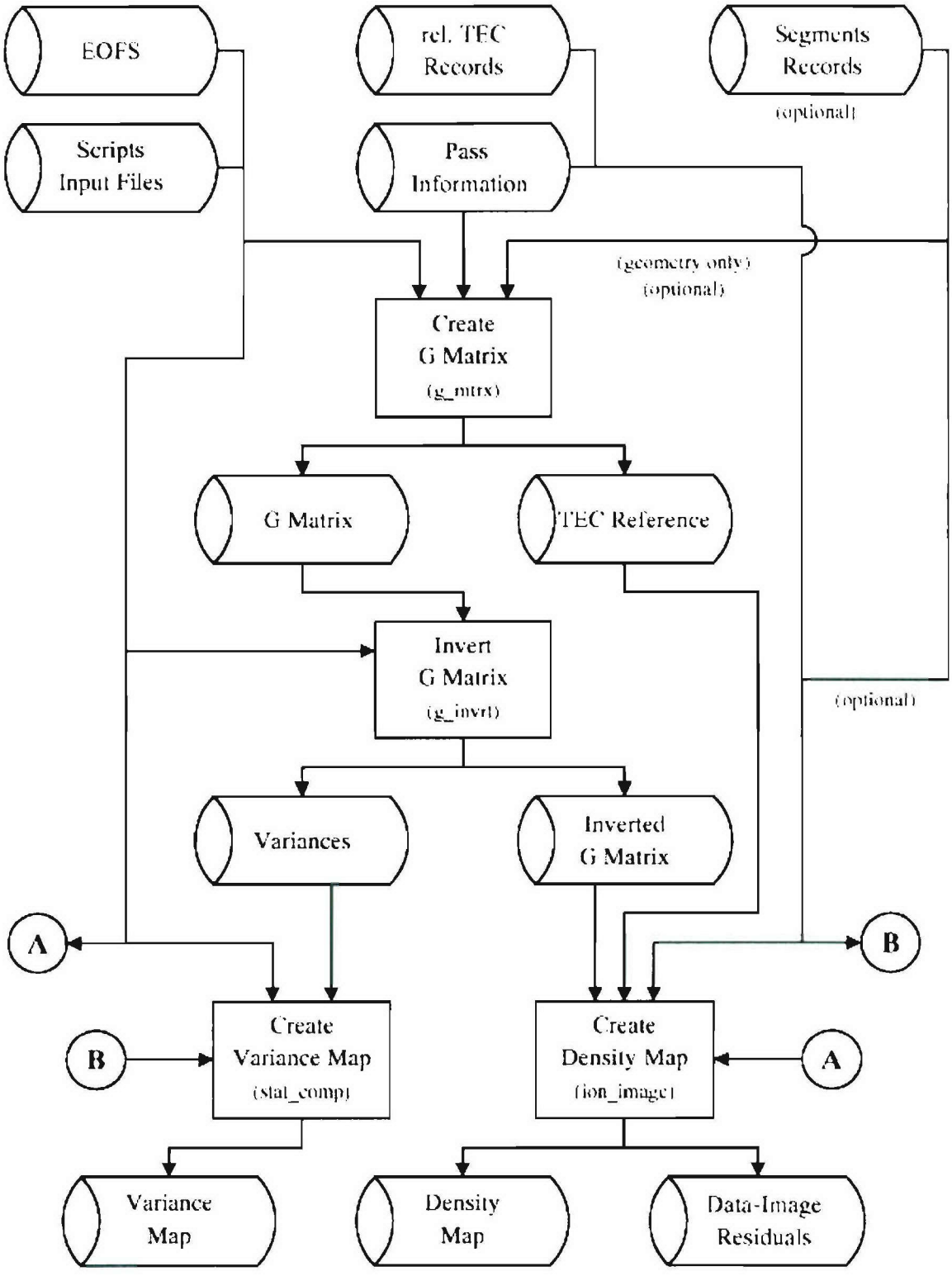


Figure 4. Flow diagram of the tomographic analysis section of the tomographic processing system (the block labeled "Tomographic Inversion Processor" in Figure 2).

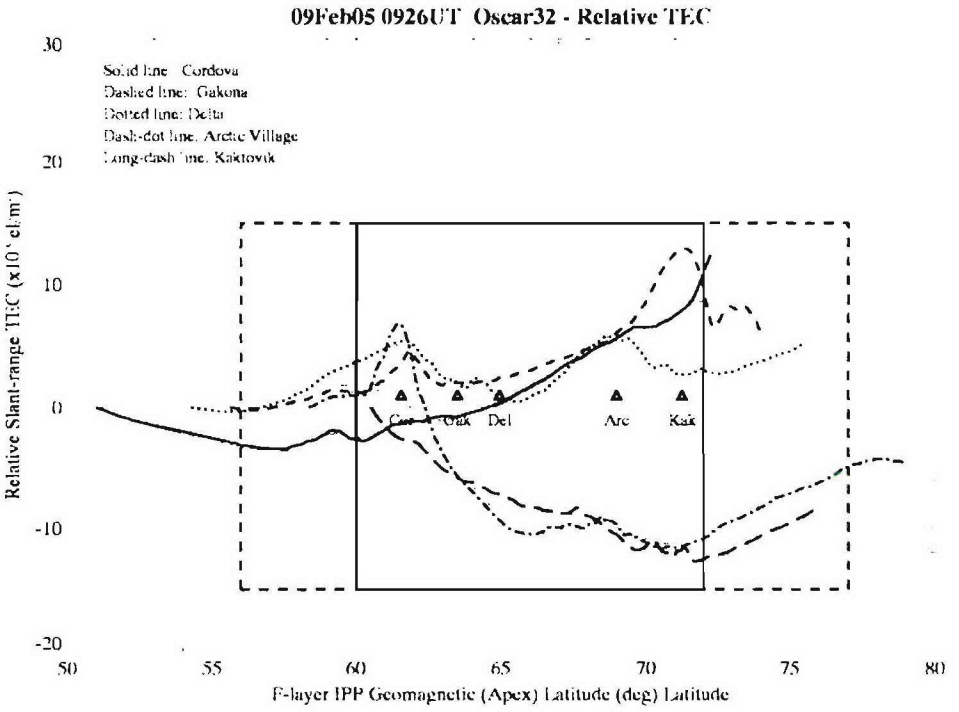


Figure 5. Relative slant TEC from the observations that went into the image shown in Figure A2 in Appendix A. The solid box indicates the image range used until recently, and the dashed lines indicate the extended range of images to be used in processing henceforth.

Table 1. Station-availability summary for tomographic images in 2004.

Number of images

Stations							Jan	Feb	Mar	Apr	May	Jun	Jul	Aug	Sep	Oct	Nov	Dec	All
Kak		For	Del				0	0	0	0	0	0	0	0	0	0	1	0	1
Kak			Del	Gak			0	0	0	0	0	0	0	1	0	0	2	0	3
		For	Del	Gak			0	0	0	0	0	0	0	0	0	0	2	0	2
Kak		For				Cor	0	0	0	0	0	0	0	0	1	1	0	0	2
Kak			Del			Cor	0	0	0	0	0	0	0	0	1	0	0	0	1
Kak				Gak		Cor	0	0	0	0	0	0	1	21	28	0	0	0	50
		For		Gak		Cor	0	0	0	0	0	0	0	0	5	1	0	0	6
	Arc			Gak		Cor	0	0	0	0	0	0	0	0	0	0	0	7	7
			Del	Gak		Cor	191	132	148	128	108	89	130	76	17	56	47	3	1125
Kak		For	Del	Gak			0	0	0	0	0	0	0	0	0	1	1	0	2
Kak		For		Gak		Cor	0	0	0	0	0	0	0	0	15	0	0	0	15
Kak	Arc			Gak		Cor	0	0	0	0	0	0	0	0	0	0	0	2	2
Kak			Del	Gak		Cor	0	0	0	0	0	0	9	38	13	38	21	1	120
		For	Del	Gak		Cor	0	0	0	0	0	0	0	0	6	13	7	0	26
	Arc		Del	Gak		Cor	0	0	0	0	0	0	0	0	0	0	48	111	159
Kak	Arc	For	Del			Cor	0	0	0	0	0	0	0	0	0	0	1	0	1
Kak		For	Del	Gak		Cor	0	0	0	0	0	0	0	0	22	67	29	0	118
Kak	Arc		Del	Gak		Cor	0	0	0	0	0	0	0	0	0	0	27	76	103
	Arc	For	Del	Gak		Cor	0	0	0	0	0	0	0	0	0	0	4	4	8
Kak	Arc	For	Del	Gak		Cor	0	0	0	0	0	0	0	0	0	0	27	31	58
						Summary	191	132	148	128	108	89	140	136	108	177	217	235	1809

Percent of images including specific stations

Station	Jan	Feb	Mar	Apr	May	Jun	Jul	Aug	Sep	Oct	Nov	Dec	All
Kaktovik	0	0	0	0	0	0	7	44	74	60	50	46	26
Arctic Village	0	0	0	0	0	0	0	0	0	0	49	98	19
Fort Yukon	0	0	0	0	0	0	0	0	45	46	33	14	13
Delta	100	100	100	100	100	100	99	84	54	98	100	96	95
Gakona	100	100	100	100	100	100	100	100	98	99	99	100	100
Copper Center	0	0	0	0	0	0	0	0	0	0	0	0	0
Cordova	100	100	100	100	100	100	100	99	100	99	97	100	99

Table 2. Station-availability summary for tomographic images in 2005 (through August).

Number of images

Stations							Jan	Feb	Mar	Apr	May	Jun	Jul	Aug	Sep	Oct	Nov	Dec	All
Kak		For		Gak			0	0	0	0	2	3	15	79					99
	Arc	For		Gak			0	0	0	0	1	0	0	0					1
Kak			Del	Gak			7	0	2	2	7	0	0	0					18
	Arc		Del	Gak			1	2	0	57	0	0	0	0					60
Kak		For				Cor	0	0	0	0	0	0	0	28					28
Kak	Arc					Cor	1	0	0	0	0	0	0	0					1
	Arc		Del			Cor	0	0	2	0	0	0	0	0					2
Kak				Gak		Cor	0	0	0	0	24	79	27	1					131
		For		Gak		Cor	0	0	0	0	2	6	8	1					17
	Arc			Gak		Cor	0	0	0	0	0	1	0	0					1
			Del	Gak		Cor	18	57	18	7	16	0	0	0					116
Kak		For	Del	Gak			0	0	0	0	1	0	0	0					1
Kak	Arc		Del	Gak			3	1	0	32	0	0	0	0					36
Kak		For		Gak		Cor	0	0	0	0	74	62	102	7					245
Kak			Del	Gak		Cor	12	37	15	4	7	0	0	0					75
	Arc		Del	Gak		Cor	111	70	134	47	0	0	0	0					362
Kak		For	Del	Gak		Cor	0	0	0	0	10	0	0	0					10
Kak	Arc		Del	Gak		Cor	62	37	84	32	2	0	0	0					217
	Arc	For	Del	Gak		Cor	0	0	0	0	1	0	0	0					1
Kak	Arc	For	Del	Gak		Cor	0	0	0	0	1	0	0	0					1
						Summary	215	204	255	181	147	151	152	116	0	0	0	0	1421

Percent of images including specific stations

Station	Jan	Feb	Mar	Apr	May	Jun	Jul	Aug	Sep	Oct	Nov	Dec	All
Kaktovik	39	36	39	38	86	95	94	99					60
Arctic Village	82	53	86	92	3	0	0	0					47
Fort Yukon	0	0	0	0	62	47	82	99					28
Delta	99	100	100	100	30	0	0	0					63
Gakona	99	100	99	100	100	100	100	75					98
Copper Center	0	0	0	0	0	0	0	0					0
Cordova	94	98	99	49	92	98	90	31					84

2.1.2 GPS Data Sets

NWRA operated an Ashtech Z-FX Continuously Operating Reference Station (CORS), consisting of a 12-channel GPS receiver and an antenna, at the HAARP Gakona facility for the entire period covered by this report. Data collection is performed by means of the NWRA GPS Ionospheric Observation System (GIOS) program, supplemented by a real-time process to convert raw data records from the GIOS software into calibrated estimates of equivalent vertical TEC (VTEC) using the SCORE (Self-Calibration of Range Errors) process developed by NWRA for the USAF Ionospheric Measuring System (IMS) instruments (*Bishop et al.*, 1995). These data are stored in a database and are used to generate plots of absolute TEC displayed on the HAARP Web site. Two different types of plots are produced from the GPS TEC data, examples of which are shown in Appendix A (Figures A3 through A7).

Note in the caption to Figure A5 that the plot shown in this figure includes not only GPS-derived VTEC estimates, but also VTEC estimates from LEO data. These latter estimates are generated from the relative slant TEC provided from the LEO receivers to estimates of VTEC using a modified version of the SCORE process as described in *Mazzella et al.* (2001).

In addition to the Ashtech Z-FX system, NWRA also operates a GPS-based CNS Clock as a time standard for the NWRA ITS10S receiver located at Gakona. This clock uses a single-frequency GPS receiver chip set (Motorola Oncore UT+) that can also provide estimates of the receiver location. We use these data to measure the position error in these estimates by comparing the instantaneous position estimates to estimates derived from long-term averages of the receiver location. The departures of the instantaneous positions from the average positions, both in the horizontal and vertical directions, are plotted as shown in Figure A8 in Appendix A.

These plots show up to 36 hours of data, and the horizontal data are fitted by an rms-based error ellipse, which can be seen plotted over the horizontal data in Figure A8.

All of the GPS data described in this section are archived at either the HAARP site or on servers at NWRA's Bellevue office.

2.2 Tomographic Image Uncertainty Specification

2.2.1 Background

While TEC-based tomography has been validated by comparison with latitude-altitude maps of plasma density obtained by means of incoherent scatter (*Kersley et al.,* 1993), the technique does rely on some *a priori* information to augment the TEC data used as input to the inversion. In the NWRA ITS processor, the incompleteness stems from the sparseness of the matrix to be inverted. The primary cause of the sparseness is lack of horizontal rays from the satellite-borne transmitter to the ground-based receiving stations through the region being imaged.

Lack of an effective vertical scan by horizontal rays degrades vertical resolution and limits efficacy of vertical profiles incorporated into the image. Information lacking from missing rays, including those with grazing angles shallower than those of the lowest-elevation raypaths passing through the imaged region from the satellite to the northern-most and southern-most receivers, is approximated by an *a priori* background ionosphere. The anticipated variability of the ionosphere relative to the *a priori* background is described by means of empirical orthogonal functions (EOFs). The TEC data are used to evaluate coefficients that quantify the vertical EOFs and their horizontal counterparts, which are Fourier sines and cosines. The basis functions so quantified are added to the *a priori* background to produce the image.

The stochastic inverse theory that underlies the NWRA ITS inversion processor includes a means for estimating formal error in the resulting images. The formalism accounts for the geometrical deficiencies described in the foregoing and for uncertainties imposed by estimated data (receiver and sky) noise. It does not account, however, for all sources of error. For instance, the algorithm assumes straight-line propagation through the ionosphere and that the EOFs employed in the processor fully span the ionospheric states to be encountered. Under this contract, we have devised an empirical approach to accounting for those sources of error overlooked in the formalism.

2.2.2 The Formalism and Its Scaling

The NWRA ITS processor employs weighted, damped, least-squares (WDLS) matrix inversion. The image produced thereby constitutes a field of estimated plasma density. As described by *Fremouw et al.* (1990), the variances of those estimates may be obtained from a (diagonal) covariance matrix, **V'**, computed from the estimated covariance matrix, **V**, of the *a priori* ionospheric model, as follows:

$$\mathbf{V'} = (\mathbf{I} - \mathbf{G}^{-g}\mathbf{G})\mathbf{V} , \qquad [1]$$

where **I** is the identity matrix, **G** is a matrix describing the integration of plasma density along raypaths, which produces the observed TEC, and $\mathbf{G}^{-g}$ is a generalized inverse of **G,** which produces our plasma-density estimates while accounting for noise in the measured TEC data and

other sources of error. Under an earlier contract, we implemented code to perform this calculation and developed graphics procedures to display its results (*Andreasen et al.,* 2003). Those results, however, were deficient by virtue of the formalism's ignoring sources of error such as those described in the foregoing subsection.

Due to the matrix product $\mathbf{G}^{-g}\mathbf{G}$, the displays did show expected behaviors such as increased uncertainty (a) between receiving stations, where path-length and antenna-pattern effects reduce S/N, and (b) near the edges of the image in pixels that contain few crossing rays. The absolute uncertainty levels in those displays, however, were unrealistically low, for reasons that we now understand.

It is obvious from Equation [1] that the formal uncertainty estimate, $\mathbf{V}'$, scales directly as one's *a priori* estimate of ionospheric variability, $\mathbf{V}$, which we obtain in the following way. From a database of many "ionospheres" (generated originally by running an ionospheric model for many sets of input parameters), we glean (a) estimates (expectation values) of plasma density in latitude/altitude bins, which describe the average, background ionosphere, and (b) a set of EOFs that span the database. The variances associated with the EOFs describe ionospheric variability about that background, or *a priori* image. The *a priori* image is refined (usually altered substantially) by means of the TEC data and the inversion processor.

We also estimate data uncertainty due to receiver noise. So long as we have appropriately estimated the uncertainty in the *a priori* image (i.e., the *a priori* variance) and in the data, Equation [1] produces an estimate of *a posteriori* uncertainty in the resulting WDLS image. Our best estimate of data error (RMS uncertainty in dispersive phase) related to S/N on the various rays, accounting for elevation-dependent range-squared error and antenna patterns, is incorporated in $\mathbf{G}^{-g}$. In terms of the WDLS formalism, this leaves open only the question of whether we have appropriately estimated the *a priori* variance, $\mathbf{V}$.

The distribution of variance among the elements of the vector $\mathbf{V}$ somewhat affects the WDLS image, but the magnitude of that vector does not appreciably do so. This fact provided an opportunity to ascertain that originally we had underestimated the magnitude of $\mathbf{V}$. To improve upon the estimate, we employed over two year's worth of images as an enlarged database of auroral/sub-auroral ionospheres, regenerating new EOFs and their corresponding variances therefrom. That is, we rescaled $\mathbf{V}$ in accord with the variability we had experienced via our Alaska observations.

Using the new results, we regenerated a variety of images and found that they did not differ significantly from those employing the original EOFs because the distribution of variance among the elements of $\mathbf{V}$ had not changed appreciably. The magnitude of $\mathbf{V}$ (and therefore of $\mathbf{V}'$) had increased, however, by a factor of 3 for daytime and twilight cases and a factor of 13 for nighttime cases. That is, the ionosphere we imaged over a period of two years was appreciably more variable than the cases contained in our original *a priori* (model) database.

2.2.3 Empirical Calibration of the Formal Estimates

The foregoing consideration still overlooks some sources of uncertainty (e.g., the extent to which the chosen EOFs span the actual ionospheres to be imaged and the effects of ionospheric

refraction). Under this contract, we have developed an approach to augmenting the formal-error estimation procedure with information about the error sources it neglects. We began by investigating uncertainty imposed by our choice of EOFs, over and above that accounted for by rescaling their aggregate *a priori* variance, **V**.

Earlier (*Fremouw et al.*, 1997, and further unpublished analysis), we had explored the effects of employing EOFs chosen to span only a subset of "all possible ionospheres." Based on that investigation, we chose to tailor the EOFs used for Alaskan tomography to high latitudes (greater than 55° geomagnetic) and by solar elevation angle (el < -20° being deemed "nighttime," -20° < el < 20° deemed "twilight," and el > 20° "daytime").

In addition to guiding our tailoring of EOF selection, the aforementioned investigations provided information on the uncertainties engendered by doing so. The investigations employed four renderings of the ionosphere from incoherent-scatter radar (ISR) measurements, a daytime and a nighttime mid-latitude case using ISR data from Arecibo, PR, and a daytime and a nighttime case using ISR data from Chatanika, AK.

Generally (although not uniformly), the mid-latitude cases revealed smaller errors. Since tomographic imaging under this contract occurs at high latitudes, we focused our attention on those results. With EOFs chosen for high latitudes, season (winter) and time of day (simply local day or local night), we applied our (rescaled) algorithm to the daytime and a nighttime Chatanika ISR cases.

Taking the ISR renderings as "truth," we integrated through them on slant paths from a satellite at 1000 km altitude to five ground stations equally spaced over a latitude span of 12°. We then used the integral records as simulated TEC data and input them to the ITS processor. Qualitatively the tomographic images obtained appeared as rather faithful reconstructions of the ISR renditions, displaying no false features, although not resolving the peaks of high-density features.

Quantitatively we compared the resulting images to the ISR "true" renderings of the ionosphere, calculating differences in f_oF2, h_mF2, and the vertical integrals (VTEC) through the renderings and the images, as well as vertical profiles of the average and RMS differences in plasma density, N_e. In addition to showing greater disparities near the edges of the images (especially the daytime one) than in their interior, the various differences between the "true" ionospheres and the tomographic images thereof included the following:

- f_oF2 within a little over 1 MHz of that in the day time ISR mapping and mostly well within 1 MHz in the night case;
- h_mF2 overestimated by about 10 km in the day case and underestimated by about 25 km in the night case;
- VTEC overestimated by about 0 to about 4 TECu in the day case and mostly within about 1 TECu in the night case;
- average vertical-profile shapes close to their "true" counterparts, especially in the night case while somewhat less peaked in the day case, with a maximum error of -1.5×10^{11} el/m^3 just below the day time F-layer peak and -0.4×10^{11} in the night-time auroral E layer;

- RMS difference profile peaking in the bottomside F layer at about 2.8 x 10^{11} el/m^2 in the day case and in the auroral E layer at about 1.1 x 10^{11} in the night case.

We also computed the (rescaled) formal error by means of the WDLS procedure, which produces a field of RMS uncertainty in N_e in the same coordinate system in which the N_e images are presented. Visual inspection of the uncertainty fields suggested that their average RMS uncertainty profiles were qualitatively similar to those of the RMS difference profiles computed from the foregoing error-assessment procedure. As expected, however, the magnitudes of the RMS errors computed formally still were substantially smaller than those of the complete RMS differences found empirically in the two Chatanika ISR cases.

After computing the formal errors for the Chatanika cases by means of the WDLS procedure (performed in Program "StatComp" of the ITS processor), we computed the average vertical profiles in the resulting altitude-latitude fields of (formal) RMS uncertainties. We then formed the ratios between the average RMS difference profiles obtained empirically and the average formal-error profiles. The results are shown in Figures 6a and 6b for the daytime and nighttime cases, respectively.

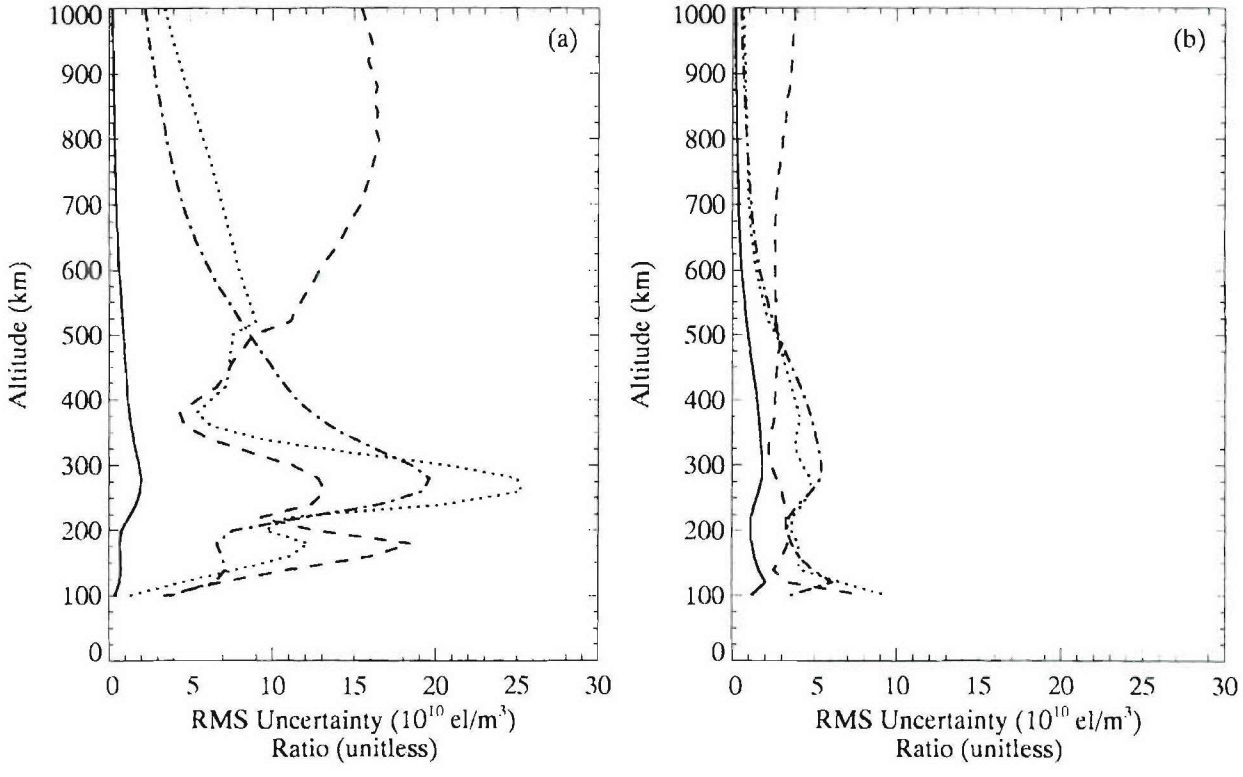


Figure 6. Comparison of error and difference profiles for (a) daytime and (b) nighttime cases. Solid curves are vertical profiles of formal errors; dotted curves are RMS difference profiles between the tomographic image and the corresponding Chatanika ISR record; dash curved are the ratio of these two; and the dot-dash curves are 10 times the formal error for (a) and 3 times for (b).

The foregoing comparisons verified that the true uncertainty in our tomographic images is substantially greater than the formal errors computed by the WDLS formalism (even after rescaling **V** and **V'**). They also suggested that the average vertical profile of those errors may provide a reasonable guide for quantifying the uncertainty field. [The discontinuity in the daytime RMS difference profile (light squares) in Figure 6a is due to inadequate topside measurements in the ISR record, which was extended by means of a model.]

Both the procedure for calculating formal error and the ISR-based EOF study (especially the daytime case) revealed larger uncertainties near the edges of images than elsewhere. In view of this similarity and taking guidance from the similarity in their vertical profiles of uncertainty, we proceeded to "calibrate" the formal errors by means of the empirical results, relying especially on the RMS difference profiles. Next, we compared the resulting estimates of f_oF2 and h_mF2 uncertainties with differences between those parameters scaled from a selected set of our tomographic images and nearly simultaneous ionosonde measurements, and then recalibrated our uncertainty estimates based on that comparison.

To assemble the information necessary for the ionosonde comparison, we first selected 54 images for which appropriate auto-scaled ionograms were available from the Gakona Digisonde and compared overhead values of f_oF_2 and h_mF_2 from the two data sources. For f_oF2, the correlation was 83%; the mean and median differences between the tomographic values and those from the ionosonde were, respectively, -0.16 and -0.17 MHz. The mean (median) absolute difference in f_oF2 was 0.38 (0.28) MHz. We also ranked the ionograms by "quality" according to a scale ranging from "excellent" to "spread with severe frequency gaps" (the latter stemming from frequencies excluded from the Digisonde's transmission license). Our results included an upward trend in absolute difference with decreasing ionogram quality.

The initial Digisonde comparison described above employed tomographic images derived from only three TEC recording stations, which is minimal. We next proceeded with a somewhat more rigorous comparison of five-station images and ionograms from Gakona and Sheep Creek (near College), AK. We selected 55 such images for which suitable auto-scaled ionograms were available from Gakona and 62 for which such were available from Sheep Creek. NWRA consultant A. Lee Snyder then employed the GAO Explorer tool developed by the University of Massachusetts at Lowell to re-scale them manually where improvements could be made. Again, we calculated differences between f_oF2 and h_mF2 values scaled from our images and those obtained from the manually scaled ionograms.

As was true for the three-station images, the five-station ones underestimated f_oF2 by substantially less than one MHz on average (-0.36 MHz at Gakona and -0.26 MHz at Sheep Creek) and with an absolute disparity of about one MHz (0.69 and 0.94 MHz, respectively). The respective standard deviations were 1.32 and 1.17 MHz. These results and those of our ISR-based investigation both suggest uncertainties of $^{\pm}1$ to $^{\pm}2$ MHz in the f_oF2 values scaled from our tomographic images. For purposes of augmenting the calculation of formal errors in our images, we converted this uncertainty and that found for h_mF2 to uncertainty in N_e near the F-layer peak and then extrapolated that uncertainty by means of the vertical profiles of N_e differences (primarily RMS values) indicated in Figure 6.

To provide this further quantification, we first divided 63 five-station tomographic images for which Dr. Snyder had manually re-scaled ionograms from Gakona and/or Sheep Creek into daytime, nighttime, and twilight groups. Then, based on a refinement of the results displayed in Figure 6, we multiplied the formal errors computed for the three groups by 4, 12, and 20, respectively, and computed the corresponding RMS uncertainty in f_0F2.

Taking the manually scaled ionosonde values as the standard for accuracy, the disparities in f_0F2 indicated a median tomographic underestimate by 0.5 MHz and a worst-case underestimate by 2.5 MHz. Our -RMS uncertainty calculation fell above the ionosonde f_0F2 value in only one case, but our +RMS calculation fell below the ionosonde value in 26 cases. Moreover, our tomographic images underestimated the f_0F2 values obtained from the carefully scaled ionograms increasingly as ionospheric density increased.

We then proceeded to refine our uncertainty estimation further, in the direction of lengthening the uncertainty bars with increasing ionospheric density. In this further refinement, rather than using discrete multipliers for three subsets of images, we established a simple law that describes continuously increasing uncertainty with increasing ionospheric density. Namely, we multiply the formal errors by (1 + m) times the average value of N_mF_2 (the maximum value of Ne at a given latitude) across the latitude span of the image being assessed. With N_mF_2 expressed in units of 10^{11} el/m^3, we set m = 1.2 as determined empirically from the ionosonde comparison, subject to a limit for the RMS uncertainty in Ne as 95% of its estimated (expectation) value since the actual value of N_e cannot be negative.

We established a similarly simple procedure for dealing with our images' underestimation of f_0F2 and the trend therein. The uncertainty in our images is expressed as the RMS error in N_e in each pixel. The value thereof at the peak of each vertical N_e profile (i.e., N_mF2) may be converted to an RMS uncertainty in f_0F2, but it contains no information about the sign of the latter uncertainty. Since our comparison with carefully scaled ionosonde values of f_0F2 does reveal a bias, we have additional information at our disposal.

Based on the ionosonde database and our two Chatanika ISR comparisons, we have devised a procedure to deal with this systematic bias. Specifically, we shift our computed f_0F2 error bars in accord with the following simple formula: upshift = $a(f_0F_2 - b)$, where the constants a = 0.1 and b = 0.3 MHz were determined empirically. Since, again, the actual value of f_0F2 cannot be negative, we limit its RMS uncertainty to 97% (determined primarily from details in the two Chatanika ISR comparisons) of its estimated value.

Aggregate results of all the foregoing procedures are illustrated in Figure 7 which compares the image-generated values of f_0F2 (y-axis values of the dark diamonds) and their computed uncertainties with the values of f_0F2 (x-axis values) obtained from the carefully scaled ionograms. The dark solid line represents the linear trend of the f_0F_2 points (dark diamonds). Its shallow slope compared with the dashed diagonal quantifies the manner in which our tomographic images underestimate the f_0F2 values obtained from the carefully scaled ionograms—namely, increasingly so as ionospheric density increases. The blue lines represent the linear trends in our ±RMS uncertainty estimates, showing the upshift we've imposed to accommodate our images' underestimation of f_0F2 and, to some extent, the trend therein.

Again, taking the manually scaled ionosonde values as the standard for accuracy, the disparities in f_0F2 indicated a median tomographic underestimate by 0.5 MHz and a worst-case underestimate by 2.5 MHz. Our -RMS uncertainty calculation fell above the ionosonde f_0F2 value in only 8 cases, and our +RMS calculation fell below the ionosonde value in 23 cases. Thus 52% of the disparities between the tomographic and ionosonde f_0F2 values fell outside our span of calculated uncertainty. For a normal distribution, 32% would do so. In this statistical sense, our uncertainty bars (spans between f_0F2+RMS and f_0F2-RMS) still are too short.

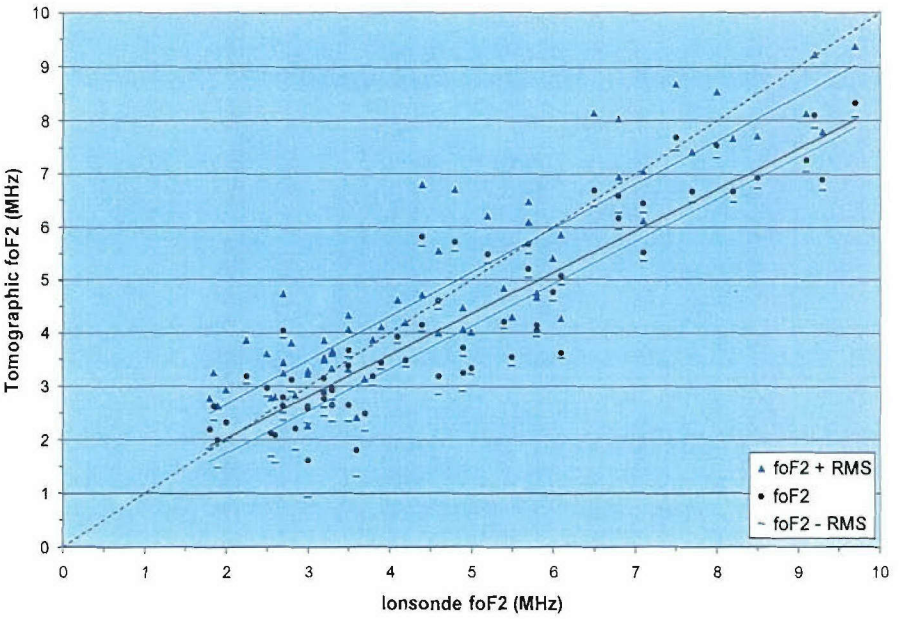


Figure 7. Comparison of f_0F2 values (dark diamonds) obtained from 63 tomographic images and their estimated ±RMS uncertainties (lighter blue symbols) with f_0F2 values (x-axis) obtained from nearly simultaneous ionograms.

Somewhat different values of m, a, and b can improve the aforementioned aggregate statistics, but only at the expense of less favorable estimation of specific uncertainties in our two Chatanika cases. Results of applying the procedure to those cases are illustrated in Figure 8. In the nighttime case (Figure 8a), all but 8 (22%) of the 37 "true" values fall within the uncertainty range. In the daytime case (Figure 8b), all but 10 (28%) of the 35 points in the common latitude span do so. We have accepted the combined results from the aggregate ionosonde comparisons and the two ISR case studies as the best we can do with the existing database and other resources available.

Finally, we show the intended use of our uncertainty estimation in Figure 9. Using the Chatanika daytime case for purposes of illustration, Figure 9a shows a modification of our current tomographic posting on the HAARP Web site. The upper panel contains the ionospheric image, while the lower panel presents f_0F2 and vertical TEC scaled therefrom. The modification consists of displaying the upper and lower uncertainty estimates above and below the f_0F2 plot. We intend to provide the viewer with a linked alternative display, illustrated in Figure 9b. The alternative again shows the image in the top panel, but the lower panel is replaced with the full uncertainty field estimated for the image.

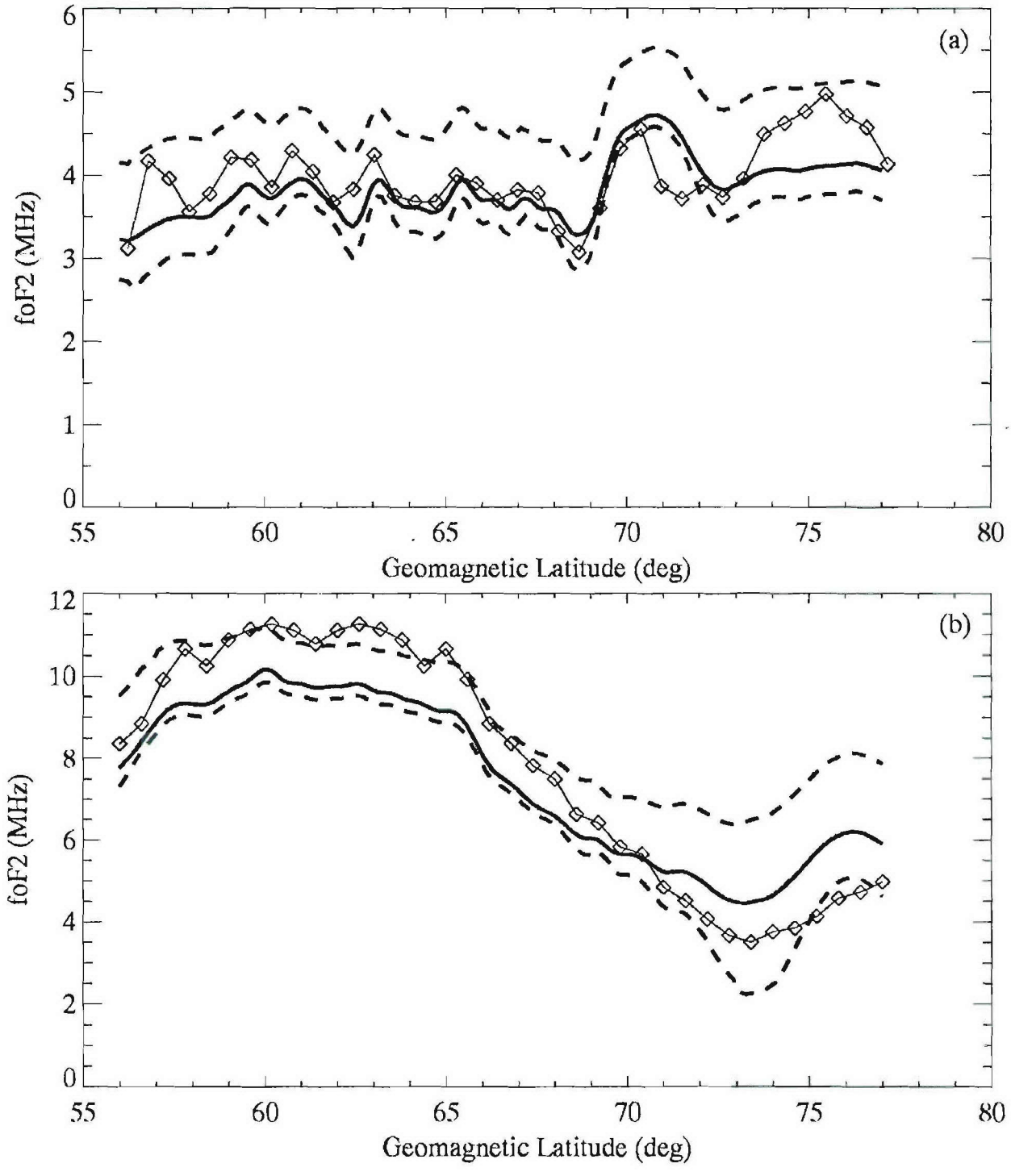


Figure 8. Comparison of f_0F2 values (solid line) derived from tomographic reconstruction of (a) nighttime and (b) daytime Chatanika ISR records and their estimated ±RMS uncertainties (dashed lines) with f_0F2 values (diamonds) scaled from the ISR record.

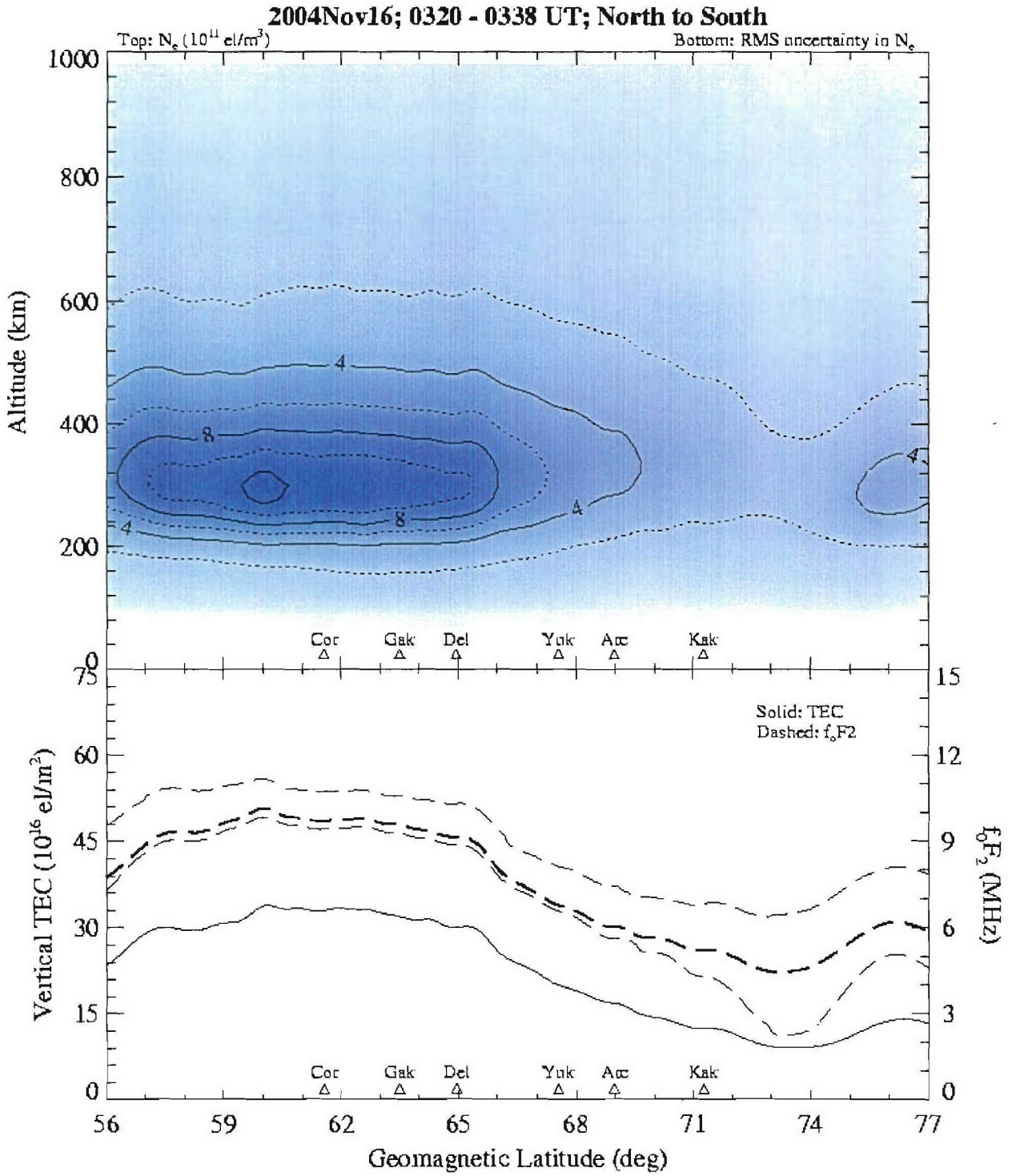


Figure 9a. Example (Chatanika daytime case) of presentation intended for posting on the HAARP Web site, showing tomographic image on top and f_0F2 with its uncertainty band, along with VTEC on the bottom.

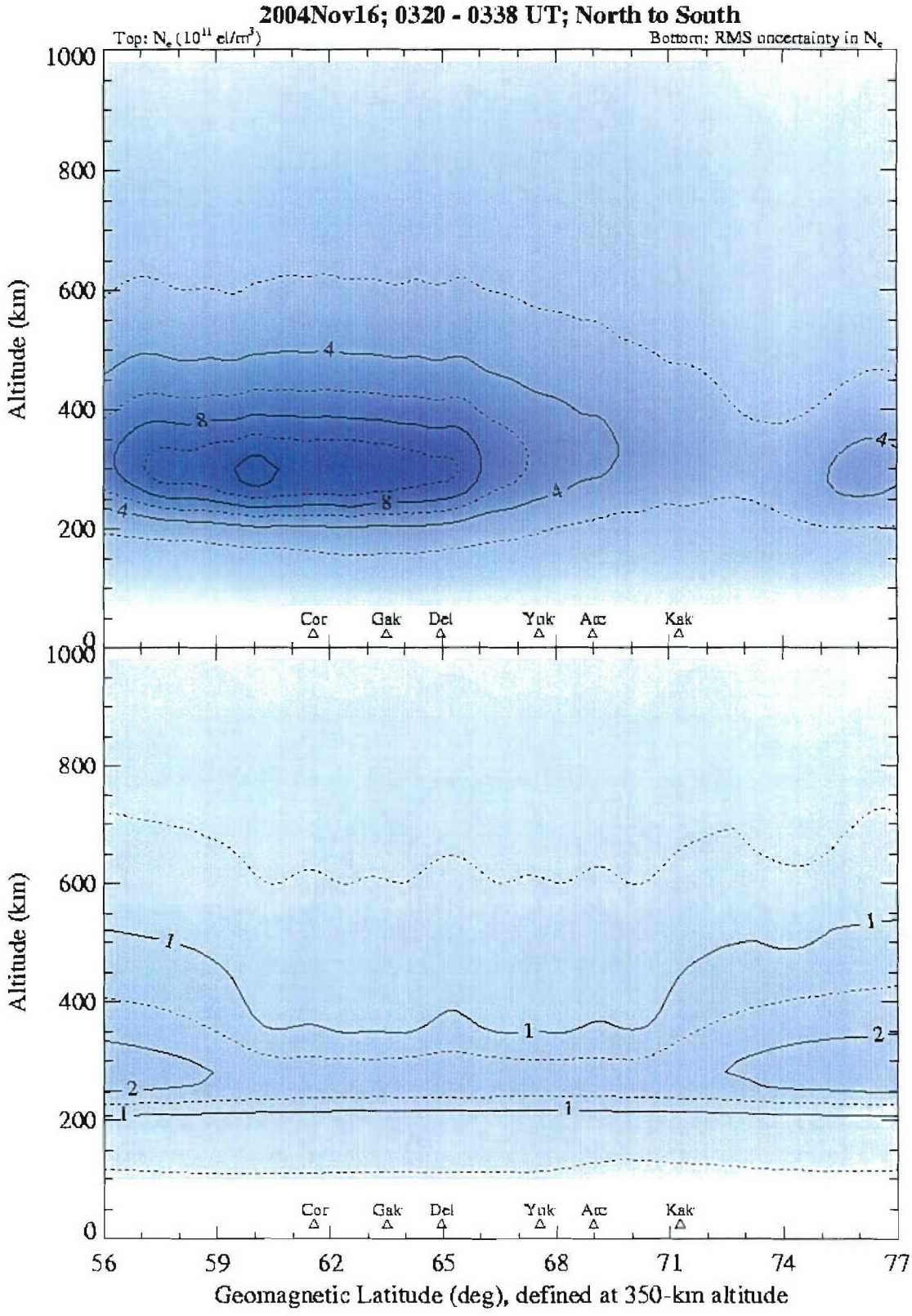


Figure 9b. Example (Chatanika daytime case) of alternate presentation intended for posting on the HAARP Web site showing tomographic image on top and uncertainty field on bottom.

2.2.4 Uncertainty in Vertical TEC

One of AFRL's early motivations for promoting the development of ionospheric tomography was as a means for converting slant-path measurements of TEC into values of vertical TEC. We have served this motive by integrating vertically thorough our images and presenting the result as in the lower panel of Figure 9a. The task then arises to estimate the uncertainty in such displays. Performance of the task should be possible once uncertainties in the images, as illustrated in the lower panel of Figure 9b, have been established. The question also arises, however, as to what the vertical correlation distance of those uncertainties in N_e may be. We intend to pursue this question and task in the next phase of this contract.

2.3 Comparison of Tomography and Digisonde Observations

Since December 1999, comparisons between vertical TEC estimates calculated from Digisonde profiles (*Reinisch and Huang,* 2001) and equivalent vertical TEC derived from GPS measurements have displayed a substantial and systematic difference during local daytime hours (*Fremouw et al.,* 2000). The availability of vertical TEC derived from integration of tomographic images presented an opportunity for resolving this discrepancy because the tomography results provide comparative data for both the Digisonde density profiles and the GPS TEC measurements.

A stepwise comparison of the distinctive measurements derived from the Digisonde, Transit receivers, and GPS receiver was performed, in order to seek the possible sources of the discrepancy in these measurements. Resolution of these discrepancies would provide an increased assurance of the accuracy of TEC measurements, but even a quantification of the discrepancies would provide an error assessment for ionospheric observations.

A review conducted in October 2004, for data from 12 September 2004, indicated that the discrepancy was still present, as displayed in Figure 10. Consequently, procedures and programs were developed to process the various data sources and display appropriate comparisons. The particular steps of the processing are:

Retrieve the Standard Archive Output (SAO) files for the Digisonde data;

Retrieve the tomography image files;

Retrieve the GPS TEC report files;

Extract densities and TEC from the SAO files;

Select GPS equivalent-vertical TEC values above a specified elevation threshold (65°);

Extract densities and TEC from the tomography files;

Display vertical TEC from GPS, Digisonde, and tomography versus time;

Display electron density altitude profiles for the Digisonde and tomography;

Integrate electron density altitude profiles over a selected range (bottomside, topside, all, interval) for further comparisons.

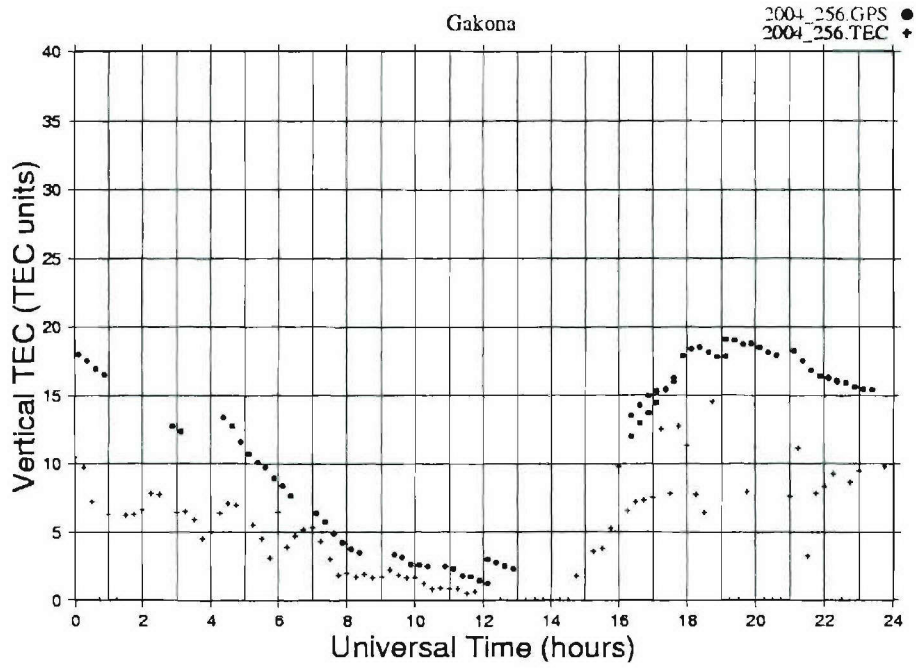


Figure 10. Vertical (or equivalent-vertical) TEC for GPS (o) and Digisonde (+) measurements for 12 September 2004, displaying the predominant TEC discrepancy between the GPS and Digisonde values during the daytime periods (0-4 UT and 15-24 UT).

The preliminary case study spanned the period 9 June 2004 to 22 June 2004 using Digisonde data with data quality assessments in the highest three quality ranks (1, 2, and 3). This resulted in 20 cases of Digisonde density profiles with corresponding tomography profiles, on 11 different days (June 11-14, 16-22). For this set of days, there was generally a good TEC match between the Digisonde and GPS (Figure 11), with some possible offset effects from the GPS calibrations. However, comparisons of the Digisonde and tomography altitude profiles (Figure 12) displayed discrepancies even for a close TEC correspondence. Because the topside density profile from the Digisonde is determined solely by the scale height and density at the peak of the profile, some discrepancies from the tomography could be expected for that region, but the discrepancies for the bottomside density profiles are also significant. For either the Digisonde or tomography, the TEC associated with the bottomside region is about one-third of the entire vertical TEC (to 1000 km altitude). Despite the differences in the altitude profiles, the vertical TEC values determined from the Digisonde and tomography agree quite well for this case (within 1 TEC unit).

Further comparisons were conducted for data from 28 October 2004 and 29 October 2004, with both days displaying the TEC discrepancy previously observed between the Digisonde and GPS values (Figure 13). Unfortunately, 28 October lacked tomography results during the daytime period when the TEC discrepancies occurred (20 - 24 UT), but for 29 October, when several Digisonde/GPS/tomography comparisons were possible (Figure 14), the density profiles all were too discordant for definitive conclusions. However, the Digisonde scans for this day were not reviewed in the same manner as the June data, so some measurement difficulties could have influenced those results.

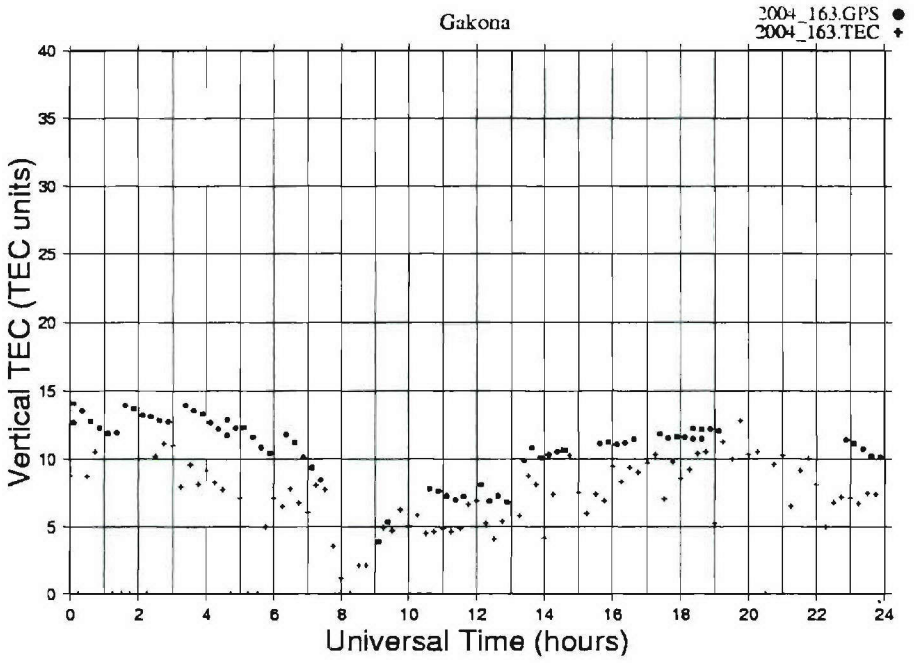


Figure 11. Vertical (or equivalent-vertical) TEC for GPS (o) and Digisonde (+) measurements for 11 June 2004 (day 163). Note that the period from 7-11 UT is local night for Gakona, Alaska, for this date. The TEC discrepancy displayed in Figure 10 is essentially absent for this day.

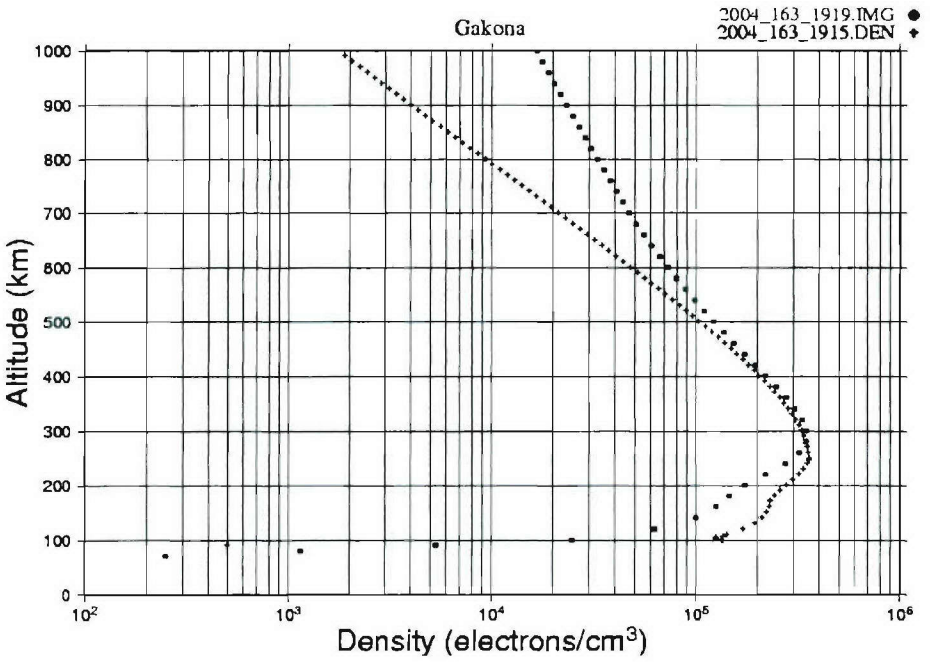


Figure 12. Density profile from tomography (o) for 19:19 UT on 11 June 2004 (day 163), with derived Digisonde density profiles (+) at 19:15 UT.

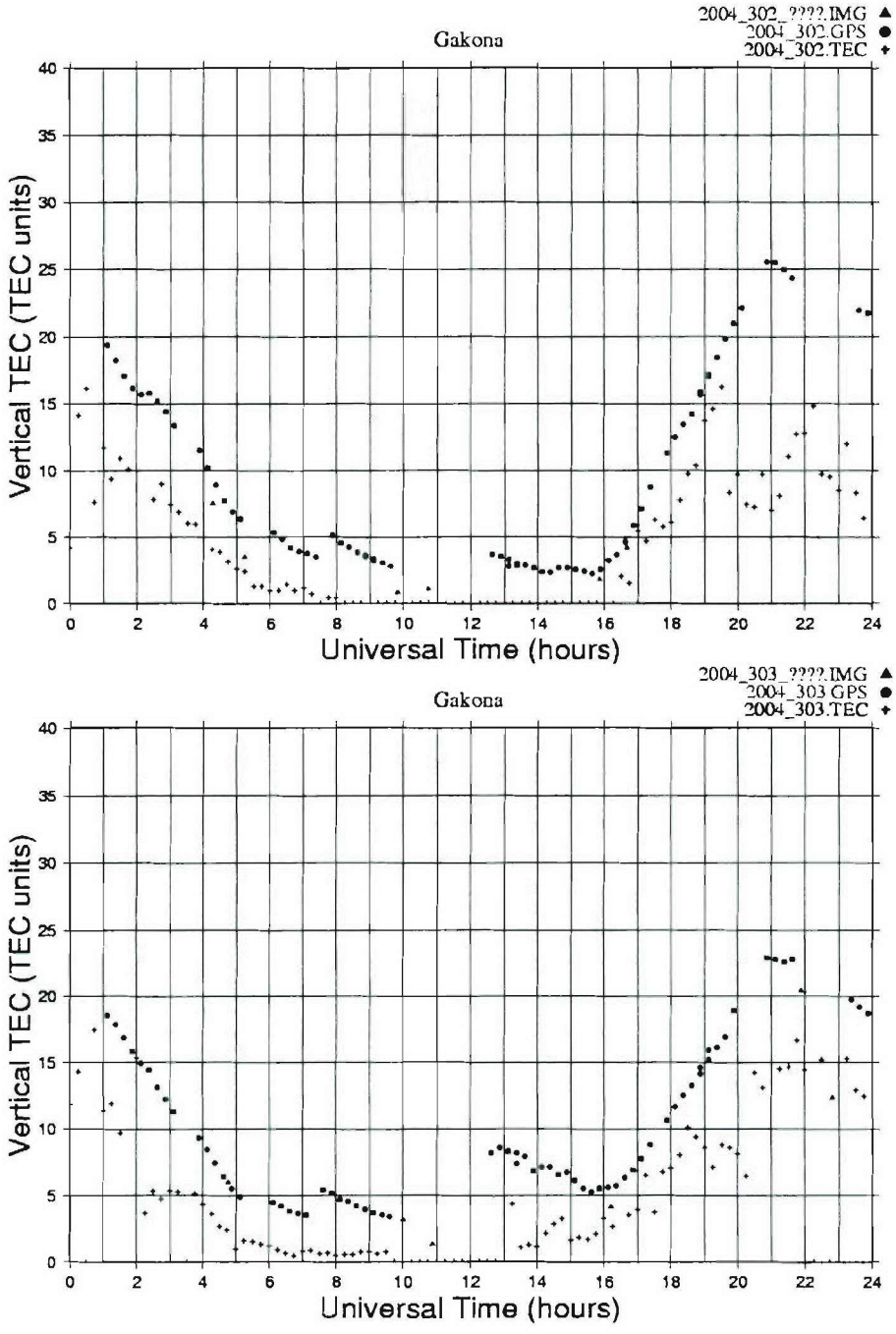


Figure 13. Vertical (or equivalent-vertical) TEC for tomography (Δ), GPS (o), and Digisonde (+) measurements for 28 October 2004 (day 302) and 29 October 2004 (day 303).

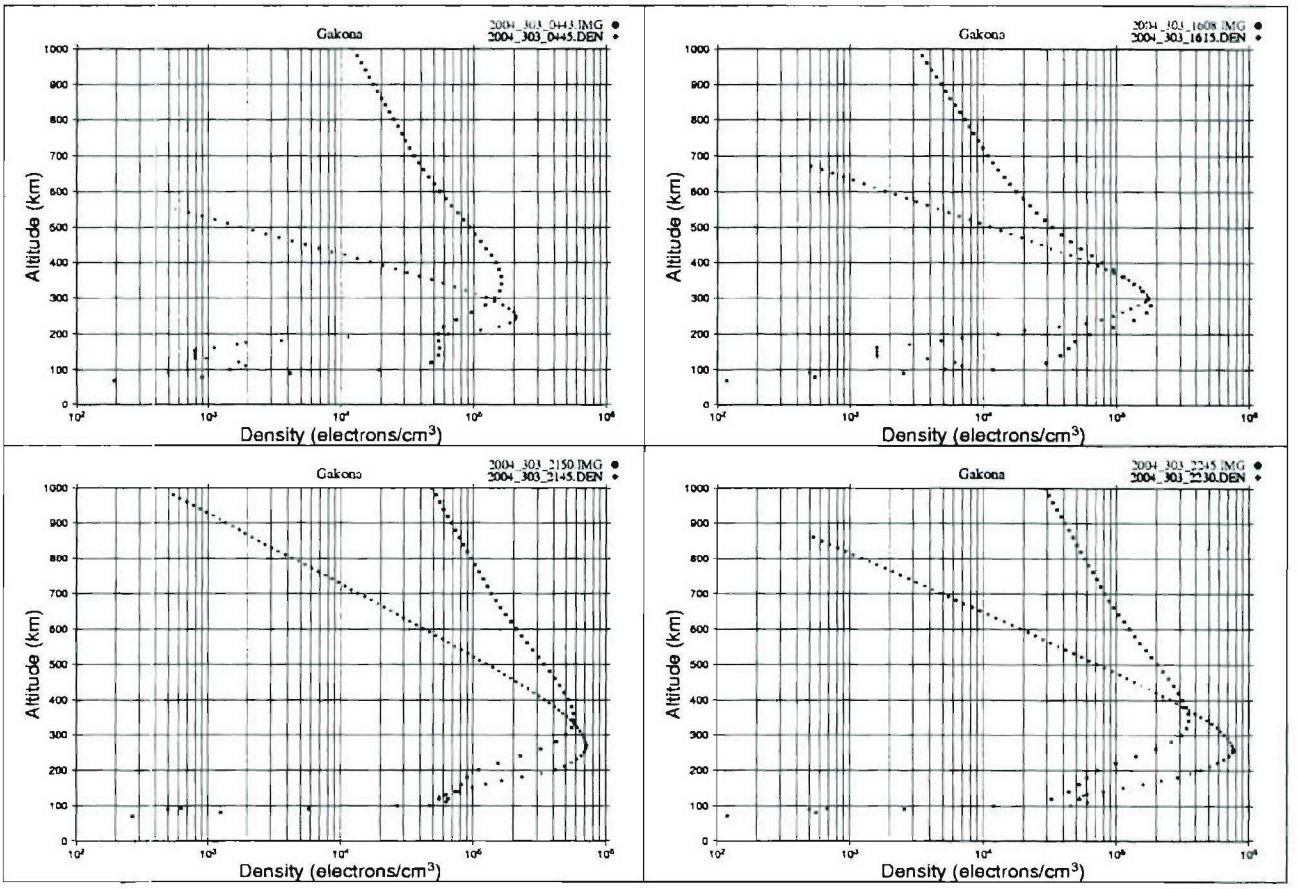


Figure 14. Density profiles for tomography (o) and Digisonde (+) for four time periods (04:43 UT, 16:08 UT, 21:50 UT, 22:45 UT) on 29 October 2004 (day 303).

Additional examinations were conducted for 1 November 2004 and 6 November 2004, based on a survey of days with quiet ionospheric conditions and reliable GPS calibrations (unaffected by ionospheric activity). The (local) afternoon of 1 November displayed the TEC discrepancy, but tomography cases were absent for this period, while 6 November displayed a general agreement between the Digisonde and GPS TEC results.

Very few quiet days, when both the digisonde and tomography densities would be considered reliable, were encountered during the winter period (December 2004 - January 2005). Investigations resumed after this period, with examination of several more days of DISS, GPS, and tomography results for TEC and density profiles. The daytime discrepancies between DISS and GPS or tomography TEC values remained, as well as discrepancies between the DISS and tomography density profiles. The days examined spanned the period from the end of January 2005 to mid-March 2005. The bottomside density profiles for DISS and tomography are often quite distinct for the daytime profiles (which were the predominant cases considered, because of the association with the TEC discrepancies), with different peak densities, altitudes for the peak densities, and bottomside scale heights. The topside density profiles are predominantly quite disparate, with the extrapolated DISS scale height determination being significantly smaller than the topside scale height for the tomography representation. (Figures 15).

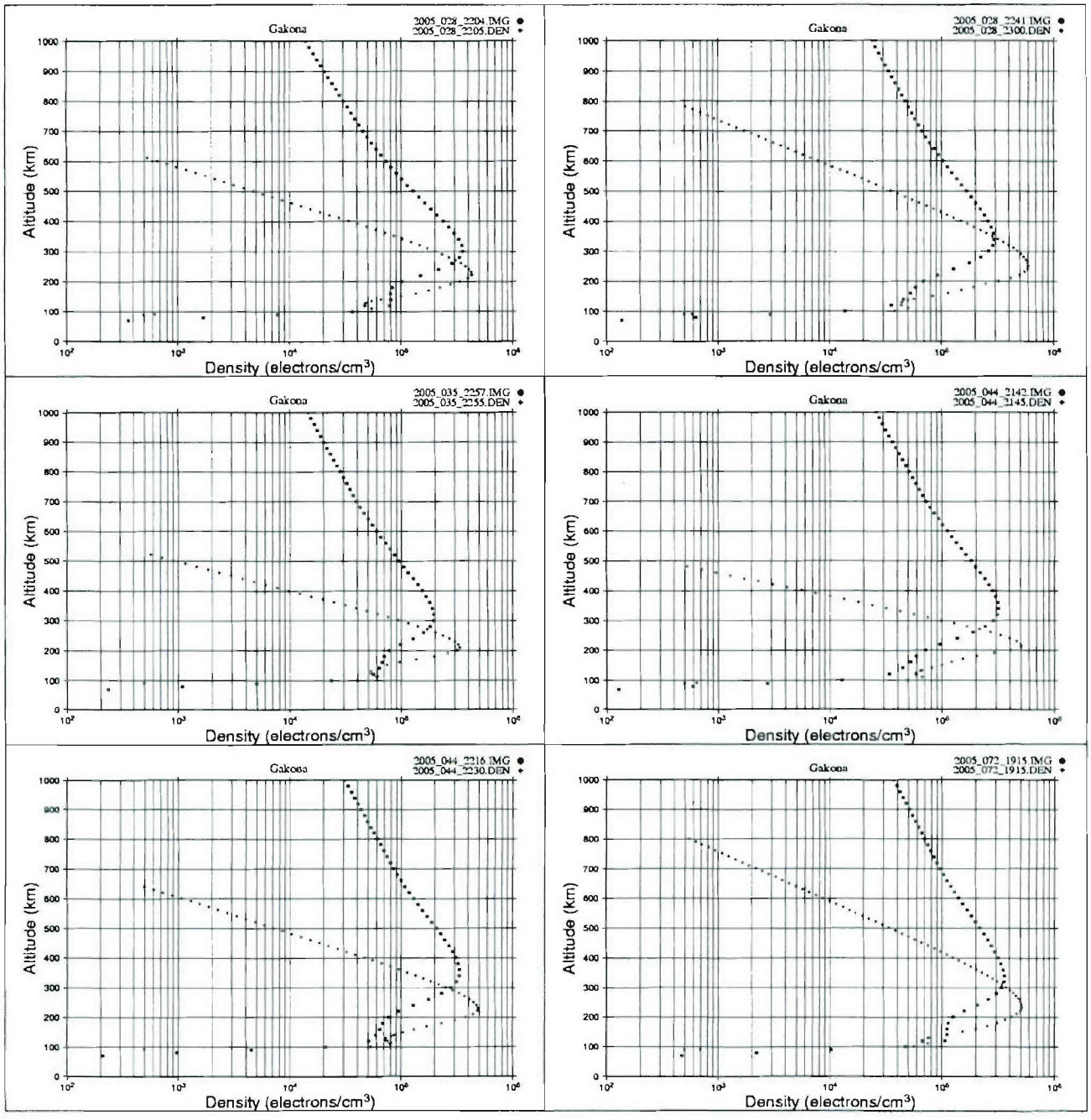


Figure 15. Density profiles for tomography (o) and Digisonde (+) for 22:04 UT and 23:00 UT on 28 January 2005 (day 28), 22:57 UT on 04 February 2005 (day 35), 21:42 UT and 22:16 UT on 13 February 2005 (day 44), and 19:15 UT on 13 March 2005 (day 72), with disparate topside density profiles arising from the extrapolated DISS scale height determination being significantly smaller than the topside scale height for the tomography representation. For the case on day 35, the DISS TEC is 4.1 TEC units, while the tomography TEC is 7.0 TEC units; for day 28 (23:00 UT), day 35, day 44, and day 72, the peak densities are also significantly discrepant.

Because the bottomside profile accounts for only about one-third of the contribution to the TEC, the topside scale height discrepancies appear to be the major contributor to the low DISS TEC estimates. The discrepancy in the bottomside profiles (Figure 16) or in peak densities (Figure 17) between the DISS and tomography sometimes counteracts the topside effect, even eliminating the TEC discrepancy between DISS and tomography in some cases (Figure 18). In some other cases, the peak densities and TEC values for DISS and tomography match, but the altitudes for the peak densities are considerably different. However, the density profiles in the vicinity of the peak density can have a close resemblance, producing the TEC agreement, even if the topside profiles diverge (Figure 19).

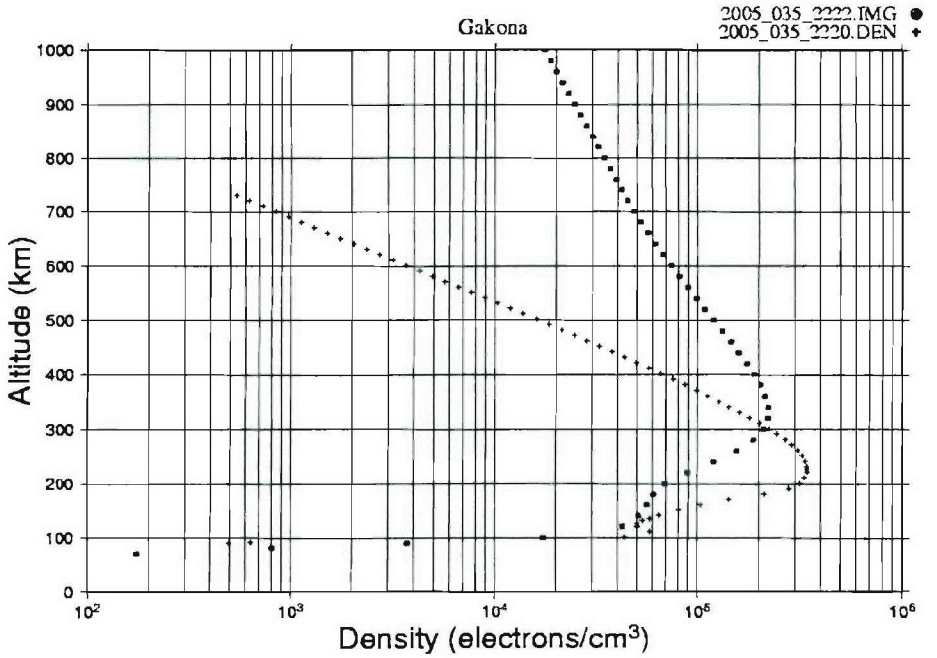


Figure 16. Density profile for tomography (o) and Digisonde (+) for 22:22 UT on 04 February 2005 (day 35), which display a closer TEC agreement (better than the typical factor of two discrepancy), even if the topside profiles diverge. The DISS TEC is 6.3 TEC units, while the tomography TEC is 8.0 TEC units, with the topside discrepancy partially compensated by the discrepancy in peak densities.

Some consideration has been given to reassessing the empirical orthogonal functions (EOFs) used for the tomography, based on the DISS bottomside profiles. This would be different from trying to utilize the DISS measurements in a real-time manner as inputs to the tomography process. The topside profile to be used for the EOFs could be determined from the peak density and TEC, using a topside scale height derived to produce a TEC value consistent with the GPS or ITS10S TEC calibrations. This endeavor would also require considerable effort to evaluate and possibly re-scale the DISS ionograms. However, it could ultimately reduce the tomography error magnitudes.

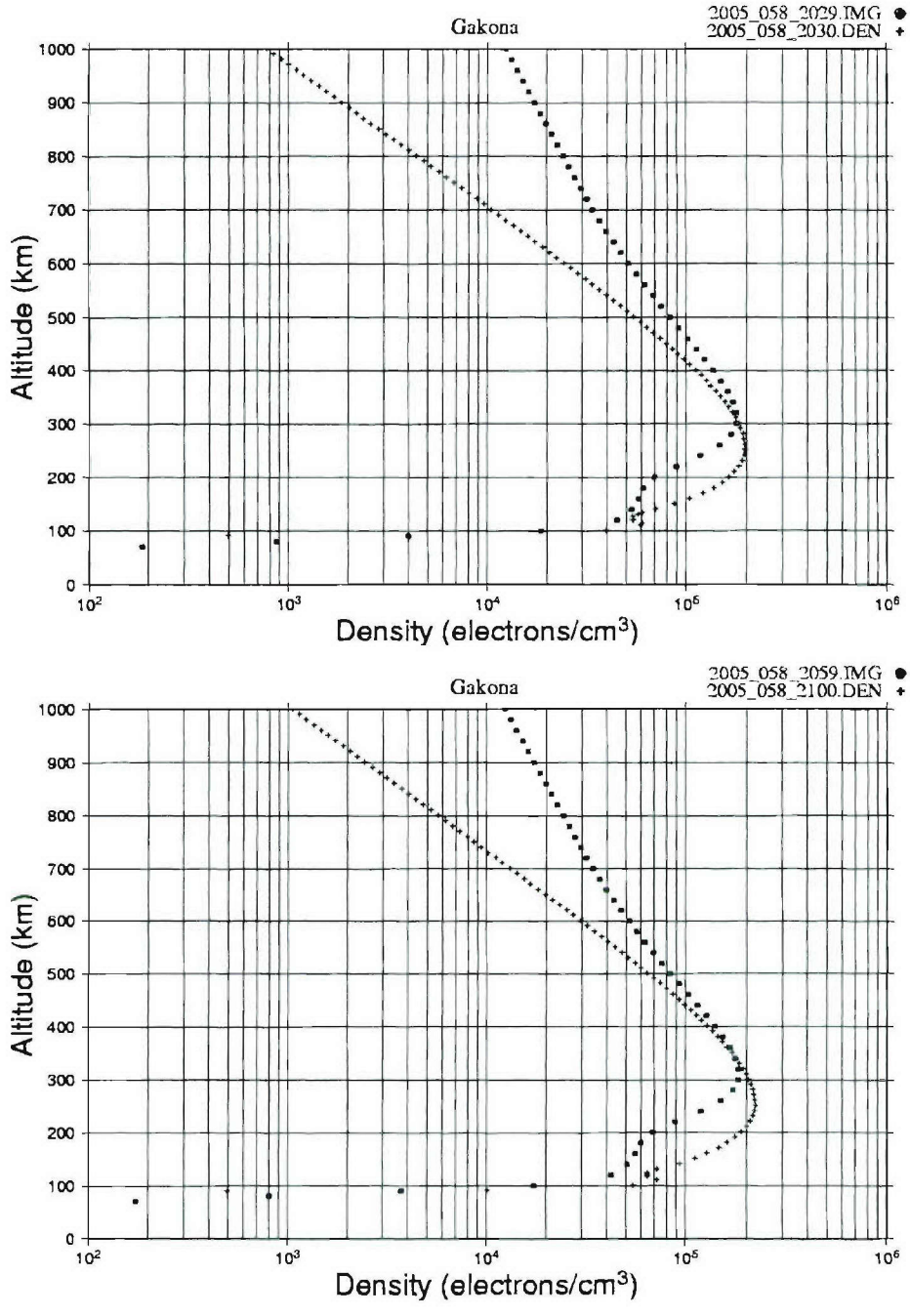


Figure 17. Density profiles for tomography (o) and Digisonde (+) for 20:29 UT and 20:59 UT on 27 February 2005 (day 58), exhibiting discrepancies in the bottomside profile and peak densities, respectively, despite the good TEC agreement between DISS and tomography, which are both different from GPS TEC.

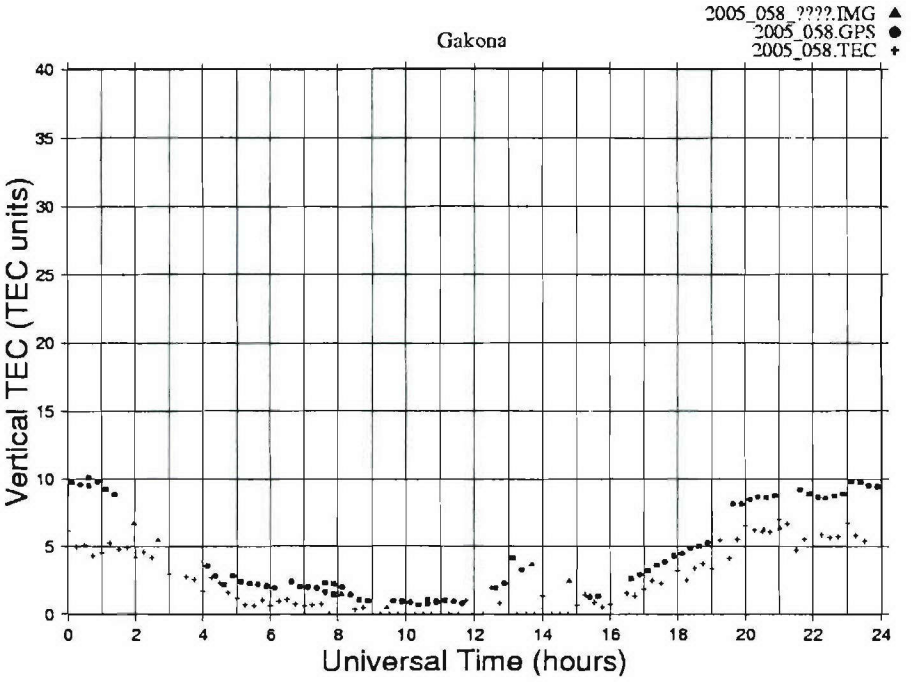


Figure 18. Vertical (or equivalent-vertical) TEC for tomography (Δ), GPS (o), and Digisonde (+) measurements for 27 February 2005 (day 58), indicating good TEC agreement between DISS and tomography TEC values at 20:29 UT and 20:59 UT, despite the discrepant density profiles. Note that a TEC discrepancy with GPS TEC remains.

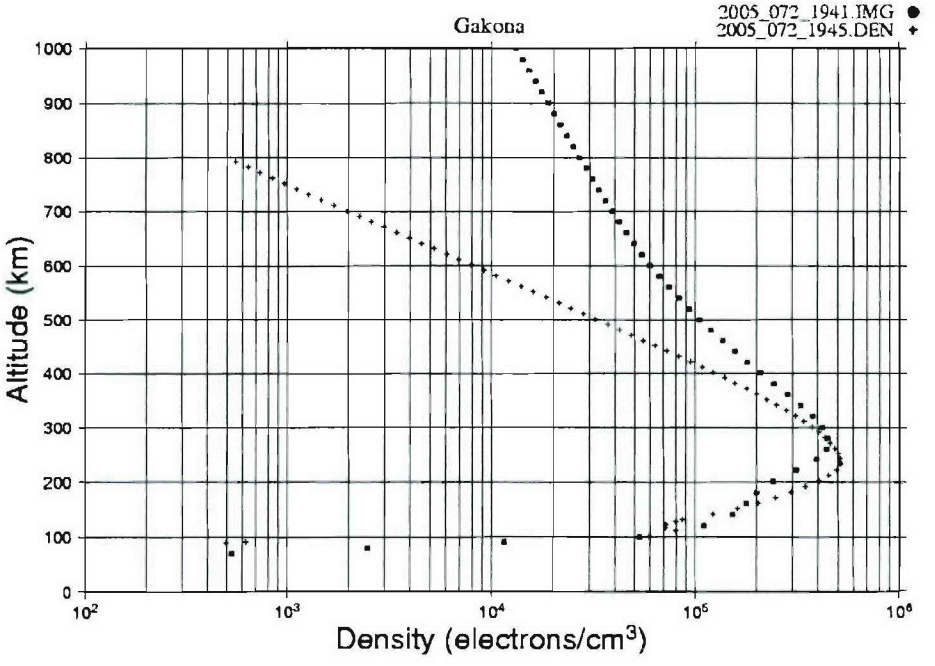


Figure 19. Density profile for tomography (o) and Digisonde (+) for 19:41 UT on 13 March 2005 (day 72), which displays a closer TEC agreement (better than the typical factor of two discrepancy), even if the topside profiles diverge. The DISS TEC is 10.1 TEC units, while the tomography TEC is 12.0 TEC units.

2.4 Observations of the Artificially-Perturbed Ionosphere

A field campaign was conducted at the HAARP facility in early February 2005 focusing on optical signatures of the heated ionosphere. Four satellite passes were identified for inclusion in this campaign to attempt to collect TEC observations of the ionosphere within the region heated by the HAARP transmitter. These passes were selected based on two criteria: time of day and number of receivers (of the set Cordova, Gakona, and Delta) for which the ray path Ionospheric Penetration Point (IPP) passes within the region most likely to be structured by the heater. The time criterion was constrained by several factors: the heater operations window, needs of the optics experimenters (who had priority for heater operation time), and a need to have enough ionization available in the main F region for the heater to work with. In order to obtain the maximum impact on F-region ionization, we planned to have the heater point directly up the field-aligned point in the F region and operate in CW O-mode at full power at a frequency just below f_oF2. In previous campaigns, we focused solely on observations from Gakona and from a receiver temporarily deployed in Copper Center. In this campaign, we included both Cordova and Delta to provide sampling of the heated region along ray paths not parallel to the local magnetic field within the heated region. A ray path was assumed to be within the heated region in the F region if the IPP passes within an area within eight degrees of angular distance of the center of the heated region as viewed from the heater.

Table 3. List of satellite passes from which data were collected during the optics campaign.

						RMS	Heater Start Time		
	Case	Rank	SAT	NSta	Date (UT)	GCA	UT	MST	AST
υ	7	18	o25	3	20050202	0.21	03:53:00	*08:53 PM*	*05:53 PM*
λ υ	9	1	o31	3	20050203	0.06	03:54:00	*08:54 PM*	*05:54 PM*
υ	16	7	o25	3	20050210	0.10	03:24:00	*08:24 PM*	*05:24 PM*
υ	18	11	o31	3	20050211	0.12	03:24:00	*08:24 PM*	*05:24 PM*
							Italic indicates time on previous day		

We were able to identify four passes, listed in Table 3, which occurred just after local F-region sunset with at least two stations meeting the "nearness" criterion. The pass marked with a λ symbol was among the top five ranked passes initially identified, and passes marked with a υ symbol occur during just after sunset in the E-region (100 km altitude). During the first two passes, ionization in the F layer dropped to below a level that the heater could interact with prior to the passes. This was unfortunate, as one of these passes (Case 9 in Table 3) had all three station's IPP tracks pass very near the heated region and the natural ionosphere was largely absent of the irregularities normally observed during non-sunlit times. The third pass was during a period of geomagnetic activity, and a combination of absorption and auroral-E made it impossible to get any heater energy to the F region.

For the fourth and final pass, which occurred on the final night of the campaign, the combination of a later sunset time and an earlier pass time provided enough F-region ionization for the heater to operate and geomagnetic conditions were quiet so that there was little or no absorption and no blocking auroral E layer. The heater operator attempted to keep the heater operating at just below f_oF2, and although it appears that at the time of the pass the heater was

operating above f_0F2 as measured by the Gakona digisonde, there is evidence from observations by the SuperDARN radar at Kodiak that the heater was generating irregularities in the F region over HAARP.

Preliminary analysis of the pass data from the three stations shows little evidence of heater modifications in the data collected at Cordova and Delta, but there is a possibility that a heater effect can be seen in the Gakona data. While it is difficult to sort out propagation enhancement of the effect of naturally occurring irregularities in the heated region when viewed from Gakona, which is why we collected data from the other stations, there is a compelling change in the characteristics of the small-scale irregularities observed in the Gakona data within the region most likely to have observable heater-generated irregularities.

A review of data collected by the Kodiak SuperDARN radar (Figure 20) shows that while natural irregularities started forming north of Gakona around the time of the pass and migrated southward over Gakona later in the evening, it appears that the heater was producing irregularities over Gakona at the time of the pass, perhaps with some "contamination" by natural irregularities. The tomography image generated from the Oscar 31 TEC data (Figure 21) shows a typical mid-latitude, daytime, ionosphere over and south of Gakona with lower densities and a more structured ionosphere from Delta northwards.

Our initial belief that the Gakona phase and intensity records from this pass show evidence of heater-produced irregularities came from inspection of the time-series records of detrended differential phase and VHF intensity from Gakona (Figure 22) and Delta (Figure 23). While the Delta record shows a classic, and smooth, enhancement of the phase structures at the point where the ray path is nearly field-aligned with little corresponding intensity scintillation, the Gakona record shows a very structured phase and intensity record at the field-aligned point, which for Gakona is also within the heated region. In particular, there is a large enhancement in both small-scale irregularities in both the phase and VHF intensity record.

Power-density spectra from the Gakona and Delta VHF records are shown in Figure 24. These spectra are for 1024 data points (just over 20 seconds in time). The two spectra from the Gakona record (the leftmost two panels in this figure) show data segments just prior to entry into the heated region and in the center of the heated region. The Delta spectrum is from near the center of the point in the pass nearest the geomagnetic meridian. The horizontal dotted lines on the spectrum plots indicate the nominal noise-floor as determined from the Gakona records away from the heated region. It is very clear from these spectra that as the ray path passes through the heated region at Gakona, there is an increase in the small-scale irregularities in both phase and VHF intensity. At Delta, there is no similar increase at the smaller scales as the ray path passes through the nearly field-aligned point. Our current working hypothesis is that the increase in power at small scales is a manifestation of the fine-structure "striations" which are postulated to form in the heated region (*Gurevich et al.*, 2002).

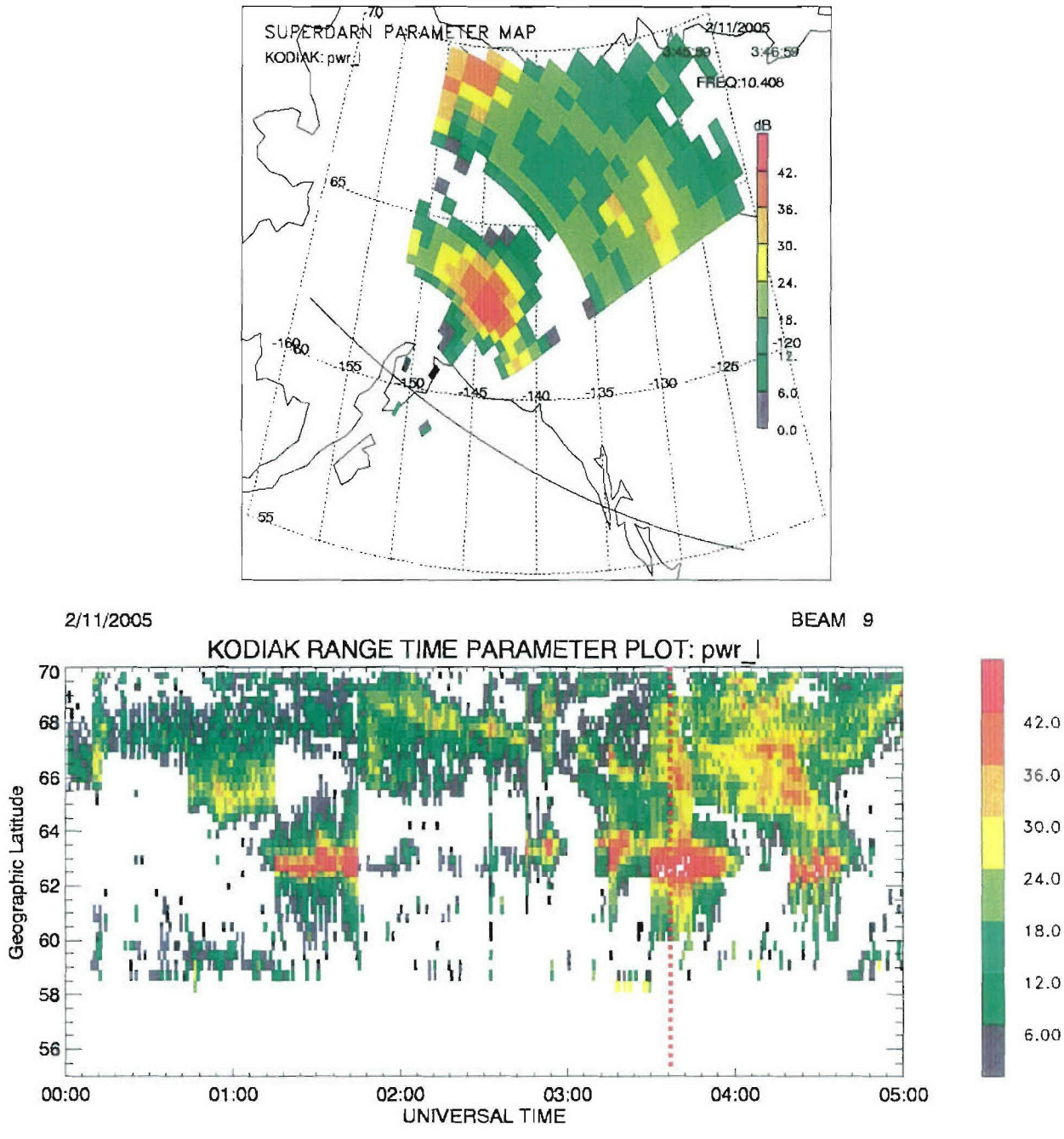


Figure 20. Data from the Kodiak SuperDARN radar (courtesy of R. Bristow of the University of Alaska at Fairbanks). The top panel shows the return power as a function of latitude and longitude at a time near the pass of interest, and the lower panel shows the return power as a function of latitude and Universal Time (UT). The vertical dotted line in the lower panel indicates the time of the pass of interest.

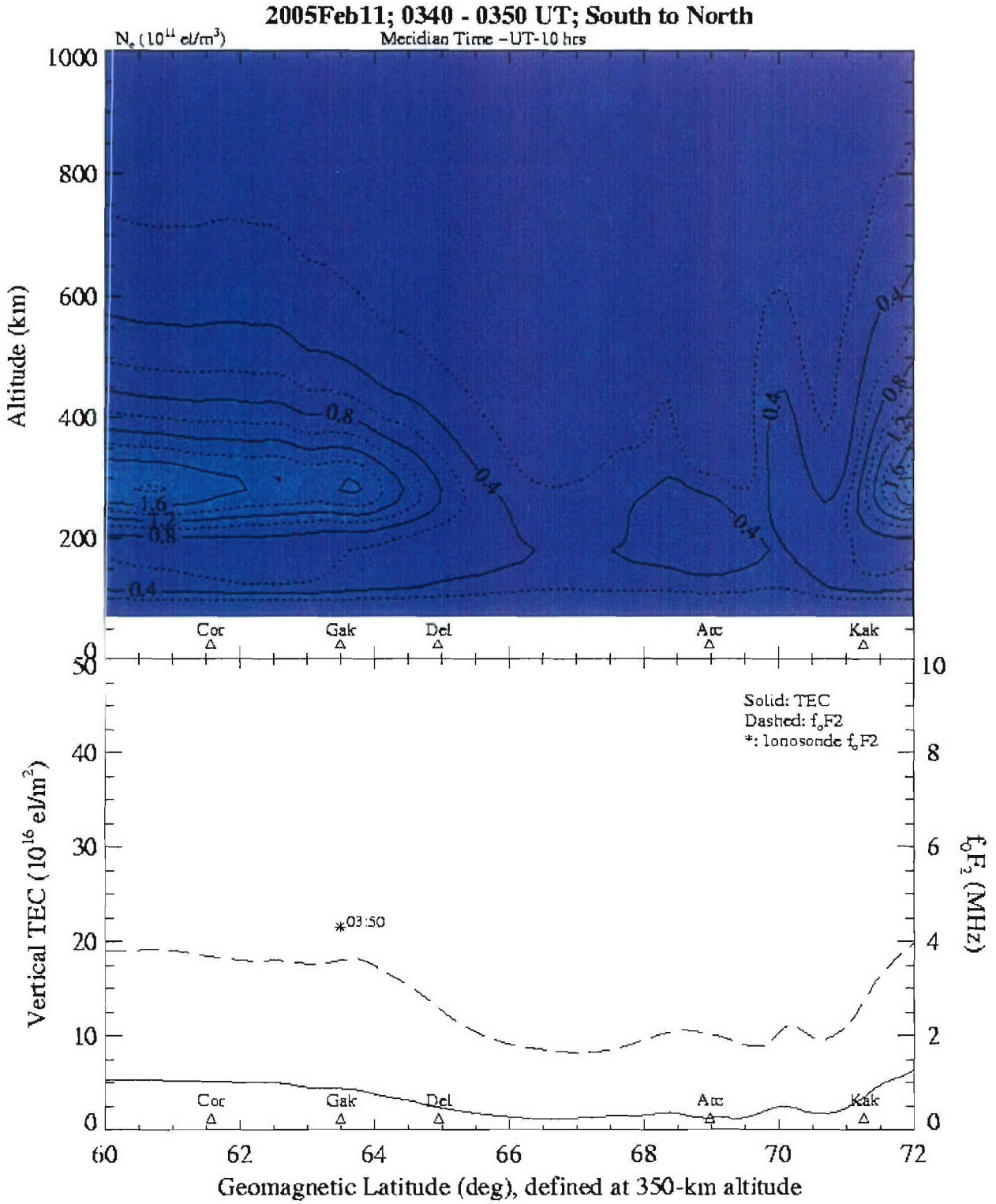


Figure 21. Electron density as a function of geomagnetic latitude and altitude derived from TEC data collected from the Oscar 31 pass using the NWRA tomographic processor (upper panel), and vertical TEC and f_oF2 as a function of geomagnetic latitude derived from the image in the upper panel (lower panel).

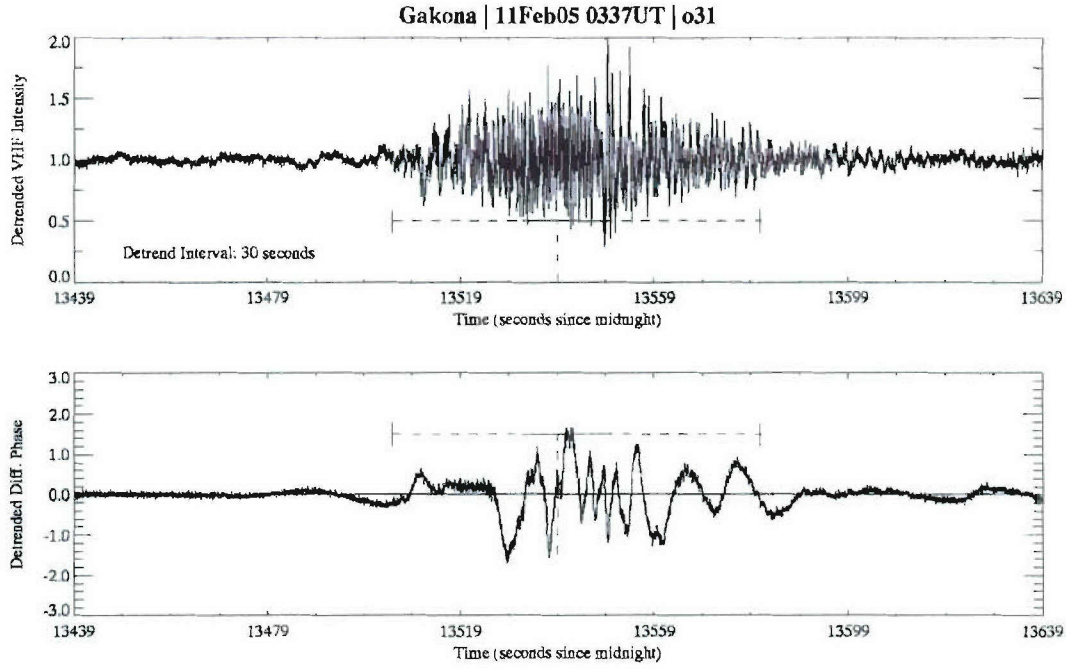


Figure 22. Detrended (30 second period) VHF intensity (upper plot) and differential phase (lower plot) from the Gakona ITS10S station for the 0337UT Oscar 31 pass on 11 February 2005. The horizontal dashed lines indicate the segment that is within 16 of the heater beam center and the horizontal solid line indicates the segment within 8 of beam-center. Closest approach to beam-center is indicated by the vertical dashed line.

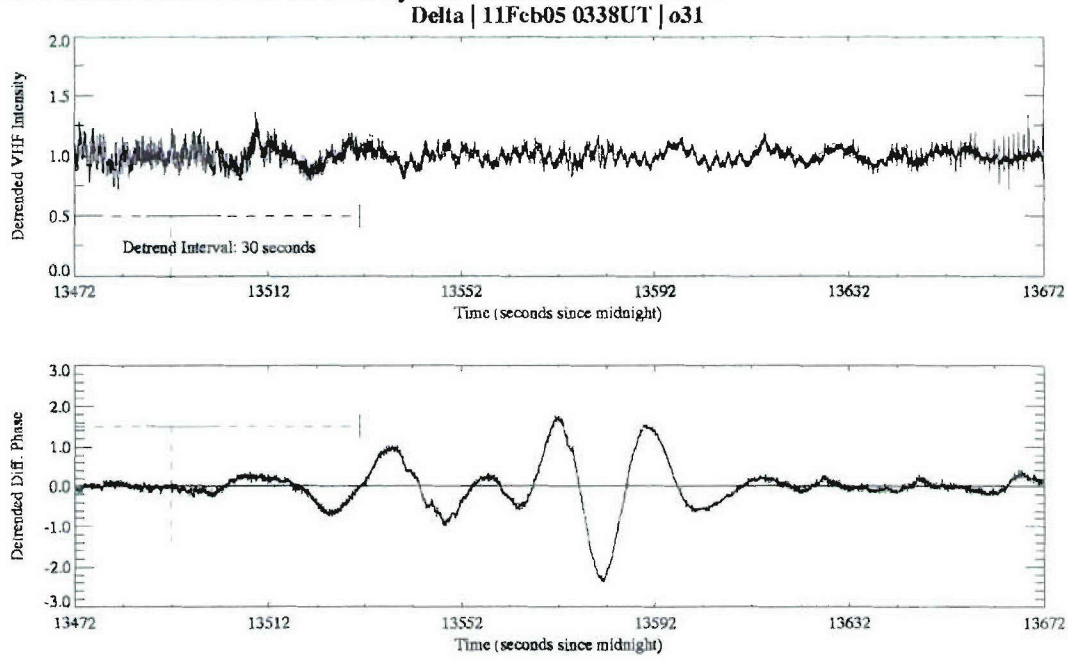


Figure 23. Detrended (30 second period) VHF intensity (upper plot) and differential phase (lower plot) from the Delta ITS10S station for the 0337UT Oscar 31 pass on 11 February 2005. The format of this figure is the same as Figure 22.

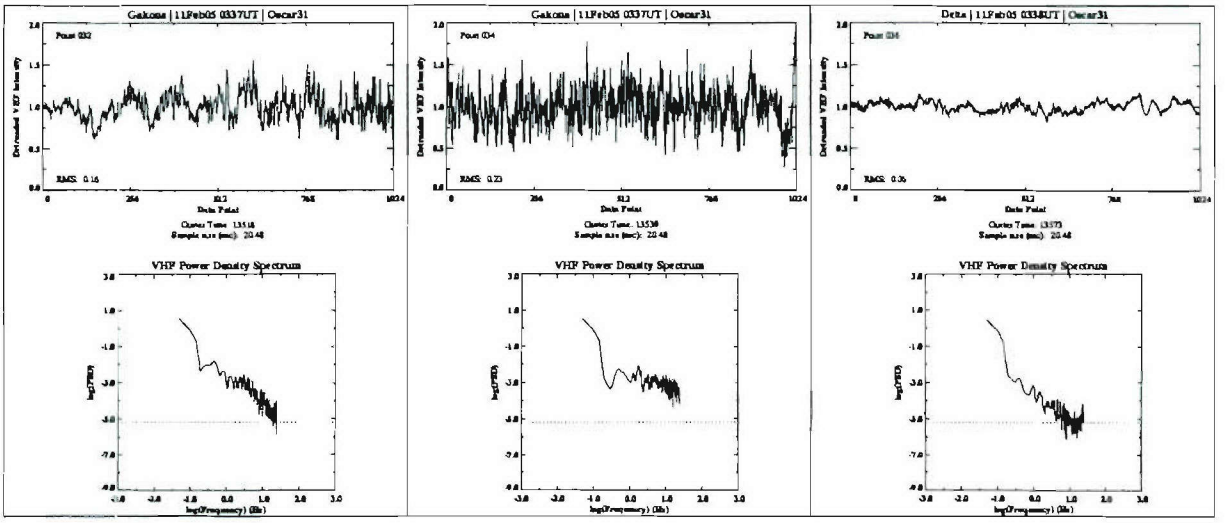


Figure 24. VHF intensity spectra from the ITS10S receivers at Gakona (first and second panels) and at Delta (third panel) from the Oscar 31 pass at 0337UT on 11 February 2005. In each panel, the upper plot is the time-series of detrended (30 second detrend period) VHF intensity and the lower plot is the power-density spectrum of the time series. The dotted line in the spectrum plots indicates the noise floor of the measurements.

3. Non-HAARP Topics

3.1 Ionospheric Scintillation Confidence Model

We have developed and implemented an initial model to provide a measure of the confidence in scintillation estimates calculated from the WBMOD ionospheric scintillation model (*Secan,* 2004). The confidence level is calculated as a multiplicative combination of the confidence level derived for the various factors listed in Table 4. Preliminary models, some of them fairly rudimentary, have been developed and implemented to account for reduction in confidence due to the system frequency, the user-selected percentile in the $\log(C_kL)$ distribution, K_p, SSN, target altitude, latitude regime, time of day, season, and elevation angle. This section will provide a brief description for each of these.

Table 4. Factors to be included in a WBMOD confidence-level model.

Parameter	Discussion
System Frequency	Two factors are in play here: the fact that scintillation drops rapidly with increasing radar frequency (increasing slightly the confidence at higher frequencies), and the fact that the data from which WBMOD was constructed is from a disparate set of frequencies, and not the same frequencies in each latitude regime. In a simple model for the latter factor, the confidence level would be higher in the VHF (137 MHz) through L-band (1200 MHz) range for which data were available with the same model for this variation used in all latitude regimes. In a more complex model, the confidence level would be changed based on what frequencies were available in the various latitude regimes.

Table 4. (continued)

Distribution Percentile	WBMOD does not model irregularity strength, but the distribution, or population, of irregularity strength given the necessary inputs. This allows the model to calculate irregularity strength (and from it, scintillation levels) either at a user-specified probability of occurrence (percentile) or the probability that a user-specified threshold is exceeded (threshold). Due to factors such as the natural reduction in the number of cases at either end of the distributions (very low or very high scintillation levels) and filtering effects due to the collection process (noise floors, saturation, equipment limitations, etc), there are typically few, and occasionally no, observations towards the ends of the distribution. Thus, the confidence in the output is less as the ends of the distribution are approached. For example, the 80^{th} percentile value is better sampled, and we have more confidence in it than we do in the 99^{th} or 1^{st} percentiles. The confidence level would be modified based on either the user-specified percentile or, in the case of a user-specified threshold, the percentile resulting from the scintillation calculation.
Elevation Angle	The propagation model used in WBMOD appears to start to break down as the satellite approaches the horizon. The data used in developing the model was limited to geometries where the satellite elevation angle was greater than 10 degrees for most of the data sets and higher for others. The confidence level in scintillation calculations will need to drop with elevation angle from about 10 degrees elevation to the horizon.
Satellite Altitude	The propagation model assumes that all scintillation effects are created within a thin phase-changing screen (phase screen) located within the ionosphere at an altitude calculated as a model parameter. Thus, a satellite just below this altitude will show zero scintillation while one just above this altitude will have the full scintillation level. In addition, WBMOD includes only F-layer irregularities, and there is evidence that there is scintillation caused by E-layer irregularities in the auroral zone. Both factors will be included in the confidence-level model.
IPP Latitude	This will likely be the most complex part of the final confidence-level model, and is most likely to be very simple in the initial implementation should the initial delivery be in the near future. In general, the confidence level is difference in the different latitude regimes: equatorial, anomaly crest, mid-latitude, auroral, polar cap. In addition to varying confidence levels within a particular region, there are also confidence levels to be attributed to uncertainties in the location of peaks and transition boundaries. Some of this can be derived from the WBMOD models for the transitions, but others will need to be constructed from scratch. Also, many of the transition boundaries are dependent on K_p, and so this part of the confidence-level model will have a certain amount of interdependence with that part concerned with K_p effects on confidence level.

Table 4. (continued)

Database Limits	The climatology within WBMOD is based on data collected at a discrete set of locations spread unevenly in latitude and longitude over the globe. The algorithms within WBMOD extrapolate and interpolate from the locations where observations were available to locations where they were not. While there is high confidence in some extrapolations (near total absence of equatorial scintillation during daylight hours), in others there is markedly less (extrapolation of the equatorial coupled seasonal-longitudinal variation to all longitude sectors). While this aspect is lumped in with "spatial location" parameters, it is likely to be a complex function of location and time.
IPP Local Time	The climatology within WBMOD is based on data collected at a discrete set of locations spread unevenly in latitude and longitude over the globe. The algorithms within WBMOD extrapolate and interpolate from the locations where observations were available to locations where they were not. While there is high confidence in some extrapolations (near total absence of equatorial scintillation during daylight hours), in others there is markedly less (extrapolation of the equatorial coupled seasonal-longitudinal variation to all longitude sectors). While this aspect is lumped in with "spatial location" parameters, it is likely to be a complex function of location and time.
Season/Longitude	This is also an issue for the equatorial region only. During those seasons when we know that it is unlikely that plume structures will form we can set the confidence levels high. When the likelihood of plume structures exceeds some threshold, the confidence levels would be reduced. In addition, recent investigations of WBMOD by AFRL/VSBXI have shown that the seasonal transitions are probably too sharp in the model. This should be reflected in the confidence model until such time as this issue is resolved.
SSN	The confidence in scintillation levels produced by WBMOD should drop at higher SSN simply because of the fewer cases of high SSN in the data used to generate WBMOD. This will be a slight effect, however, because there appears to be a natural "saturation" in the scintillation increase with SSN that sets in around SSN=150. This is in good agreement with the observation that the SSN variation of the critical frequency of the F2 layer, f_oF2, also appears to saturate at about SSN=150 or so.
K_p	The dependence of scintillation levels as calculated by WBMOD on K_p is very complex, and is very different in each of the latitude regimes. This section of the final confidence-level model may be as complex, if not more so, than the latitude-regime section. In general, and similar to the SSN situation, there are fewer observations at high K_p and thus the confidence level should be lower at higher K_p. In addition, there are considerations as to the accuracy of the input K_p (which can depend also

Table 4. (continued)

K_p (cont)	on whether it is an observation or a forecast), the source of the input K_p (calculated from magnetometer observations or derived from an auroral boundary location), and the time between the observation and the time of the product. The type of K_p will impact the confidence level in different latitude regimes in different ways. For example, while a K_p derived from an auroral boundary observation will provide a higher confidence in the location of the auroral scintillation boundary, it might provide a lower confidence in the scintillation levels in the post-midnight equatorial region. An initial implementation of the confidence-level model may well only address the issue of the low number of high K_p cases in the WBMOD database.
Drift Velocity	If phase scintillation parameters are used (S_4 is not impacted by this), uncertainties in the *in situ* drift velocity of the ionospheric irregularities will need to be reflected in the confidence levels. This will be dependent on the velocity of the target (and thus the target-motion component of the line-of-sight velocity through the irregularities), uncertainties in the drift-velocity models used, and, once again, on K_p. If only S_4 is to be used, this part of the confidence-level model can be deferred until such time as the phase parameters are to be used.

Note that this addition to WBMOD does not change the scintillation calculation in any way.

System Frequency

A number of factors contribute to reduce the confidence level as a function of the system frequency: the frequency range of data used in building the WBMOD climatology, the line-of-sight propagation assumption implicit in the WBMOD propagation model, and phenomena not included in WBMOD such as E-layer irregularities and scintillation caused by tropospheric effects. The model implemented sets the confidence level for this factor to 10% for frequencies below 100 MHz, 100% for frequencies between 130 MHz and 1600 MHz, 80% for frequencies greater than 5000 MHz, with linear interpolation used to fill in between 100 and 130 MHz and 1600 and 5000 MHz.

Percentile

WBMOD models the probability distribution function (PDF) of $\log(C_kL)$ which allows a user to either (1) specify a threshold scintillation level and have the model calculate the probability of that level being exceeded, or (2) specify a percentile and have the model calculate the scintillation levels for that percentile. In either case, the model will be calculating scintillation levels from various points in the $\log(C_kL)$ PDF. Due primarily to data limitations such as noise floors and S_4 saturation, the extremes of the $\log(C_kL)$ PDF are not well-represented in the modeling process. This leads to a reduction in confidence at both the low and high ranges of the PDF. The model sets the confidence level to 5% at the ends of the PDF (0.0 and 1.0), to 100% in the range 0.1 to 0.9, and linearly interpolates between the ranges 0.0 to 0.1 and 0.9 to 1.0.

Geomagnetic Activity Index (K_p)

Reduction in confidence derived from the K_p value input shows up both explicitly via a function directly related to the K_p level and implicitly in the high-latitude regime as described later. The explicit function is designed to mirror reduced confidence in the K_p variations in the model at very low and very high K_p values due to the natural reduction in the number of very low and very high K_p observations. In short, the statistics for very low and very high K_p conditions are worse than for other K_p conditions because fewer cases are available for inclusion in the modeling process. The confidence level factor for K_p is set to 80% at K_p of 0o, linearly increases to 100% at 1-, stays at 100% to 6o, and then linearly decreases to 10% at 9o.

Sunspot Number (SSN)

Similar to K_p, observations at very high SSN are underrepresented in the WBMOD modeling database with similar effects on the confidence. To reflect this, the confidence level factor for SSN is set to 100% up to 175, linearly decreases to 60% at 250, and set to 60% for SSN>250.

Target Altitude

In the standard WBMOD, if the target is below the ionospheric irregularities which cause scintillation, no further calculation is done. The propagation code in WBMOD assumes that the irregularity layer, which can extend hundreds of kilometers in altitude, can be assumed to be in a single, thin, phase-changing layer known as the phase screen, which is located at a certain altitude within the ionosphere. If the target is below the phase-screen altitude, WBMOD assumes there will be no scintillation. The *wbmod-v15-rs* program handles the calculation in the same manner, and the confidence level factor based on target altitude is calculated based on the following algorithm:

1. If the target is entirely above the irregularity layer, defined as above 800 km, the confidence level factor is set to 100%.

2. If the target is within the F-region irregularity layer (< 800 km) and above the phase-screen altitude, the confidence level factor is reduced smoothly from 100% at 800km to 10% at the phase-screen altitude (nominally 350 km).

3. If the target is below the phase-screen altitude but within the F-region irregularity layer (> 200 km) OR above an auroral-E irregularity layer (assumed to be at 90 km), the confidence level factor is increased smoothly from 10% at the phase-screen altitude to 100% at 200 km if no auroral-E layer is present or at 90 km if one is present.

4. If the target is below any ionospheric irregularities, the confidence level factor is set to 100%.

Note that the setting on this parameter does not affect the scintillation parameters calculated. As in the standard WBMOD, if the target is below the phase-screen altitude, no scintillation parameters are calculated. Figure 25 shows an example of how this factor will vary with altitude. The dotted line indicates how the region between 90 km and the phase screen varies when the target is determined to be within the auroral E-region.

The determination of whether the raypath intersects a region where there might be an auroral E layer is based on two models. The equatorial and poleward latitude boundaries of a possible

auroral E layer are calculated using the implementation of the DMSP SSJ4 boundary model (driven by K_p) used in WBMOD for the equatorward boundary (see references *Secan* [2004]) and a simple model for the poleward boundary that locates it $4+K_p$ degrees poleward of the equatorial boundary (see page 44 in *Miller and Gibbs* [1978]).

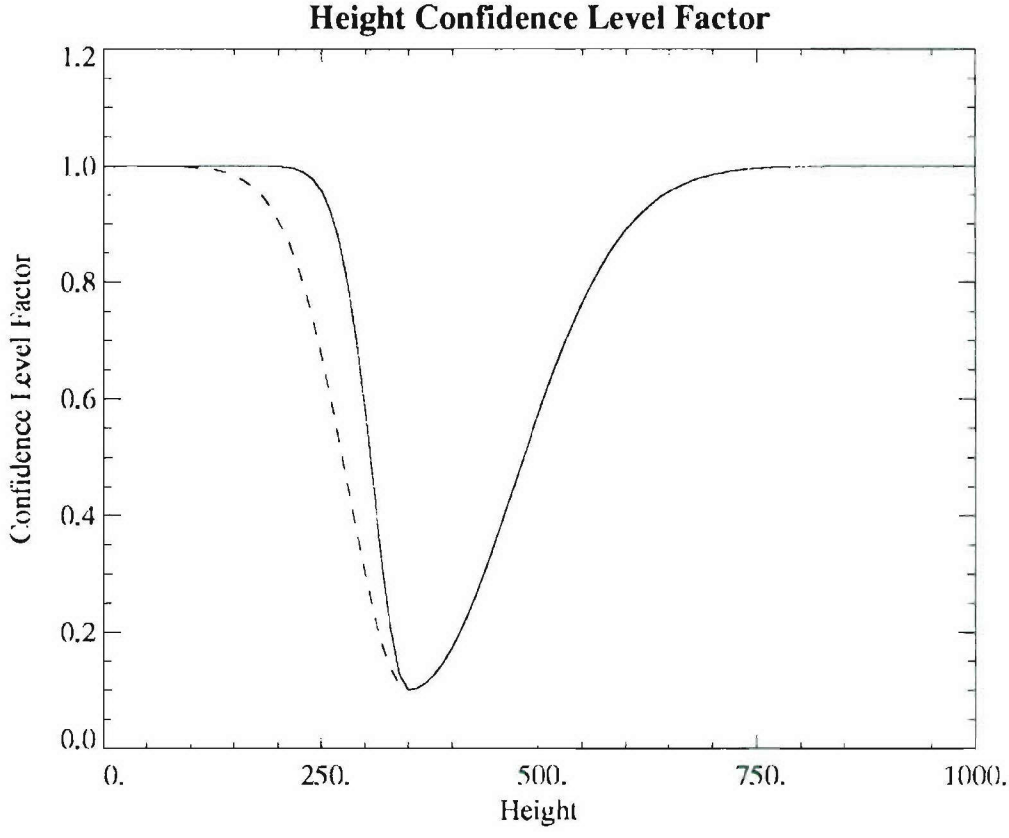


Figure 25. Example of the height variation of the height confidence-level factor.

Latitude Region

The latitude region section of the confidence level model is divided into three sections: equatorial, extending from the geomagnetic equator to the poleward edges of the anomaly crest regions; high latitude, extending from the geomagnetic poles to the equatorward edges of the sub-auroral region; and mid-latitude, covering everything else. The confidence level factor for the latitude regime is set to 100% in the mid-latitude regions, with fairly complex models based on the WBMOD C_kL model in the other two regions. Note that the equatorial region as implemented includes local time and season factors, but these are described separately in later sections of this document. This section will focus solely on latitude-based variations. In both the equatorial and high-latitude regions, reduction in the confidence level is based on uncertainty in the location of peaks and transition latitudes.

In the equatorial region, the confidence level factor is calculated based on the uncertainty in the location of the anomaly crests. This is modeled by two Gaussian-shaped reductions in the confidence level of 20% centered on 3° north and south of the center latitude of the anomaly crest as set in the $\log(C_kL)$ model with 2° half-widths. This is further modulated by the time and season factors described in the next two sections.

In the high-latitude region, there are three transition latitudes: two involving the transition from mid-latitudes into the sub-auroral and auroral latitude regions, and one involving the transition form auroral into polar cap. The first two are included in the confidence level factor as 20% Gaussian-shaped reductions centered on the transition latitudes from the $\log(C_kL)$ model using transition widths also from that model. The auroral-to-polar-cap transition uses an error function to transition from the auroral value to an additional polar-cap decrease of 20%.

Time of Day

In the equatorial region, there are two transitions which alter the confidence level: sunset, when scintillation levels can increase dramatically over periods as short as a few minutes; and sunrise, when solar-produced ionization begins to fill in the plasma-density irregularities generated during the night. Uncertainty in the time of the sunrise onset is reflected by a decrease of 20% in the confidence level factor at the time of sunset dropping rapidly away from that time via a Gaussian function with a 30-minute half-width. Sunset is specified by the time-past-sunset metric used in the $\log(C_kL)$ model (t_{PSS}). At sunrise, the confidence level factor for all variables is forced to 100% using an error function with a 30-minute half-width. Between the end of the sunrise and sunset transitions, the confidence level for the entire equatorial region is forced to 100% to reflect the very low probability of daytime scintillation.

There are no explicit time-of-day variations in the confidence factor in the other latitude regions.

Season

Recent ad hoc studies of the equatorial section of WBMOD have shown that there may be problems with the seasonal variation. To reflect this, a confidence level factor has been included that uses the same metric as the $\log(C_kL)$ model: the angle between the local geomagnetic meridian and the sunset terminator (Φ_{trm}). In the $\log(C_kL)$ model, the probability of the production and growth of the post-sunset bubble structures that are the cause of severe equatorial scintillation is highest when Φ_{trm} is zero. The recent studies indicate that this model may be introducing unrealistically-sharp longitude transitions in maps of scintillation parameters derived from WBMOD. To reflect this uncertainty, the confidence level factor for the equatorial seasonal variation is reduced by 25% using two Gaussian functions in Φ_{trm} centered on dates when the rate-of-change in the seasonal function used in the $\log(C_kL)$ model are maximum (dates when $\Phi_{trm} = \pm W_c/\sqrt{2}$, where W_c is the half-width from the $\log(C_kL)$ model) using a half-width of $W_c/4$. Figure 26 shows the seasonal variation for a satellite viewed at near overhead at Ancon, Peru.

An additional term, fixed in longitude, is included as part of the seasonal variation. During the model development, it was noted that there were differences in the seasonal behavior transitions in different longitude sectors. The longitude distribution of the data used in model development was inadequate to accurately note where the transitions occurred from one behavior to the other, so two longitudes were selected to transition between the observed behaviors at arbitrary points between the sectors where data were available (at 60° and 210° east longitude). To indicate the uncertainty in the location, and characteristics, of these two transitions, the confidence level is dropped by 20% at these longitudes (in the equatorial region only) via two Gaussian functions with half-widths as used in the $\log(C_kL)$ model.

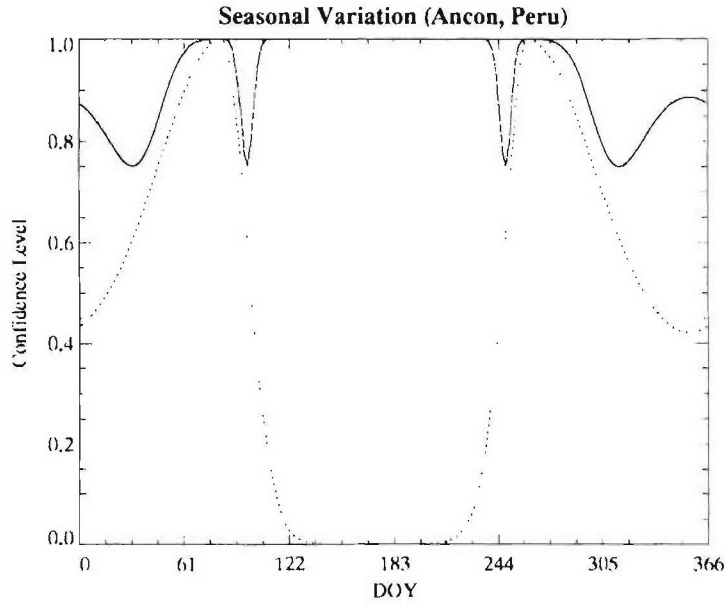


Figure 26. Example of the seasonal variation at Ancon, Peru.

There are no explicit time-of-day variations in the confidence factor in the other latitude regions.

Elevation Angle

The final confidence level factor in the current implementation accounts for increased uncertainty in the WBMOD propagation model at low elevation angles. The confidence level factor remains at 100% until roughly 10° elevation. At this point, the factor is rapidly reduced to roughly 1% at the horizon using an error function of the elevation angle. Figure 27 shows this transition.

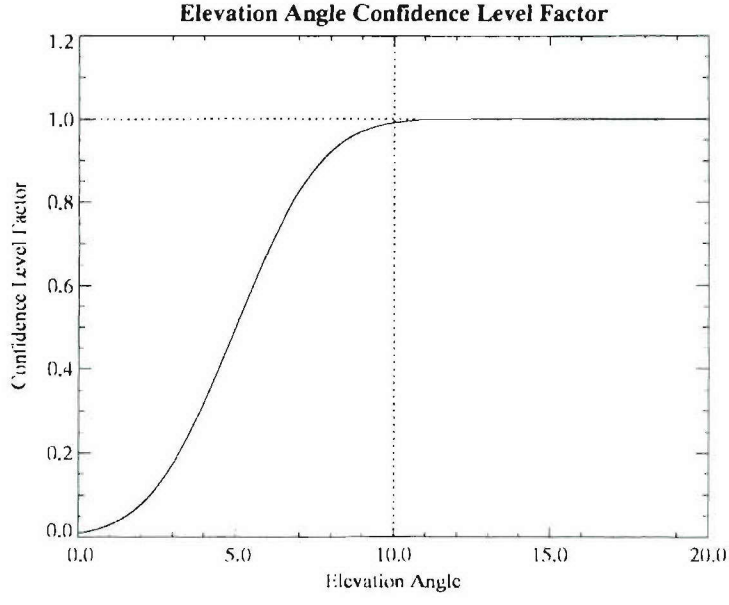


Figure 27. Example of the elevation-angle confidence level factor.

Final Confidence Level Calculation

The first step in generating the final confidence level is to combine the local-time and season factors with the equatorial region factor to produce a final latitude region factor. Once this is done, the remaining six confidence-level factors described above are merged by multiplying them together. This final combined factor is then applied to a maximum confidence level (set to 95%) and constrained to be greater than a minimum level (1%). Figures 28 and 29 are geographic latitude slices from south to north pole of the confidence factor along the 100° longitude meridian for local noon and midnight, respectively. The latitude transition features can be clearly seen in these figures, as well as the relative confidence in the various regions.

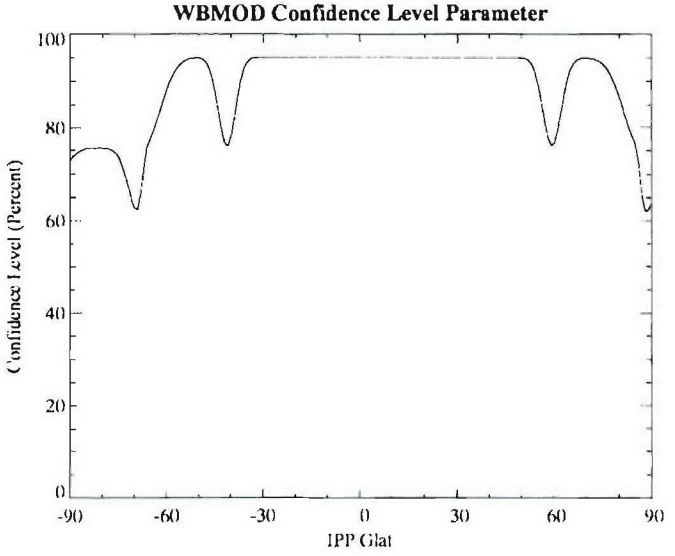


Figure 28. Variation of the confidence level as a function of geographic latitude along the 100° longitude meridian for local noon.

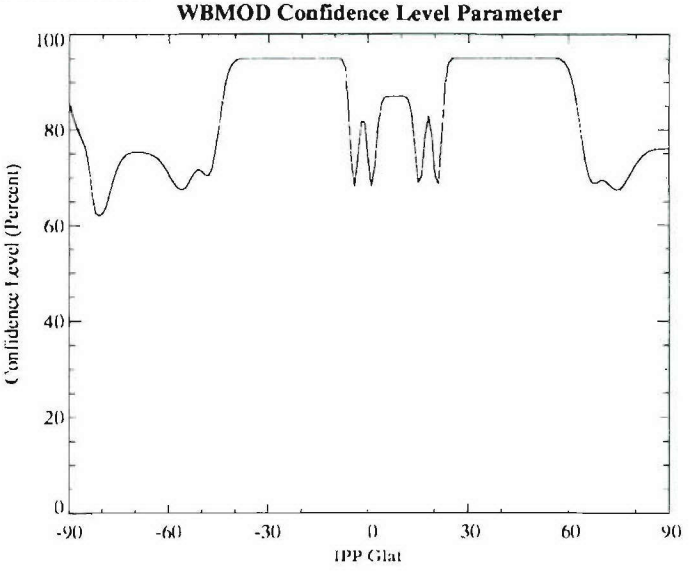


Figure 29. Variation of the confidence level as a function of geographic latitude along the 100° longitude meridian for local midnight.

Figure 30 is a slice along a constant geomagnetic latitude of (top to bottom) 14°N, 7°N, 0°, 7°S, and 14°S at 1700 GMT as a function of geomagnetic longitude. In each of these plots, the solid curve is the total confidence factor, the dotted curve is a combination of the seasonal and longitudinal contribution to the total, and the dashed curve is from the t_{PSS} contribution. The sharp decrease in confidence at sunset is clearly shown (the vertical dashed line indicates the point where $t_{PSS} = 0$) as is the sunrise transition to the maximum confidence level of 95%. Much of the structure during the night is due to the seasonal factor, which varies as a function of longitude, and the two longitude terms described earlier (the two vertical dotted lines indicate the location of these two transition longitudes).

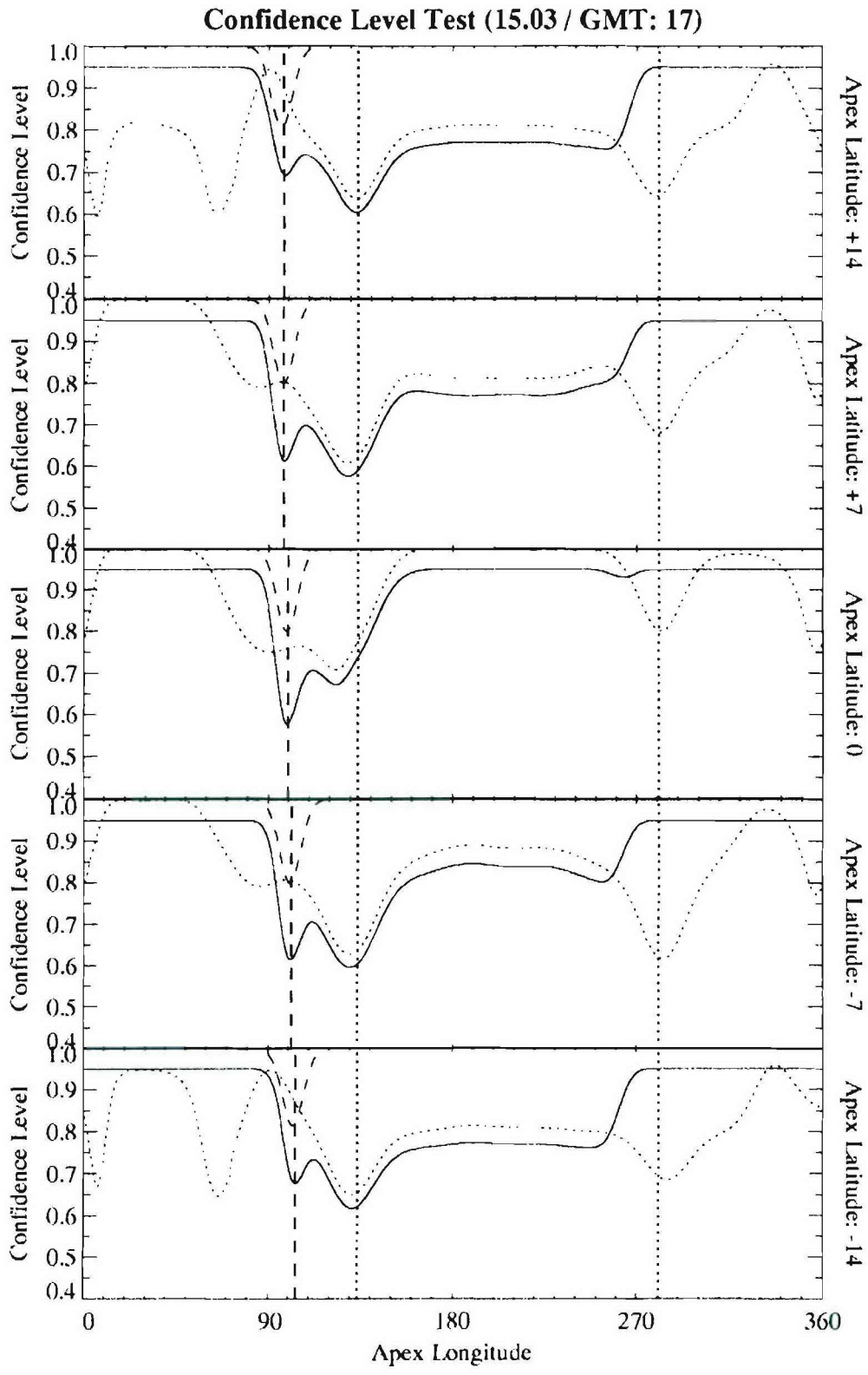


Figure 30. Variation of the confidence level as a function of geomagnetic latitude at various geomagnetic latitudes for 1700 GMT. See text for details.

4. Publications and Presentations

E. J. Fremouw, J. A. Secan, G. J. Bishop, Ionospheric Trough Behavior in Alaska, presented at the *International Beacon Satellite Symposium* held during 18 – 22 October 2004 in Trieste, Italy.

S. P. Kuo, Paul Kossey, James T. Huynh, and Steven S. Kuo, Chaotic Scattering of Trapped Relativistic Electrons in the Magnetosphere by Whistler Waves, *31st IEEE International Conference On Plasma Science,* June 28-July 1, 2004, Baltimore, Maryland.

S. P. Kuo, Paul Kossey, Steven S. Kuo, James T. Huynh, Amplification of Whistler Waves by Trapped Relativistic Electrons in the Magnetosphere, *31st IEEE International Conference On Plasma Science,* June 28-July 1, 2004, Baltimore, Maryland.

S. P. Kuo and M. C. Lee, Cascade spectrum of HFPLs generated in HF heating experiments, submitted to the *J. Geophys. Res.*

J. A. Secan, E. J. Fremouw, G. J. Bishop, Ionospheric Trough Behavior in Alaska, presented at the *Ionospheric Effects Symposium 2005* held during 3 – 5 May 2005 in Alexandria, VA.

Appendix A. Data Displays from the HAARP Web Site

This appendix provides samples of the data displays that can be found on the HAARP Web site generated from instruments operated for HAARP by NWRA. As described in the body of this report, these displays are generated either at the HAARP site or at NWRA's Bellevue office and shipped to the HAARP computers for display. The primary URL for access to the latest data of each display type is given below. These displays are available for the entire period that NWRA has been collecting data for HAARP. All of these displays can be accessed, although not all directly, from the main HAARP data page at URL:

http://www.haarp.alaska.edu/haarp/data.fcgi

The displays are grouped by data source as follows:

LEO Data Sets:

Figure A1: Standard plot of data from one LEO pass as collected from a single station. The URL for the latest pass from a given station is:

*http://maestro.haarp.alaska.edu/cgi-bin/its10/plot-tec.cgi?location=**station***

where ***station*** is replaced by the name of the receiver site (*cordova*, *gakona*, *delta*, or *arctic_village*). Note that these displays are available only for the NWRA ITS10S receivers.

Figure A2: Tomographic image generated from analysis of a single LEO pass collected at stations in the HAARP tomography chain (see Figure 1). The URL for the latest image is:

http://maestro.haarp.alaska.edu/cgi-bin/its10/plot-tom.cgi?archive

GPS Data Sets:

Figure A3: Standard plot of data from one GPS pass as collected at Gakona from the Ashtech Z-FX system. The URL for the latest pass from a given station is:

*http://maestro.haarp.alaska.edu/cgi-bin/ashtech/plot-ash.cgi?**yyyyddd.prn***

where ***yyyyddd.prn*** is replaced by year (***yyyy***), day of year (***ddd***), and GPS satellite PRN number (**prn**). While these can be accessed directly, the usual access will be through links on the next figure.

Figure A4: Daily individual pass summary plot of all GPS TEC data collected during a particular day. The URL for this is:

*http://maestro.haarp.alaska.edu/cgi-bin/ashtech/tec.cgi?date=**yyyymmdd**&type=sa*

where ***yyyymmdd*** is replaced by year (***yyyy***), month (***mm***), and day of month (***dd***). The plot for an individual pass, as shown in Figure A3, can be accessed from this page by clicking on the pass's TEC trace.

Figure A5: Combined summary plot of all GPS TEC data collected during a 36-hour period. The URL for the most recent data is:

http://maestro.haarp.alaska.edu/cgi-bin/ashtech/tec.cgi

By using links on this page, you can access the seven- and twenty-eight-day plots shown in Figures A6 and A7. By clicking on individual days on these multi-day plots, you can obtain the single-day plot for the selected day in the format of Figure A5.

Figure A8: GPS position error derived from GPS positions provided by a single-frequency receiver (a CNS GPS clock used for timekeeping). The URL for the most recent data is:

http://maestro.haarp.alaska.edu/cgi-bin/ashtech/tec.cgi?type=sgps

This plot shows 36 hours of data. A similar plot for a single hour of data can be accessed by clicking in the upper panel of this figure.

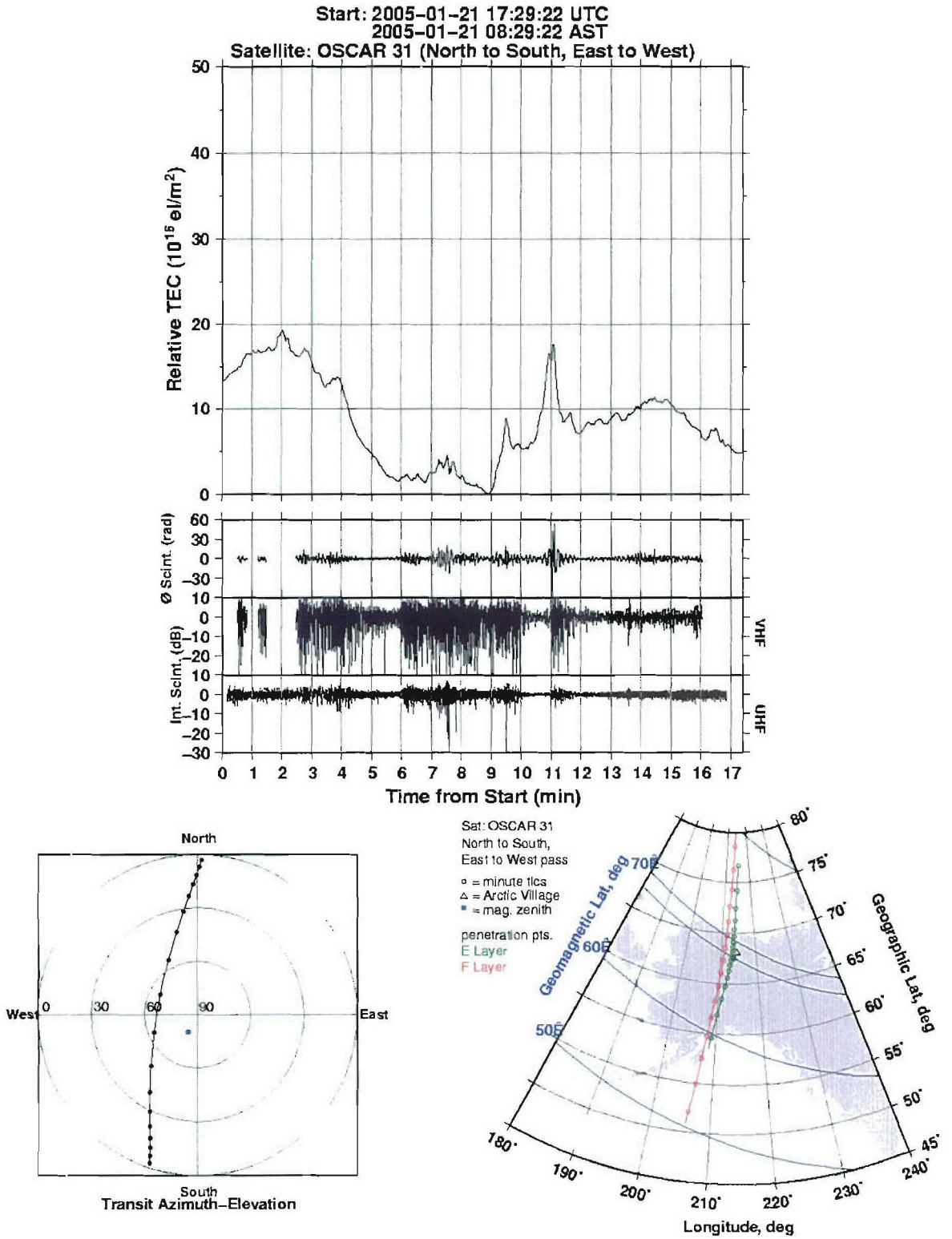


Figure A1. Example of LEO satellite data collected from the ITS10S receiver located at the new Arctic Village site. The upper panel shows the relative slant TEC, phase scintillation, and intensity scintillation for the pass; the lower-left panel shows the elevation and azimuth angle geometry of the pass; and the lower-right panel shows the pass geometry on a map of Alaska.

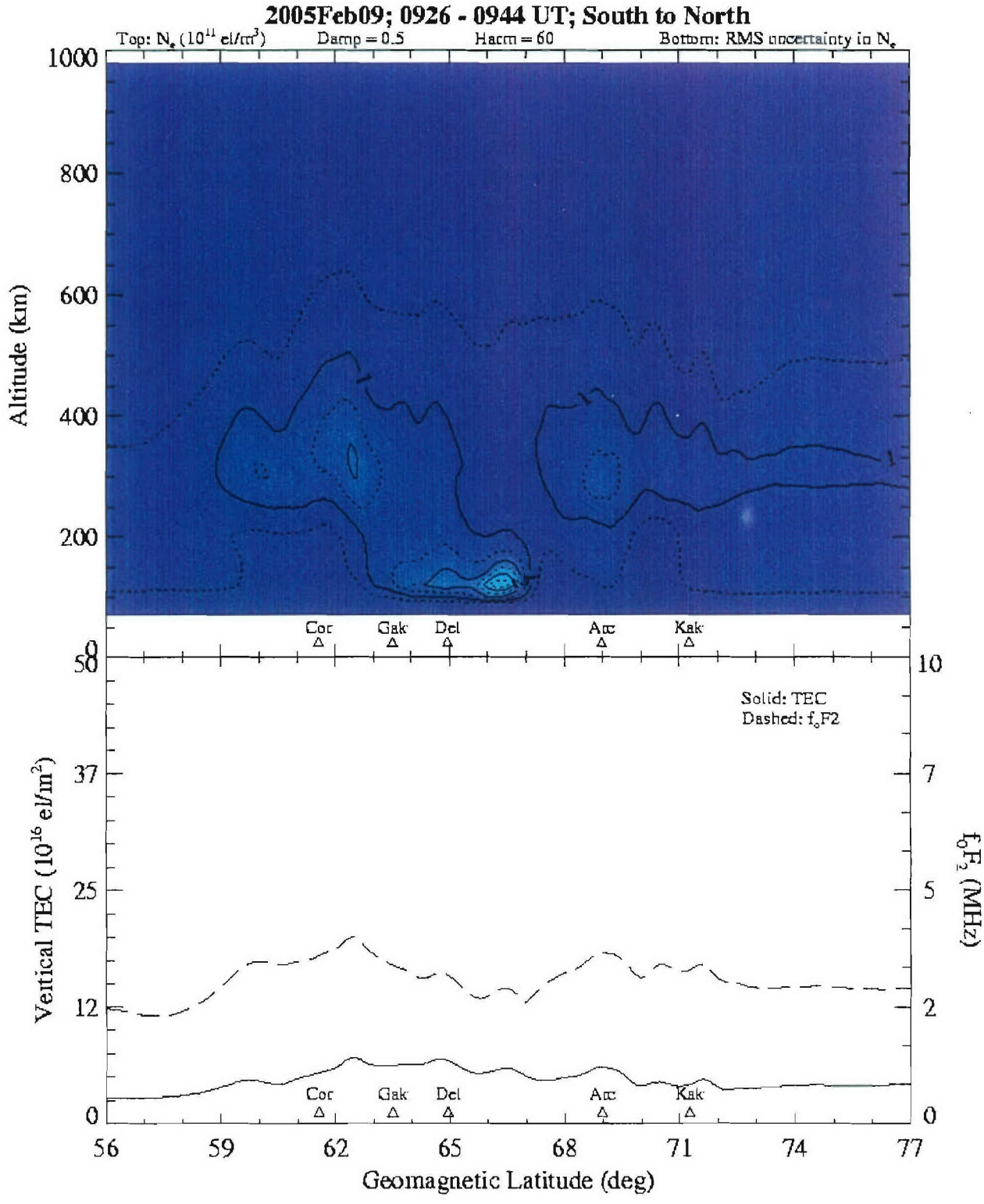


Figure A2. Sample image generated from the NWRA tomographic processor. The upper panel is a contour plot of electron density, and the lower plot show vertical TEC (solid curve) and f_0F2 (dashed curve) derived from the image. The locations of receiver locations that contributed data to the image are shown as triangles along the bottom of both plots.

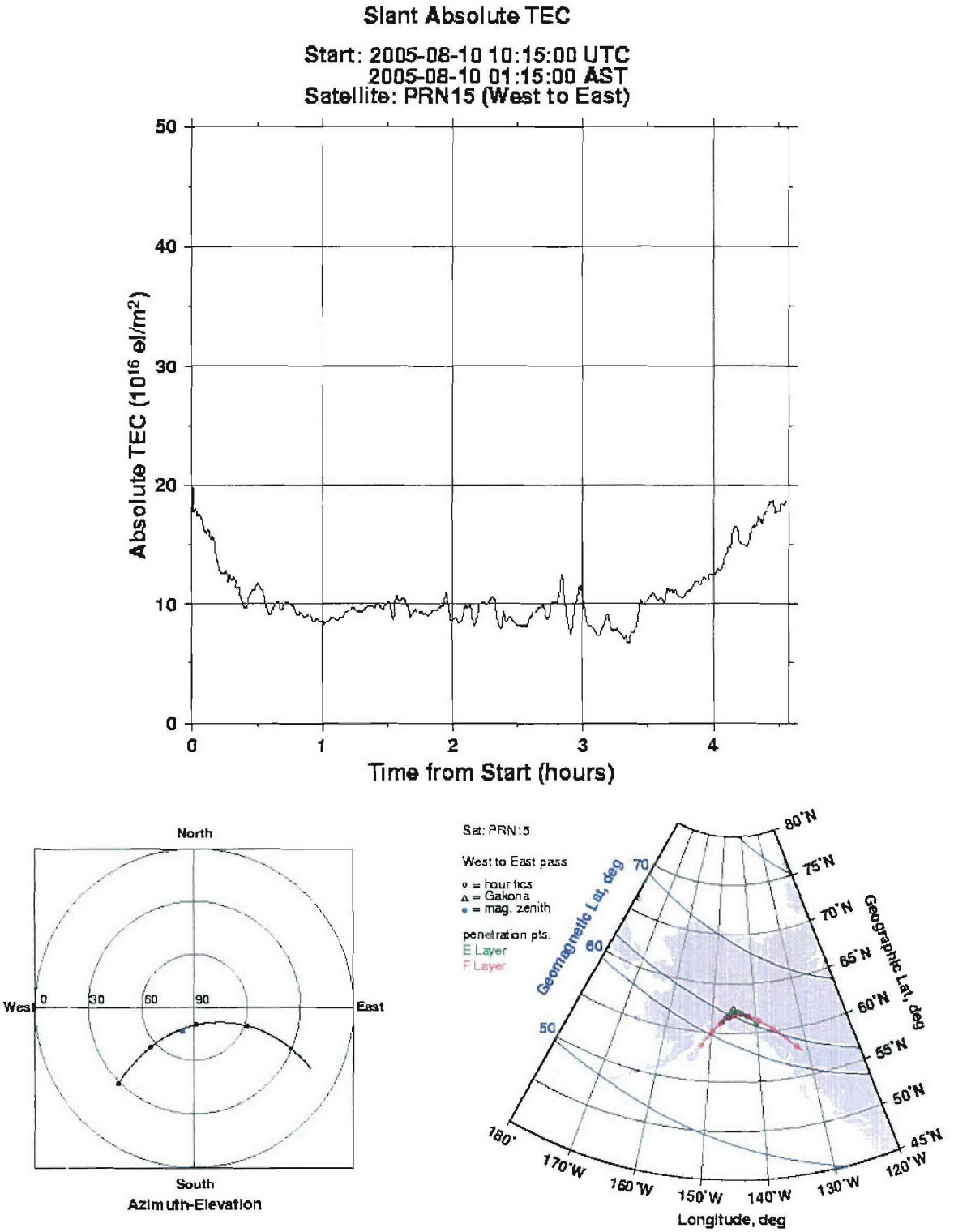


Figure A3. Example of GPS satellite data collected from the Ashtech Z-FX receiver located at Gakona. The upper panel shows the absolute slant TEC for the pass, the lower-left panel shows the elevation and azimuth angle geometry of the pass, and the lower-right panel shows the pass geometry on a map of Alaska.

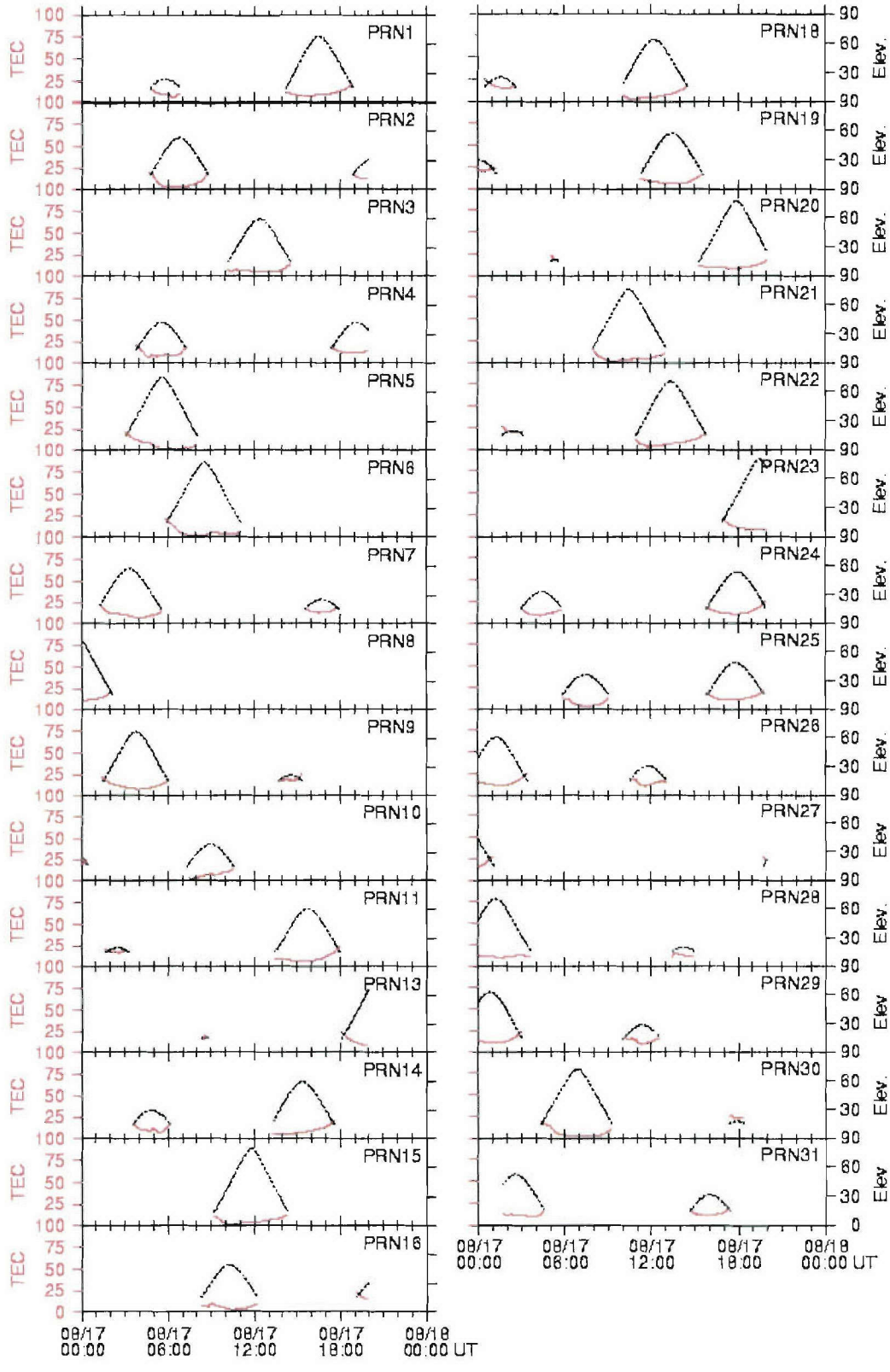


Figure A4. Daily individual GPS summary plot as shown on the HAARP Web site. The vertical absolute TEC (red lines) and elevation angle (black lines) are plotted as a function of UT for each GPS satellite as identified by PRN.

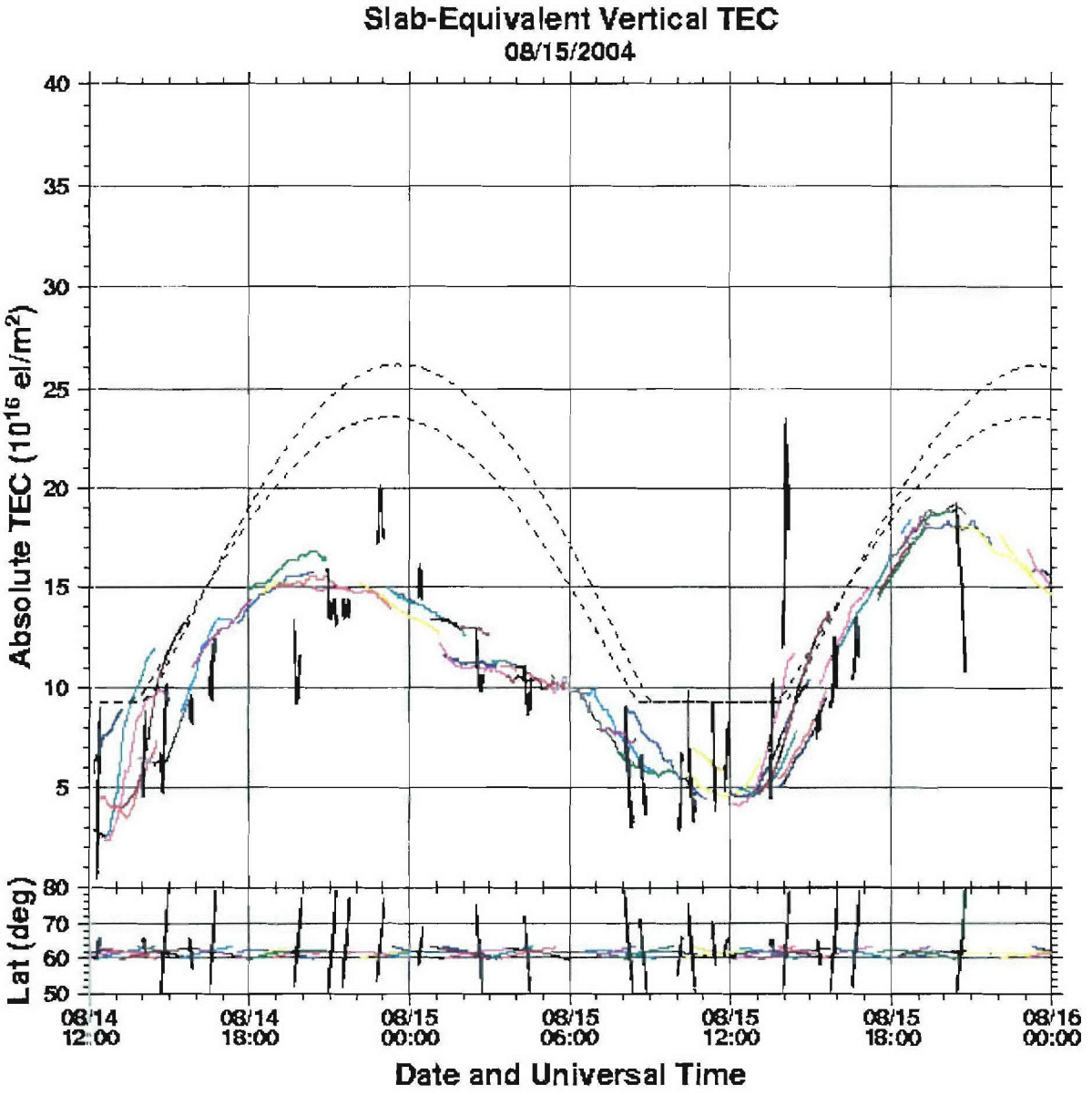


Figure A5. Summary of GPS-derived VTEC (colored curves) and LEO-derived VTEC (black curves) for a 36-hour period. The upper panel shows the variation of VTEC and the lower panel shows the 350 km IPP for the observation. The dashed curves in the upper panel are VTEC derived from the GPS TEC model (*Klobuchar*, 1987) using the IONO coefficients in the GPS telemetry stream for that day. The upper curve is for a GPS path looking to the south from Gakona and the lower curve is for a path looking to the north.

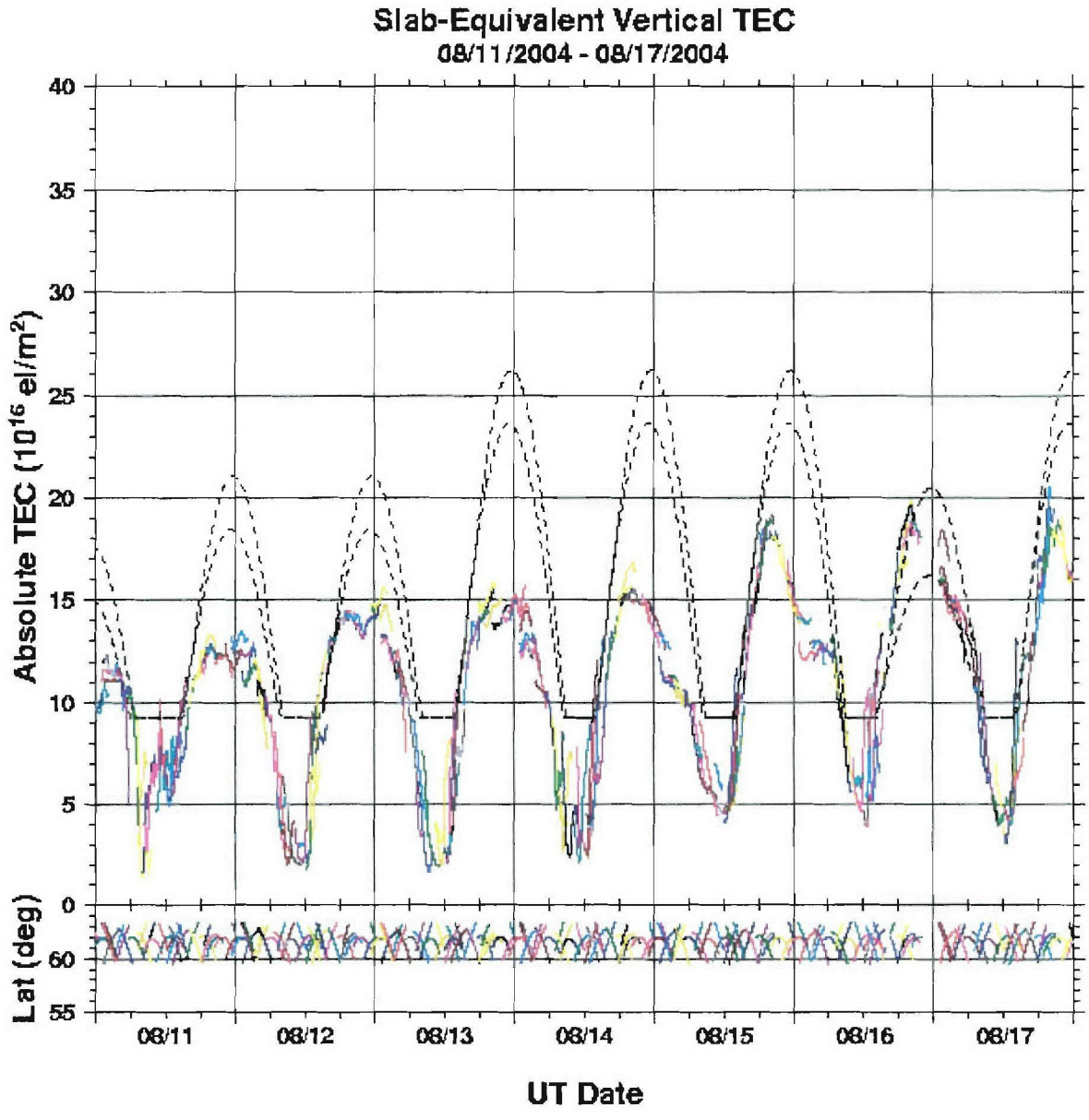


Figure A6. Same data (GPS only) as shown in Figure A5 but for a seven-day period.

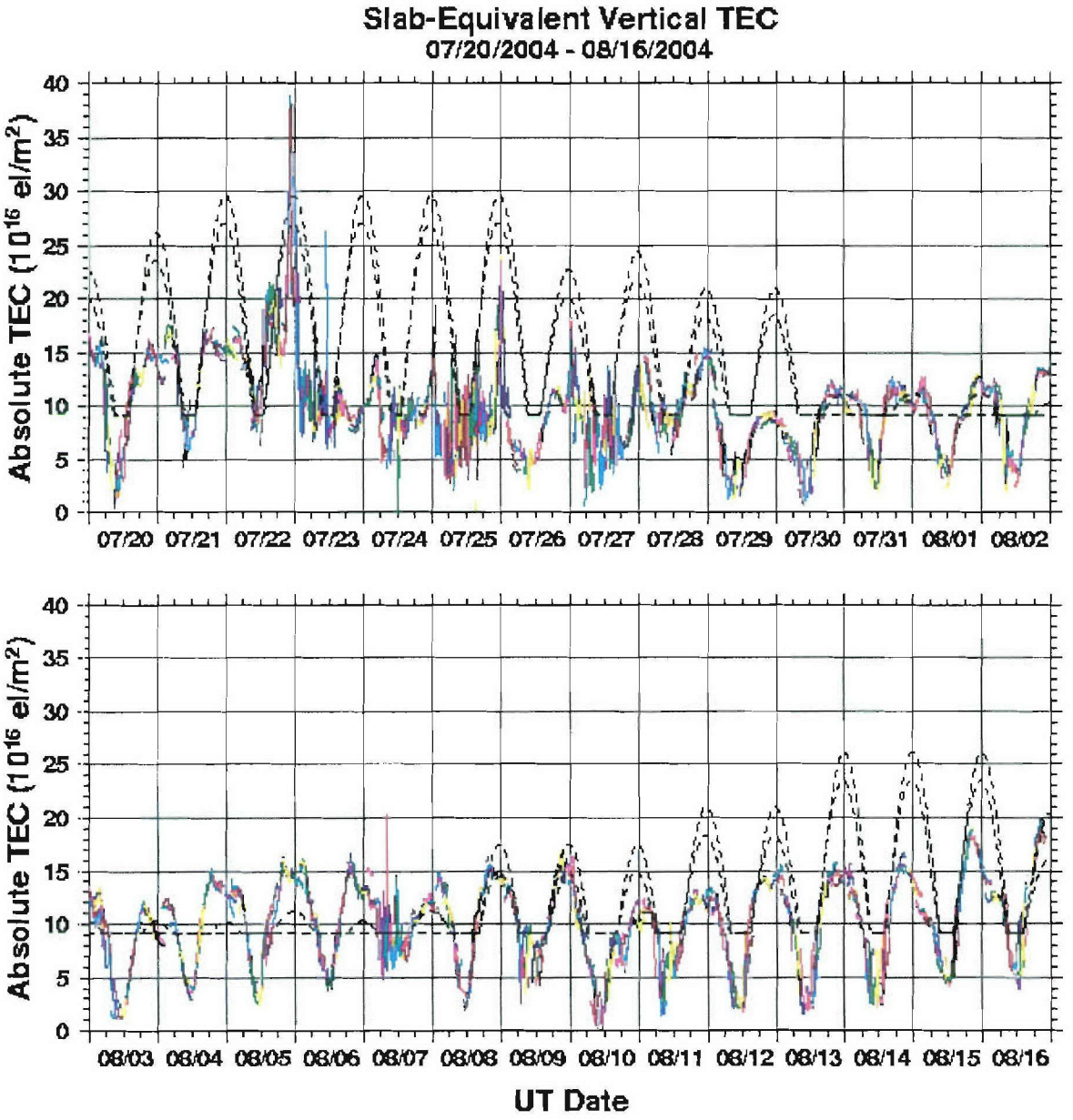


Figure A7. Same data (GPS only) as shown in Figure A5 but for a twenty-eight-day period.

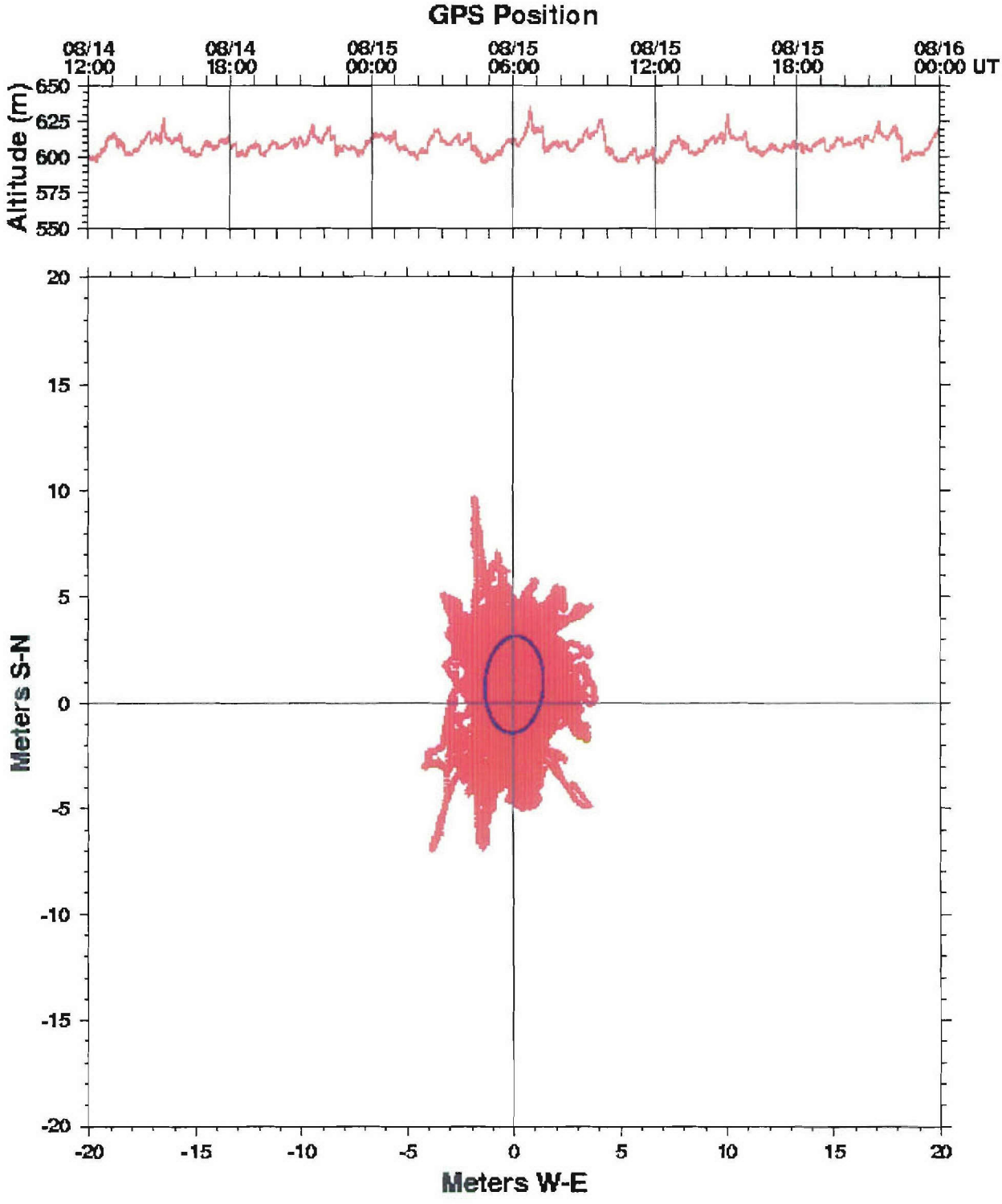


Figure A8. GPS position-error plot for a 36-hour period. The upper panel shows the altitude provided by the GPS clock for the 36-hour period, and the lower panel shows the GPS horizontal position relative to the true horizontal position. The inset blue ellipse in the lower panel is a least-squares fit to the horizontal error data showing the rms error by the size of the semi-major and semi-minor axes.

Appendix B. Consultant Activities Summaries

This appendix includes summaries of activities undertaken for the HAARP project by NWRA consultants as provided by each consultant.

B.1 Report from Mr. John Rasmussen

During this contract period NWRA coordinated significant additions and enhancements to the HAARP suite of diagnostic instruments and the supporting infrastructure.

B.1.1 Instrumentation Coordination:

NWRA has been involved in coordinating the installation of essentially all of the diagnostic instruments located at the HAARP facility as well as remote sites and in providing the infrastructure required for their successful operation. Examples include:

Imaging Riometer: Coordinated the planning for a diagnostic 8x8 Imaging Riometer with the University of Alaska. This instrument will complement the classic 30 MHz riometer currently located at HAARP. The Imaging Riometer will provide information on the spatial distribution of absorption in the lower ionosphere to aid in both the operation of the heating transmitter and in the interpretation of experimental data.

30 MHz Riometer: Provided test and installation support for the new riometer developed by Jens Ostergaard.

Optical Instruments: NWRA supported the acquisition of a new CCD camera for the HAARP Optical Imager. In addition NWRA provided coordination with Cornell University and SRI International (SRII) to develop the specifications for a new narrow field-of-view telescope and associated computer controlled mount and initiated procurements for these instruments.

B.1.2 Infrastructure Coordination

NWRA has been instrumental in assuring that the HAARP diagnostic instruments and the associated research scientists have the facilities available to work efficiently. This support has ranged from major acquisitions such as instrumentation shelters to making sure that general purpose computer terminals are available in the shelters to provide network access without interrupting dedicated diagnostic computers.

ELF/VLF Receiver Site: NWRA coordinated the move of the HAARP ELF/VLF diagnostic receiver from the HAARP site to Chistochina and arranged for space and power. This was a cooperative effort with the University of Alaska Fairbanks. The receiver operation has shown Chistochina to be a viable alternative to the current ELF/VLF receiving site at Gakona Junction, however, installation of a new power line past the Chistochina site has forced a delay in a final decision to move. The Gakona Junction site needs to be either upgraded or moved. The upgrade would require a new shelter and improved data communications.

28 MHz and 50 MHz Radars: A new instrumentation shelter was procured for Diagnostic Pad 2 resulting in a dedicated shelter for the 28 and 50 MHz radars.

Optics Infrastructure Upgrade: NWRA procured and installed a new 14 ft observatory dome and the associated arctic shelter to house the narrow field-of-view telescope/imager for studies of the optical emissions from the heated region. The dome was built by Ash Manufacturing Company of Plainville, IL and the arctic shelter was produced from Alchem, Inc. of Anchorage, AK. The dome and shelter were installed at Gakona in early May (see Figure B1).



Figure B1. New dome shelter for the narrow field-of-view telescope on Pad 3 (left), and the new shelter layout on Pad 3.

With the narrow field-of-view imager moved out of the Optics Shelter and into the new Dome Shelter, the five foot acrylic dome was moved back to its original position on the Optics Shelter. NWRA procured a heavy duty scissors lift and it was installed under the acrylic dome to support the Az/El mount and the HAARP Imager. In addition, the entire Optics Shelter was moved on Pad 3 to a position less subject to interference from automobile headlights.

B.1.3 Research Campaign Support

NWRA provided coordination as well as logistical and material support for general research campaigns along with ELF/VLF and optical campaigns.

B.1.4 Special Activities

NWRA participated in many special HAARP activities including the RF Ionospheric Interactions Workshop, Educational Outreach and Distinguished Visitor Tours. In addition, NWRA represented the HAARP diagnostics in program planning meetings, presenting the status of the instruments and advocating for the resources necessary to operate reliably and produce the best possible product.

Strategic Planning Meeting: Coordinated arrangements for the HAARP annual Strategic Planning Meeting that was held in Tenants Harbor, Maine from 30 August through 3 September 2004. The meeting included Air Force, Navy DARPA and BAE representatives.

ELF/VLF Receiver Workshop: Assisted Ed Kennedy in organizing the HAARP ELF Measurements Workshop, held in Washington, DC on 4, 5 November, and moderated a session on instrumentation. The workshop included both theory and instrumentation talks

and was followed by a discussion of specifications for a new HAARP ELF/VLF diagnostic receiver.

HAARP-Supported Scientists' Workshop: Provided coordination for the HAARP-Supported Scientists' Workshop that was held at the UCLA Conference Center, Lake Arrowhead, CA from 7-10 March 2005. NWRA was responsible for agenda development as well as providing planning, logistics, lodging, and conference facilities for approximately 40 scientists associated with the HAARP program. The Workshop provided a forum to review and highlight ongoing research sponsored by the HAARP and to foster technical interchanges between its scientists who represent a broad range of diverse disciplines related to ionosphere/radio science research.

Summer Intern: Coordinated arrangements to hire Mr. Troy Lawlor as the 2005 HAARP Summer Intern. Mr. Lawlor is in his second year at the University of Alaska Fairbanks majoring in computer science. This will be his third year with HAARP. Arranged for Mr. Lawlor to visit AFRL at Hanscom AFB to prepare for his work supporting Dr. Todd Pedersen's optical imager development.

B.2 Report from Dr. Arnold Snyder

B.2.1 Incoherent Scatter Radar (ISR)

The 18 month period culminated with the checkout, initial tests, and demonstrations at the Gakona, AK HAARP site of a 16-panel prototype of the Advanced Modular Incoherent Scatter Radar (AMISR) developed by SRII. This accomplishment was enabled by the NWRA consultants' work supportive of infrastructure development that included a dedicated shelter, electric power, telephone, and computer networking; foundation design and installation; acquisition and installation of the 16-panel support structure; and coordination of the 16-panel prototype AMISR installation. This activity involved coordinating and planning the work of the following principal organizations: National Science Foundation (sponsor of the AMISR development); SRII (developer of the AMISR prototype and installer of the 16 panels at HAARP); BAE Systems (HAARP operation and maintenance contractor); and the University of Alaska Fairbanks (recipient of an Office of Naval Research [ONR] grant to acquire an AMISR prototype for long-term test and evaluation in conjunction with the HAARP Ionospheric Research Instrument [IRI]). Figure B2 shows the completed installation of the 16-panel AMISR prototype at the Gakona, AK HAARP site.

B.2.2 Digisonde Upgrade

The University of Massachusetts at Lowell (UML) Digisonde originally installed at HAARP was an early prototype of a later instrument employed worldwide at some 50 ionospheric monitoring sites. When the original HAARP Digisonde failed, it often took the expertise of the Lowell developer and a hunt for scarce replacement parts. Given the Digisonde is vital for the successful operation of the Ionospheric Research Instrument, it was recommended the original instrument be upgraded to be compatible with the latest Digisonde version. This upgrade was coordinated with and accomplished by UML. Initial tests of the new Digisonde revealed instrument-generated, broadband interference below approximately 150 km range. The cause was found in four of the newly developed receiver cards; new cards were prepared and installed

by UML. This eliminated the interference. The new Digisonde has improved sensitivity, reliability, and is supported by the availability of spare parts should the instrument fail.



Figure B2. HAARP installation of the 16-panel AMISR prototype antenna.

B.2.3 Ionogram Scaling

Dr. Edward J. Fremouw (NWRA) selected a number of ionospheric tomography examples for comparison with F-region critical frequencies and associated true heights determined from the Gakona and College, AK Digisondes. Using the UML developed SAO Explorer software, the associated digital ionograms were downloaded from the UML digital data base, rescaled, and associated true heights determined as necessary.

B.2.4 Over-the-Horizon Backscatter (OTH-B) Radar Surplus Transmitter Equipment

I alerted a number of Department of Defense organizations that the Air Force was planning to dismantle the East and West Coast OTH-B Radar Systems and dispose of the associated seventy two 100 kW high frequency (5-28 MHz) transmitters as scrap metal. The Office of the Secretary of Defense became involved and the 72 transmitters were saved for potential future use. Groundscreen from the west coast transmit site will be used at HAARP for the new imaging riometer.

B.2.5 Imaging Riometer Installation Planning

An ONR grant to the University of Alaska Fairbanks provided for the acquisition of a 64-element, 38 MHz imaging riometer and subsequent research associated with the IRI. The imaging riometer will occupy an approximate 150 foot square on HAARP's Diagnostic Instrument Pad #3. During the latter part of this 18-month period, NWRA consultants were involved with the infrastructure planning and preparation. This included defining a preliminary Pad #3 layout and orientation for the imaging riometer antenna array; transportation of 90 concrete guying blocks from Anchorage to the Gakona, AK HAARP site; coordination with BAE Systems to level Pad #3 and install a fence around the pad to protect the imaging riometer antenna array; and coordination with Office of the Secretary of Defense personnel to acquire

surplus Over-the-Horizon Backscatter radar groundscreen to be used for the imaging riometer. Plans are to install the imaging riometer in late summer or early fall 2005.

B.2.6 Equipment Frequency Allocation

With Edwin Lyon, III (Science and Technology Associates, Inc providing SETA support to DARPA's HAARP-related program), I prepared and submitted DD Form 1494s for four HAARP radio frequency transmitting systems. These included the 3600 kW IRI; the Traffic Collision and Avoidance System (part of HAARP's aircraft alerting system); and the 28 and 50 MHZ ionospheric diagnostic radars. The NTIA has approved the IRI request for frequency allocation. The TCAS unit was fully certified for operation. The requests for frequency allocations are under consideration for the 28 and 50 MHz ionospheric diagnostic radars. Achievement of the aforementioned status for these four systems required development of answers to questions from the NTIA for the IRI, DoD International AIMS Program Office testing of the HAARP TCAS unit, and measurement of the spectral and harmonic frequency bandwidth measurements for the ionospheric diagnostic radars. The latter measurements were arranged by NWRA and conducted by John Brosnahan of Signal Hill Research, Inc. Data were developed for a subsequent Notice to Holders for the UHF 8-panel AMISR prototype; this included expansion to 16 panels and potentially to 24 panels. The Notice to Holders is under consideration. Initial tests of the 16-panel AMISR prototype were conducted under a 90-day temporary license granted by the Alaskan Frequency Management Office.

B.2.7 HAARP Optical Campaign Support

During the March 2004 HAARP Optical Science Campaign, coordinated the efforts of Drs. Frank T. Djuth (Geospace Research, Inc.) and Bodo W. Reinisch (UML) to use the HAARP Digisonde to acquire skymap measurements of HAARP IRI generated ionospheric irregularities. Participated in the initial analysis of the resulting skymap data. A multi-author journal paper is in preparation. For both the 2004 and 2005 HAARP Optical Campaigns, developed and implemented Digisonde special operating modes to support the optical experiments.

B.2.8 Distinguished Visitors

Supported the preparations for and participated in the Alaskan and HAARP visits by General Gregory S. Martin, Commander of AF Materiel Command May 20, 2004); Lieutenant General Carrol H. Chandler, Commander Alaskan Command (May 20, 2004); Dr. Anthony J. Tether, Director DARPA (June 25, 2004); Mr. James Engle, Assistant Secretary of the Air Force for Science Technology and Engineering (May 11, 2005); Mr. Ryan Henry, Principle Deputy Under Secretary of Defense for Policy (June 21, 2005); and Major General Perry Lamy, Commander Air Force Research Laboratory (July 21, 2005).

B.2.9 Summer Intern

With John Rasmussen coordinated transportation and lodging for Troy Lawlor summer 2004 and 2005 visits to the Air Force Research Laboratory, Hanscom AFB, MA. These visits were for the purpose of discussing his software development work with Dr. Todd Pedersen. Also coordinated Troy Lawlor's attendance at the HAARP/NSF sponsored 2005 Summer School; this involved arranging for Professor Brenton J. Watkins to serve as mentor and to develop a Summer School project for Troy Lawlor.

B.2.10 Program Reviews and Planning Meetings

Participated in contractor program reviews for BAE Systems, Stanford University, the Polar Aeronomy and Radio Science grant to the University of Alaska Fairbanks, planning meeting for the 2005 HAARP Optical Campaign and the September 1-3, 2004 Strategic Planning Meeting.

B.2.11 Workshop Planning and Support

Assisted in the preparation for and participated in the 2004 and 2005 Santa Fe RF Ionospheric Interactions Workshops and participated in the March 7-10, 2005 HAARP Sponsored Scientist Workshop.

B.2.12 Operations Center Infrastructure Improvements

Acquired and coordinated the installation of a motorized projection screen and a sound system for the HAARP Operations Center Conference Room. Acquired a large table and associated chairs for the data analysis center where HAARP experiments are planned and results analyzed.

B.2.13 Support for Site Cleanup

Surplus and or obsolete computer monitors and the Pathfinder Radar control console were transported from the HAARP Site and turned in to the Anchorage DRMO. In addition, commercial transportation was arranged from the HAARP Site to the Anchorage for an inoperative forklift and three pieces of a large water tank. The forklift was turned into the Anchorage DRMO and the water tank pieces to an Anchorage recycling center.

B.3 Report from Dr. Allan Schell

Note that references for the four memos cited by Dr. Schell in this report are listed at the end of this section.

B.3.1 Background

Construction of the AMISR has proceeded with some delays over this period. A Technical Advisory Committee (TAC) was formed at the request of the National Science Foundation to review and comment on the technical progress of this project. Results for the AMISR are important to HAARP because the same (or similar) modules are employed in the array at Gakona and also in the array at Jicamarca. The January 2004 meeting of the TAC was planned to review the completion of the initial 40 AEUs (Antenna Element Units) in order to consider a recommendation to proceed with building 512 more AEUs.

Problems occurred in several areas during production. Receive and transmit path losses were somewhat higher than expected. A mechanical redesign of the crossed dipole antenna was necessary. An unacceptable failure rate of transformers on the power supply board emerged. Also, a new supplier of power amplifier units was selected.

An issue that had arisen earlier was whether every AEU should have the capability to monitor the amplitude and phase of the radiated signal at the antenna ports. This capability entailed adding about $20 of additional circuitry to each AEU. SRII argued that this was an unnecessary enhancement and that adding this capability to one or two AEUs per panel (of 32

AEUs) was sufficient. Tests by AFRL had shown that snow on the antenna face could have a significant effect on performance, and the full array test capability would give a more accurate assessment of this performance. The AEUs for AMISR will have one enhanced AEU per panel, but the Gakona array will consist of all enhanced AEUs.

The TAC at the January 2004 meeting endorsed the construction of 512 AEUs under the following conditions:

a. Component problems such as the transformers on the power supply board must be satisfactorily resolved.
b. The DVT environment tests must be completed successfully.
c. A better test of receive and transmit losses should be devised and used.
d. The redesigned crossed dipole antenna must be validated.

The TAC observed that the delays had prevented observation of operation of the Gakona and Jicamarca arrays before further decision making, and they asked that the initial near-production panel be run continuously for 30 days to evaluate its operation. Other issues that warranted comment by the TAC were:

a. The solid state power amplifier requirement and compliance to it should be rigorously examined.
b. Further investigation of lightning strike protection should be done.
c. A better analysis of the Figure of Merit for this type of radar should be conducted.

The ability of the radar operator to assess the technical performance of the radar became an issue that I considered vital to successful use of the system. Phased array radars require detailed performance monitoring, fault isolation, and calibration. While some attention had been paid to this issue, it appeared that there were several shortcomings, and these were pointed out in two memos [1], [2] that I provided to AFRL. Not much additional work on this topic had been done at the time of the above mentioned TAC meeting.

B.3.2 The AMISR Technical Advisory Committee Meeting of July 21, 2004

At this meeting of the TAC, held at SRII, considerable progress was noted, although several items of the earlier schedule showed delays. Extensive tests were run on the circuit boards, on the AEUs, and a completed panel. Overall, the results were favorable. The design verification tests showed that the AEU design meets specifications. Environmental test results were generally satisfactory, but further testing of the new Solid State Power Amplifier (SSPA) design was needed. The following items were noted:

a. The long duration field site test showed that a panel would remain functional over several months, but also uncovered a solar heating problem and showed several AEU failures.
b. AEU manufacturing yields were currently around 73% (120 out of 164 manufactured by 19 July), with most failures resulting from the transmit power supply and excessive receiver noise.
c. Panel acceptance testing hardware was under construction; these tests were to be moved to Sanmina-SCI.

d. A change of SSPA vendors and the new design results in two different and potentially incompatible configurations. The new SSPA needs to be reconciled with its AEU power supply.
e. A start has been made on the AMISR calibration procedure. A test antenna atop a pole is positioned near the panel at the field site, and the software has been written. The geometry for the full array was not presented.
f. The receiver noise measurements were unchanged.
g. Foaming the column of the antenna element was not considered necessary, based on the results of the precipitation test. A procedure for foaming the elements has been developed, if subsequently needed.
h. Lightning protection of the receiver has been enhanced by shunt diodes on the input path. External protection was suggested by using lightning rods atop the calibration antenna poles.
i. SRII has concluded that the vector measurement of the currents at each antenna element is not of sufficient value to warrant inclusion, and instead will "enhance" two AEUs per panel with I and Q sensors rather than make all AEUs the same. This sparse (1 in 16) sampling of the aperture will not yield either accurate gain assessment or knowledge of the pattern at wide angles.
j. The TAC endorsed the building of 512 more AEUs, but did not recommend proceeding with the construction of the full array. They also asked that more emphasis be placed on system aspects of the radar, and that a revised system specification sheet be provided. Also noted were other design issues such as switching noise in the new SSPA.

An extensive description of these issues is in a memo [3] provided to AFRL.

B.3.3 The AMISR Technical Advisory Committee Meeting of June 30, 2005

The meeting of the AMISR Technical Advisory Committee on 30 June 2005 in Santa Fe was significant because the program is in the midst of a redesign effort to correct some potentially serious problems, some of which could impact the Gakona array.

An interference problem had occurred at HAARP. Apparently this was a configuration management problem by SRII that caused clock spurs on six AEUs. This has been fixed, but in the process they found another clock signal coming from the control board. This is a general problem; the SRII solution is to add a shielding screen on the PC 104 board. They are in the process of determining a suitable manufacturing fix with Sanmina SCI for the shielding.

The power transformer failure problem occurred because the counter on the core winder introduced random nicks to the wide insulation, and occasionally this caused a failure. This has been resolved.

The issue that occupied the bulk of the time and concern of the committee was the final amplifier chip of the solid state power amplifier (SSPA) now supplied by Comtech PST Corp. It was found that rapid fall times of input pulses caused the amplifier chips to fail. SRII began the correction process by adding a bandpass filter to each panel to increase the fall time. As the filter is at the panel level, not at each AEU, one is needed per 32 AEUs. Also, SRII found that their automatic test equipment was causing voltage spikes due to lack of proper synchronization.

Later, Comtech found that the chip could oscillate if overdriven. The chip supplier, Cree, has closed their Sunnyvale plant, where the laterally diffused metal oxide semiconductor (LDMOS) chips used for rf amplifiers were made. Consequently, SRII is looking again for an amplifier chip supplier.

The status of the current production run of Comtech SSPAs is somewhat uncertain. Some of these units were shipped to Gakona, although the first eight panels will use the amplifier by Delta Sigma, the first SSPA supplier. SRII will modify the Gakona and Jicamarca panels with bandpass filters, as the Cree amplifiers might be used as replacements at these sites. For AMISR, a redesign of the SSPA is an option.

After further discussion the following were the decisions of the TAC:

a. Build 32 AMISR panels, and then stop. (This is ¼ of a full face.) Test and determine how well these units work (for probably two months).
b. Initiate an alternative design of an amplifier as an option, and work with Sanmina SC to determine that the design is compatible to the maximum extent possible with existing equipment.
c. Install the 32 panels on one face and appraise the results of this and the design effort at the next TAC meeting in early October.

B.3.4 Progress on Performance Monitoring, Fault Isolation, and Calibration (PMFIC)

Dr. Todd Valentic reviewed the calibration, fault isolation and testing, and performance monitoring for the Gakona array and the AMISR. He has developed (although it is incomplete) a Web based monitoring system based on earlier work for Sondrestrom and other sites. His displays for Gakona form the basis for a more sophisticated system for AMISR. He has developed graphic presentations that give an overall display of the array status, including some quantitative ranges. If he completes his development successfully, the radar experimenter should have a considerable amount of information to quantitatively determine system performance. Also, because this is Web based, a maintenance crew could have access to detailed performance of array components. He understands that the experiment operator might want to be able to portray the actual radiation pattern, showing the effects of failed AEUs, in a convenient graphic format. He was able to call up on his laptop many of the initial fault isolation and performance readiness screens. The results were very encouraging progress towards the goal of an effective PMFIC system. Further details on this meeting and related matters are given in reference [4].

B.3.5 Memos Cited

[1] "Built-in Performance Monitoring, Fault Isolation and Calibration for a Phased Array Radar," Allan C. Schell, February 7, 2003.

[2] "Further Report on Built-in Performance Monitoring, Fault Isolation and Calibration," Allan C. Schell, March 3, 2003.

[3] "Report on the AMISR Technical Advisory Committee Meeting of July 21, 2004," Allan C. Schell, July 28 2004.

[4] "Report of the AMISR Technical Advisory Committee Meeting of June 30, 2005," Allan C. Schell, July 5, 2005.

B.4 Report from Mr. Jens Ostergaard

B.4.1 Riometer Operations

The first 18 months of the contract period were spent finalizing the development of a new standard riometer for HAARP, continued development of a method to compute quiet day curves, updates of the antenna system, and on the data acquisition computer hardware and software.

The riometer used for the first many years of measurements at HAARP did show instabilities and non-linear calibration characteristics. Over the past few years, HAARP has funded the development of a new standard 30 MHz riometer. The major design objectives were to improve the rejection of large out of band signals close to the riometer frequency, to obtain real time absorption measurement and inherently linear operation using digital noise balancing techniques and to develop an embedded instrument controller. The sky temperature can, on very rare occasions during deep absorption events, reach values less than 290° K, the normal lower limit for a 30 MHz riometer. By injecting a small amount of offset noise in the signal path, a noise-balancing riometer can measure antenna temperatures less than 290° K provided the integration time is long enough to obtain the necessary radiometric resolution. This feature has been incorporated in the new design.

The salient features of the new riometer are:

- Noise-balancing radiometer principle.
- Extended measurement range to ~ 10° K to 200,000° K.
- Interference protected receiver front end.
- Frequency agility. Will search for the most quiet frequency in the 29 - 32 MHz range if signal exceeds the quiet day noise level.
- 30 kHz IF bandwidth, with 90 dB out of band attenuation.
- Inherently linear, digital noise balancing using high quality, Solid State Noise Sources.
- Computed quiet day curve computation for all locations and two representative riometer antennas (single, five element crossed Yagi, and array of four, five element crossed Yagis.).
- Embedded real time clock. Can be set from an attached GPS receiver or the associated data collection system.
- Simple ASCII, RS-232 data interface modeled after the NMEA0183 Marine Data Exchange Format.

The design objectives were met at the start of the current contract, but a number of hardware development problems have plagued the stability of the new riometer receiver during the reporting period. Some have been traced to interference from the original, switch-mode power supply in the riometer receiver, and some to the antenna system.

The switch-mode power supply has been replaced with a battery of linear regulators. This has eliminated internal interference in the riometer receiver. It was found that the data transmission between the riometer and the data collection computer every second created interference in the induction magnetometer system. This interference was not expected as all the transmission lines are twisted, shielded pair cables. The interference was traced to the DC power

supply lines between the instrumentation shelter and the riometer receiver, and was eliminated by moving the AC power supply from the shelter to the receiver box by the antennas.

In recent years, a number of abrupt changes in the quiet day curve have been observed to occur at the onset of very low temperatures in the early winter. The change, a markedly lower quiet day antenna temperature indicative of a change in the antenna beam, did persist into the spring and summer. Intensive tests of the antennas, their phasing and feed systems have not revealed a plausible cause for this jump, but one previous quiet day discrepancy was traced to a faulty balun in the antenna system. The discrepancy disappeared when the balun was replaced. During the recent site visit, all eight baluns were replaced with sturdier versions constructed from heavy, coaxial cable. This has stabilized the quiet day curve at a slightly lower level than anticipated. The difference is most likely caused by the new baluns center frequency being slightly lower than 30 MHz. This effect is currently being examined with NEC antenna modeling. The computed quiet day curve has been adjusted accordingly.

Traditionally, quiet day curves for riometers have been derived from a number of seemingly quiet days selected from the recorded data. This method is not applicable at auroral locations, as none, or very few quiet days are found. Also, using quiet day recordings will introduce a masking effect of the regular lower ionosphere absorption, that varies with time of day and season. This absorption is real and should not be excluded. The noise temperature of an antenna at VHF can be computed if the location of the antenna, the antenna radiation pattern, and the noise temperature distribution of the sky are known. The location is a given, and the antenna radiation pattern can be computed using NEC or other similar software.

A Galactic Noise Map suitable for computation of antenna temperatures in the 30 MHz - 400 MHz range were presented by *Taylor* [1973]. Maps presenting Galactic Noise temperatures in degrees K for the whole sky at 136 MHz and 400 MHz are included. The temperatures can be scaled to any frequency in the VHF range. The spatial resolution of the maps is good enough to yield accurate results with the relatively broad beam antennas used for riometers. The 136 MHz noise map has been digitized and software produced to compute antenna temperatures for moderate gain Yagi arrays at frequencies of 30, 35, 45, 65, 85, 104, and 150 MHz with good results. The noise map and the software can be embedded in a modern riometer, facilitating instant absorption measurement at any location.

B.4.2 Participation in the HAARP Lake Arrowhead Workshop

It was very informative to participate in the Lake Arrowhead workshop in April 2005. The current status of the riometer was presented, and very good feed back was received from the users. It is reassuring to know that the data is being used, and that the quality matters. A wish for better time resolution than the current one minute was expressed by some users. The basic conversion cycle in the new riometer is one second, and this resolution can be made available within a matter of a few months. However, a time resolution of 0.1 second has been mentioned as a goal for some HAARP experiments. Such a resolution will require a redesign of the riometer timing and must be seen as a more involved process. It is the hope that the dialog with the users will continue, and that the riometer data can be adapted to the needs of the largest possible circle of users.

B.5 Report from Dr. Spencer Kuo

Dr. Kuo's report was provided as a preprint of a paper to be published in Geophysical Research Letters (*Kuo and Rubinraut*, 2005). The abstract from that report is provided here.

> The theory of electron acceleration by upper hybrid waves at second harmonic cyclotron resonance is presented. The results show that the meter-scale upper hybrid waves can incorporate the finite Larmour radius effect to make a second harmonic cyclotron resonance interaction effective. The finite Larmour radius effect provides a positive feedback to the interaction, thus the energies of the accelerated electrons increase in time exponentially, rather than linearly as in the case of fundamental cyclotron resonance. Consequently, energetic electrons (having energies larger than 10.7 eV) can be generated even at very low upper hybrid wave intensities. The threshold field for parametric excitation of meter-scale upper hybrid waves by O-mode HF heating wave is shown to be very low. The theory can be a reasonable basis for explaining the enhancement of airglow at 777.4 nm observed in recent low-heating-power experiment at HAARP.

B.6 Report from Dr. William Gordon

My participation in the HAARP effort during the referenced period included the following activities:

1. Evaluation of HAARP campaigns and planning for new campaigns at Santa Fe workshops and the Arecibo workshop.

2. Lectures to workshop schools on the early Arecibo days, and engineering as art. The first introducing incoherent scatter as a technique to study the upper atmosphere with a powerful radar, and the extension to planetary radar studies and to the large radio telescope as the best observer of pulsars and of other solar systems. The second "defining" engineering and suggesting characteristics of art, profusely illustrated, as an after dinner talk.

3. Discussions with Elizabeth Gerkin (lighting up the sky) and others on the conditions to generate airglow

4. Participated in discussions with "open house" visitors on the safety features of HAARP with respect to its neighbors.

Appendix C. Activities of the HAARP Summer Student Interns

NWRA employed Mr. Troy Lawlor as an HAARP summer student intern during the period covered by this report. This appendix contains summaries of Mr. Lawlor's activities during the entire first summer and the second summer through mid-August 2005. Documentation for the browser described by Mr. Lawlor (keoBrowser) was provided to Dr. Todd Pedersen of AFRL as a separate report.

C.1 Report for Period June 2004 through August 2004

During the summer of 2004, Dr. Todd Pedersen of the Hanscom AFRL assigned me the task of writing a Java Applet capable of analyzing and browsing All-Sky Imager data. The project can be viewed as a follow-up to my activities for Dr. Pedersen last summer, wherein I wrote a JavaScript version of the tool along with a CGI interface for the All-Sky Imager control software. Unfortunately JavaScript has many limitations, particularly with regard to file inspection and manipulation. This made browsing large sets of Imager data inconvenient and slow. Also, JavaScript could not display raw imager data, only JPEG previews of the data created with a separate program. So a more powerful and robust browser was needed, preferably one that could replace expensive IDL based browsing tools.

To begin work on the project, NWRA sent me to Hanscom AFB to meet with Dr. Pedersen. There, we discussed the implications and complications of creating the Java applet and I was able to start laying the groundwork for the applet. When I returned to HAARP, I was introduced to some of the new faces at the OpCenter and shown the state of construction on the array. I then began work on the applet.

Due to construction and the presence of another intern at HAARP this summer, there were only a few auxiliary projects for me to work on. Thus, I was able to devote the majority of my time to the Imager Browser. Creating the applet was more difficult than I had anticipated, and features that I thought I could write quickly turned out to be long pieces of code that broke with many Java applet guidelines.

Traditionally, Java applets are not capable of reading files on the client machine, much less search through directories and write large data files. Speed was also an issue, as Java applets are interpreted and use garbage collection. This particularly impacted the raw data reading and keogram creation routines. With some optimization, I was able to get the slower parts of the browser almost up to speed with their C counterparts.

Eventually the browser started to take shape and become useful. Thus, I was able to implement every feature Dr. Pederson had requested except for a geographic coordinate mode that was sacrificed so that I could more completely bug-test the browser as the summer drew to a close. Building the Imager browser was a fun project, a learning experience, and something that I hope will continue to be useful for years to come. I would like to thank everyone who made this summer internship possible, in particular Todd Pedersen, Jim Secan, John Rasmussen, and Lee Snyder.

C.2 Report for Period June 2005 through August 2005

My employment this summer began with a trip to Hanscom AFRL to meet with Dr. Todd Pedersen. This was my third summer working with Todd on an imager related project. Last year I wrote a Java applet for browsing and analyzing imager data called "KeoBrowser." Todd had a few new features that he wanted to see and had discovered some bugs that needed to be fixed. I was introduced to 1st Lt Richard "RJ" Barton, who has been working on a new general imager library that can be used with only a few modifications to run most types of imagers. Typically, imagers used for atmospheric research have many components in common, such as filter wheels and intensifiers. By using a common code base for creating JPEG images, organizing imager data into directories, and parsing parameters and commands, a lot of work can be saved when deploying a new imager. Todd and RJ wanted me to adapt the library for use with the HAARP all-sky imager, and had a list of improvements to the library they wanted.

Additionally, a moveable stage for the imager has been installed at HAARP. When using a narrow-field lens with the imager, the stage allows the camera to pan across the sky and view specific targets. Unfortunately, no automated control for the stage existed, so positioning the camera required the operator to be physically present in the optical shelter and ensure that the camera was moved at the correct time. Todd requested that I find a way to integrate the stage control with the general imager library so that the user could set up a schedule of the locations they would like to point the camera during the night and have the computer steer the stage.

Upon returning to the HAARP site, I started working on the imager projects. Unfortunately the HAARP imager exhibited strange behavior when it was removed from the crate it had been shipped in. It started working correctly after the filter wheel was exercised, which indicated that perhaps a cable or connection was loose. I was unable to determine the original problem, but was glad that it was functioning again. Unfortunately, when the imager was moved from the optical shelter to the new shelter with a telescope dome for 2nd Lt Robert Esposito's presentation, the original problems returned. Lt Esposito and I spent many days trying to determine the source of the malfunction, and the problem remains unsolved. The HAARP stage was comparatively a breeze to work with. It took just a few days to set up and integrate with the general imager library.

Mr. John Rasmussen has encouraged me to join the PARS Summer School as a student nearly every summer that I have been involved with HAARP. In previous years, I had helped out with the student experiments, but hadn't traveled to UAF or attended the lectures. This year, I actually joined as a student. Dr. Brenton Watkins with the GeoPhysical Institute offered me a software project I could work on rather than conduct an experiment. There was no way to view AMISR data from outside of the AMISR shelter, so I wrote a CGI program that allows the user to browse the data from anywhere using their browser. Dr. Michael McCarrick of BAE Systems was a great help with the networking issues.

I spent a lot of time this summer troubleshooting the imager to no avail, which was frustrating. However, I had a great deal of success with my other projects: improvements to the new general imager library, computer automated stage control, improved imager data browsing software, and a Web-based AMISR data display. It was, as always, a great learning experience. I'd like to thank NorthWest Research Associates and everybody at the HAARP site for letting me work on such interesting projects.

References

Andreasen, A.M., E.J. Fremouw, E.A. Holland, A.J. Mazzella, G.S. Rao, and J.A. Secan, Measurements of the Ionosphere and Protonosphere in the Wake of Solar Maximum, *R&D Status Report 8* on Contract F19628-01-C-0005, January 2003.

Andreasen, A. M., J. Begenesich, E. Fremouw, E. Holland, A. J. Mazzella, Jr., J. Ostergaard, J. Rasmussen, J. A. Secan, A. L. Snyder, Ionospheric Measurements in the Wake of Solar Maximum, Final Report, *AFRL-VS-HA-TS-2004-1125,* Air Force Research Laboratory, Hanscom AFB, MA, 2004.

Bishop, G.J., A.J. Mazzella, and E.A. Holland, Self-Calibration of Pseudorange Errors by GPS Two-Frequency Receivers, *Proceedings of 1995 National Technical Meeting,* The Institute of Navigation, Washington, D.C., January 1995.

Fremouw, E.J., J.M. Lansinger, and J.A. Secan, "A Feasible Ionospheric Tomography System," *GL-TR-90-0353*, Geophysics Laboratory, Air Force Systems Command, Hanscom AFB, MA, 1990.

Fremouw, E.J., J. A. Secan, R.M. Bussey, and B. M. Howe, "A Status Report on Applying Discrete Inverse Theory to Ionospheric Tomography," *Int. J. Imaging Syst. & Tech.* **5** (2), 97-105, Sept,-Summer 1994.

Fremouw, E.J., J. A. Secan, and B. M. Howe, "Application of Stochastic Inverse Theory to Ionospheric Tomography," *Rad. Sci.* **27** (5), 721-732, Sept,-Oct. 1992.

Fremouw, E.J., J.A. Secan, and Chucai Zhou, Tailoring of EOFs for Ionospheric Tomography and the Weighted, Partitioned, Least-squares Algorithm, *Acta Geodaetica et Geophysica Hungarica, 32*, pp. 365-377, 1997.

Fremouw, E.J., A.J. Mazzella, Jr., and G.-S. Rao, Investigations of the Nature and Behavior of Plasma-Density Disturbances That May Impact GPS and Other Transionospheric Systems, Scientific Report No. 3, *AFRL-VS-TR-2001-1538,* Air Force Research Laboratory, Hanscom AFB, MA, 2000.

Gurevich, A, E. Fremouw, J. Secan, and K. Zybin, "Large-scale Structuring of Plasma-density Perturbations in Ionospheric Modifications," *Phys. Lttrs. A., 301*, pp. 307- 314, 2002.

Kersley, L., J.A.T. Heaton, S.E. Pryse, and T.D. Raymond, Experimental Ionospheric Tomography with Ionosonde Input and EISCAT Verification, *Ann. Geophysicae 11*, pp. 1064-1074, 1993.

Klobuchar, J.A., Ionospheric time-delay algorithm for single-frequency GPS users, *IEEE Trans. Aerospace and Electronic Sys., AES-23,* 325-331, 1987.

Kuo, S. P., and M. Rubinraut, Generation of energetic electrons at second harmonic cyclotron resonance in ionospheric HF heating experiments, to appear in *Geophys. Res. Lett.,* 2005.

Mazzella, A.J., Jr., J. Begenisich, E.A. Holland, E.J. Fremouw, J.A. Secan, "Coordinated TEC Measurements for HAARP Using Transit and GPS," *Proceedings of the International Beacon Satellite Symposium,* 2001.

Miller, D. C., and J. Gibbs, Ionospheric Modeling and Propagation Analysis, *RADC-TR-78-163*, ADA062998, Rome Air Development Center, NY, 1978.

Reinisch, B.W. and X. Huang, Deducing topside profiles and total electron content from bottomside ionograms, *Adv. Space Res., 27,* 23-30, 2001.

Secan, J. A., *WBMOD Ionospheric Scintillation Model, An Abbreviated User's Guide (Version 15), NWRA-CR-94-R127/R6,* NorthWest Research Associates, Inc., Bellevue, WA, 30 September 2004.

Taylor, R. E., 136 MHz / 400 MHz radio sky maps, *Proc. IEEE, 71,* 469, April 1973

List of Symbols, Abbreviations, and Acronyms

AEU	Antenna Element Unit
AFRL	Air Force Research Laboratory
AMISR	Advanced Modular Incoherent Scatter Radar
APTI	Advanced Power Technology, Inc.
ELF	Extremely Low Frequency
EOFs	Empirical Orthonormal Functions
eV	Electron volt
f_0F2	Critical frequency (O-mode) of the F2 layer (MHz)
GIOS	NWRA GPS Ionospheric Observing System software
GPS	Global Positioning System
HAARP	High-frequency Active Auroral Research Program
HF	High Frequency
IMS	Ionospheric Measuring System
IPP	Ionospheric Penetration Point
IRI	Ionospheric Research Instrument
ITS	Ionospheric Tomography System
K	Kelvin (degrees)
kHz	Kilohertz (10^3 cycles/seconds)
kW	Kilowatt (10^3 watts)
L-band	Radio frequency band covering 1.0 GHz to 2.0 GHz (nominal)
MHz	Megahertz (10^6 cycles/seconds)
NetCDF	Network Common Data Format
NIMS	Navy Ionospheric Monitoring System
NNSS	Navy Navigational Satellite System
NRL	Naval Research Laboratory
NTIA	National Telecommunications and Information Administration
NWRA	NorthWest Research Associates
ONR	Office of Naval Research
PCA	Polar Cap Absorption
PDR	Powerful Diagnostic Radar
PMFIC	Performance Monitoring, Fault Isolation, and Calibration
PRN	Pseudo-Random Noise (GPS identification signature)
RINEX	Receiver Independent Exchange (data format)

rms, RMS	root mean square
S-band	Radio frequency band covering 2.0 GHz to 4.0 GHz (nominal)
SAO	Standard Archiving Output
SCORE	Self-Calibration of Range Errors
SEE	Stimulated Electromagnetic Emission
sps	samples per second
SRII	SRI International
SSPA	Solid state power amplifier
TAC	Technical Advisory Committee
TEC	Total Electron Content (el/m^2)
UHF	Ultra High Frequency radio band (300 MHz – 3 GHz)
UML	University of Massachusetts at Lowell
UPS	Uninterruptible Power Source
VHF	Very High Frequency radio band (30 MHz – 300 MHz)
VLF	Very Low Frequency radio band (3 kHz – 30 kHz)
VTEC	Vertical (or equivalent vertical) TEC (el/m^2)
WBMOD	WideBand MODel (NWRA ionospheric scintillation model)
WDLS	Weighted, Damped, Least-Squares
σ_ϕ	Ionospheric phase scintillation index (radians)